August 2018

Fabrication and Characterization of Superconducting Metamaterial Resonators

Haozhi Wang
Syracuse University

Abstract

Superconducting circuits operated at low temperatures have led to rapid advances in quantum information processing as well as quantum optics in the microwave regime. Engineered quantum systems with a dense spectrum of modes coupled to artificial atoms, or qubits, formed from superconducting circuits offer an opportunity to explore large-scale entanglement or perform quantum simulations of many-body phenomena. Recent research efforts into artificial metamaterials have yielded microwave and optical systems with numerous counter-intuitive properties, including left-handed transmission, where the group velocity and phase velocity for a wave point in opposite directions. Metamaterial resonators implemented with superconducting thin-film circuits provide a route to generating dense mode spectra in the microwave regime for coupling to qubits. In this thesis, we discuss the implementation of such superconducting metamaterial resonators. First, we derive the dispersion relation for one-dimensional metamaterial transmission lines and we describe the formation of resonators from such lines and their quality factors. Next, we describe the design and fabrication of transmission-line metamaterial resonators using superconducting thin films. We characterize the metamaterials through low-temperature microwave measurements as well as Laser Scanning Microscope (LSM) images of the microwave field distributions in the circuit. We compare these various measurements with numerical simulations of the microwave properties of the circuits, including simulated current density and charge density distributions for the excitation of different resonance modes. Following the successful realization of dense mode spectra in these circuits, we have initiated the first experiments with a superconducting transmon qubit coupled to a metamaterial resonator and we describe our progress in this direction.

Fabrication and Characterization of Superconducting Metamaterial Resonators

by

Haozhi Wang

B.S., Renmin University of China, 2011

DISSERTATION

Submitted in partial fulfillment of the requirements for the

degree of Doctor of Philosophy in Physics

Syracuse University

August 2018

Acknowledgements

I'd like to thank my advisor, Prof. Britton Plourde, for giving me the opportunity to join his group and work on this fascinating project of metamaterial resonators. I've learned a lot of theoretical and experimental knowledge of circuit QED, conventional resonator properties, left-handed transmission lines, ADR and DR operations, measurement setups and many many more by working with him in the past 7 years. I always have a feeling that he knows the answers to all of my questions about research. He was always very kind and patient to me, trusted me, supported me when I encountered frustrations, tolerated me when I made mistakes, and encouraged me when I felt depressed. I still remember that he once checked a sample which was going to be cooled down the next day with me under the microscope very carefully, even though it was already very late that day. We did find a very tiny scratch on the feedline, on a place where looked to be perfect under 10 $\times$ magnification, and saved me from spending a few days on a sample that wouldn't behave well under measurement. He showed my the importance of being patient and careful for being a qualified experimental researcher. My wife always says that I am very lucky to be Britton's student, and I indeed feel so. I really appreciate all the help and support he provided me in my entire Ph.D career.

I'd like to thank my parents, Liangji Wang and Xianyu Fang, who have been extremely supportive for my decision of pursuing doctoral degree in America and during my entire studying period. They always work hard to make sure I have fewer worries and they encourage me not to fear the challenges in my life and career. They contributed a lot to my success today and I am so proud to have them as my parents.

I'd like to thank my wife, Chengyan Jing, who always gives me love and support. The last few weeks before my defense was really tough for us, but she was very strong and brave. I will never forget the sacrifice and effort she made for our family and how she helped me overcome all the negative emotions. I'm so blessed to have Chengyan as my wife.

I'd like to thank all the people and friends who helped me on my project and thesis. Prof. Matthew LaHaye contributed a lot to the LHTL theory. He was the first one to point out that the reflection coefficient of the discrete transmission line with open-ended boundary condition is not 1, which is the really the fundamental difference of calculation the voltage and current distribution in the TL between discrete and continuous cases. Dr. Yu Hao was

like a big brother to me during his time in Syracuse. He took good care of me, taught me a lot of theoretical and experimental knowledge, and shared with me a lot of his experiences on how to successfully become a Ph.D. student. He also contributed a lot on deriving the analytic expression of the coupling quality factor of discrete transmission line. During my initial period of working in the Plourde Lab, Dr. Mike Defeo and Prof. Francisco Rouxinol guided me and worked with me through the entire fabrication process. Many of my recipes, skills and tricks were gained from them. Dr. Bruno Taketani worked closely with me on the theoretical part of the LHTL project and I have benefited a lot from discussing with him. Dr. Matt Hutchings also made remarkable contribution to the LHTL project, especially on fabricating the sample with qubit coupled to the LHTL modew and measuring the sample in dilution fridge. My colleague Indrajeet who also works on my project gave me a lot of help on the experimental part. I'd also like to thank Dr. Daniela Bogorin, Dr. Ibrahim Nsanzineza, Dr. Joel Strand, Dr. Matt Ware, Dr. Jiao He, Caleb Jordan, Dr. Jie Yang, Yebin Liu, Dr. Chunhua Song, Kenneth Dodge, Dr. JJ Nelson, Dr, Jaseung Ku, and all others who worked with me and helped me on my research, and my friends Yuxiang Wang, Jialu Xu, Junyao Li, Dr. Richard Galvez, Dongshu Liu and many others who helped me and made my time in Syracuse an unforgettable journey of life. I wish you all good fortune.

Contents

List of Figures

Chapter 1

Motivation and introduction

Quantum optics realizes the interaction of atoms with photons in a cavity using quantum electrodynamics (QED) [4], where the interaction between atoms and a cavity is made strong by confining the field into a small mode volume [5]. Instead of using real atoms, circuit QED, or cQED has taken a step further by using superconducting circuits as the artificial atoms, also known as qubits, to interact with a superconducting circuit microwave resonators [5–7]. In cQED, the microwave resonators are often made by distributed coplanar waveguide (CPW) cavities patterned from superconducting thin films [8], although they can also be formed by other resonant structures, including 3D waveguide cavities [9, 10]. The interaction is realized by the qubit(s) capacitive coupling to voltage antinodes or inductive coupling to current antinodes of standing waves in the microwave resonator [5]. This coupling is typically used for the readout of superconducting qubits in quantum information processing schemes [11], the generation of entanglement between multiple qubits [12], or a variety of explorations of quantum optics in the microwave regime [13]. The strong coupling regime, where the coupling strength becomes comparable to characteristics transition energy scales of the constituent systems, can be achieved in cQED [14–16]. Similarly to the cavity QED, cQED also permits the strong coupling between the qubit and the photonic modes in the cavity due to both the large transition dipole of the qubit and the small mode volume of

the cavity. The cQED approach also has a benefit of being flexibly engineered using entirely human made elements, which makes it possible for multi-modes coupling and for engineering of specific parameters like transition energies and coupling strengths. [17–21].

Recently, there have been several efforts addressing the generation of multi-mode spectra in cQED systems. By using long ($\sim 1\,\mathrm{m}$), transmission-line resonators, the high harmonics ($n \sim 75$) can be spaced closely enough to allow for simultaneous multi-mode coupling with a superconducting qubit [22]. Another approach involves the fabrication of arrays of coupled superconducting thin-film resonators for photonic quantum simulation [23, 24]. Superconducting thin-film cQED arrays with multiple resonances have also been investigated for a multi-mode quantum memory [25, 26]. In addition, microwave frequency combs have been generated by pumping the superconducting nonlinearity in a thin-film resonator [27].

An alternative route for implementation of novel, dense multi-mode spectra coupling is to use left-handed metamaterial transmission lines as the cavity. Left-handed materials having both a negative permeability and permittivity, which leads to a negative index of refraction and left-handed transmission properties, were first described in the last century [28]. More recently there have been numerous investigations of a variety of counterintuitive optical properties in these systems, including cloaking [29] and superlensing [30]. Research in this direction is closely connected to the field of photonic band-gap engineering [31]. Scientists have not discovered any natural material with left-handed optical properties, thus metamaterials are required in order to create left-handedness artificially. The metamaterial uses man-made structural elements, which in general are smaller than the wavelength of the radiation of interest and arranged in a dense lattice to perform as an effective optical medium. Here, we follow this approach with the extension that we explore the system up to the limit of Bragg reflection where the wavelength approaches the lattice constant.

An example of metamaterials that engineers make to exhibit left-handed properties is the arrays of wires and split-ring resonators (SRR) [32]. Such metamaterials can achieve negative permittivity and negative permeability in certain frequency ranges [33, 34], and can be made

to have very low losses by using superconductors as the material of making the SRRs [35, 36]. The superconducting quantum interference device, also known as SQUID, is another building block for superconducting metamaterials [37–39] that present left-handedness using quantum effects [40].

The left-handed metamaterial transmission line formed from lumped circuit elements is one of the realizations of the left-handed medium that have been proposed [41] and studied [42, 43] on the macroscopic scale for a variety of applications of microwave devices. The left-handed property for this system is equivalent to a decreasing dispersion relation $\omega(k)$ for increasing magnitude of the wavenumber $|k|$. The previous study of lumped-element metamaterial resonator includes the implementation of room-temperature metamaterial resonators and antennas based on zeroth-order resonances [44], leaky wave antennas [45], and novel directional couplers [46]. There have been efforts to develop metamaterial resonators from high-temperature superconducting films in order to address the effects of resistive losses in the lumped elements [47]. Superconducting metamaterials using Josephson elements in the array lattice have also been reported [48–51]. There are also proposals for using superconducting metamaterials for analog quantum systems to simulate the spin-boson model [3] and to investigate the quantum effects in the circuit analog of Hawking radiation [52]. Other applications of superconducting metamaterials include the generation of multi-partite entanglement [3], the enhancement, inhibition, and coherent control of light-matter interactions [53, 54], quantum-limited amplification of microwave signals [55], and coherent wavelength conversion [56]. Inspired by Ref. [3], simultaneous multi-mode strong coupling can be realized by coupling a qubit to a hybrid line resonator consisting of both left-handed and right-handed sections.

In this thesis, I will present the design, fabrication, and low-temperature microwave measurements to characterize the mode structure of a superconducting metamaterial resonators, along with Laser Scanning Microscope (LSM) imaging experiments to visualize the microwave field distributions. The measured spectrum of metamaterial resonators exhibits

a high density of modes as expected. The LSM imaging results illustrate the standing wave patterns for metamaterials. In addition, I compare the experimental measurements with numerical simulations, electromagnetic field (EM) simulations, as well as analytic calculations. All of these approaches are in reasonable agreement with the experimental results. Some important analytic results, such as the coupling quality factors of discrete transmission line resonators, will be introduced for the first time. In Chap. 2, I will introduce the general idea of left-handed metamaterials. I will discuss the conventional right-handed transmission line in Chap. 3 and the left-handed transmission line in Chap. 4. In Chap. 5, I will discuss the properties of resonators for cQED made by left-handed transmission line. Chapters 6-8 describe the realization, measurements, and comparison with simulations of the superconducting metamaterial resonator. Chapter 9 is about the initial implementation of the metamaterial resonator in cQED where a flux tunable transmon qubit is coupled to the metamaterial. The fabrication process will be described in Chap. 10.

Chapter 2

Introduction of left-handed material

In uniform isotropic linear materials, the supported electromagnetic (EM) plane waves have electric field $\vec{E}$, magnetic field $\vec{B}$ and the wave vector $\vec{k}$ obeying the right hand rule. Meanwhile, the Poynting vector $\vec{S}$ of the EM wave is also along the same direction with $\vec{k}$ since:

$$\vec{S} = \vec{E} \times \vec{H}, \tag{2.1}$$

where $\vec{H}$ is proportional to $\vec{B}$ as $\mu\vec{H} = \vec{B}$ [57]. According to the right hand rule, the direction of $\vec{E}$ and $\vec{B}$ will automatically define the directions of the EM wave and the energy flow. The EM response of such systems is considered "right-handed", where the vacuum is a simple example.

In optics, the index of refraction, n, describes how light propagates through the medium as ratio of the phase velocity, v compared to the speed of light in free space, c:

$$n = \frac{c}{v}. \tag{2.2}$$

When light passes through two media with different indices of refraction, it will change direction and appears to be refracted. The sines of the angles of incidence and refraction are

found to have the inverse of the ratio of the phase velocites (Fig. 2.1a):

$$\frac{\sin\theta_1}{\sin\theta_2} = \frac{v_1}{v_2} = \frac{n_2}{n_1}, \tag{2.3}$$

which is called the Snell's law [58]. The result is well known and often used to explain the refracted image of an object in water. The index of refraction can also be written as

$$n = \sqrt{\epsilon_r \mu_r}, \tag{2.4}$$

where ϵ_r is the material's relative permittivity, and μ_r is its relative permeability [59]. It is not clear how EM waves would propogate in a material where both permittivity and permeability are nagetive. In 1967 (published in 1968), Veselago discussed this type of situation [28] for the first time. In Ref. [28], he showed that having simultaneous negative permittivity and permeability would result in $\vec{E}$, $\vec{B}$ and the wave vector $\vec{k}$ forming a left-handed set. To prove it, we consider the normal Maxwell's equations in a charge and current free space:

$$\nabla \times \vec{E} = -\frac{\partial \vec{B}}{\partial t} \tag{2.5}$$

$$\nabla \times \vec{H} = \frac{\partial \vec{D}}{\partial t} \tag{2.6}$$

$$\nabla \cdot \vec{D} = 0 \tag{2.7}$$

$$\nabla \cdot \vec{B} = 0. \tag{2.8}$$

These allow a well-known set of plane wave solutions for frequency ω and wavevector $\vec{k}$ [57]:

$$E = E_0 e^{i(k\cdot x - \omega t)} \tag{2.9}$$

$$H = H_0 e^{i(k\cdot x - \omega t)}. \tag{2.10}$$

Under conditions Eqs. (2.7)-(2.8), we have:

$$E = E_0 e^{i\left(\vec{k}\cdot\vec{x}-\omega t\right)} \tag{2.11}$$

$$B = B_0 e^{i\left(\vec{k}\cdot\vec{x}-\omega t\right)} \tag{2.12}$$

$$\left|\frac{E_0}{B_0}\right| = v = \frac{1}{\sqrt{\mu\epsilon}}. \tag{2.13}$$

This plane wave has the wave vector $\vec{k}$, $\vec{E}$ and $\vec{B}$ forming a right-handed set. For linear isotropic media, we have:

$$\mu\vec{H} = \vec{B} \tag{2.14}$$

$$\epsilon\vec{E} = \vec{D}. \tag{2.15}$$

The first two Maxwell's equations can be written as:

$$\nabla \times \vec{E} = -\mu\frac{\partial\vec{H}}{\partial t} \tag{2.16}$$

$$\nabla \times \vec{H} = \epsilon\frac{\partial\vec{E}}{\partial t}. \tag{2.17}$$

If ϵ and μ are simultaneously negative, like $\tilde{\epsilon} = -|\epsilon|$ and $\tilde{\mu} = -|\mu|$, Eq. (2.16) and (2.17) can be rewritten as:

$$\nabla \times \vec{E} = -\tilde{\mu}\frac{\partial\vec{H}}{\partial t} \Rightarrow \nabla \times \vec{E} = -\mu\frac{\partial\left(-\vec{H}\right)}{\partial t} \tag{2.18}$$

$$\nabla \times \vec{H} = \tilde{\epsilon}\frac{\partial\vec{E}}{\partial t} \Rightarrow \nabla \times \left(-\vec{H}\right) = \epsilon\frac{\partial\vec{E}}{\partial t}. \tag{2.19}$$

The solutions can be found as:

$$E = E_0 e^{i\left(-\vec{k}\cdot\vec{x}-\omega t\right)} \tag{2.20}$$

$$H = H_0 e^{i\left(-\vec{k}\cdot\vec{x}-\omega t\right)}. \tag{2.21}$$

Compared with Eqs. (2.9-2.10), the minus sign in the exponential term indicate that $\vec{k}$, $\vec{E}$ and $\vec{B}$ (which is $\mu\vec{H}$) now form a left-handed set. This type of material is thus referred to as a "left-handed" material. However, the energy flowing vector in Eq. (2.1) is always the right-handed product of $\vec{E}$ and $\vec{H}$ (which is in linear of $\vec{B}$ here). So, in a left-handed material, the transmitted EM wave will have the phase velocity and the energy flowing in the opposite direction. And since phase velocity $v_p = \omega/k$ is in the direction of $\vec{k}$ while group velocity $v_g = \partial\omega/\partial k$ is in the direction of $\vec{S}$, plane wave propagating in left-handed medium would have the v_p and v_g going in opposite directions.

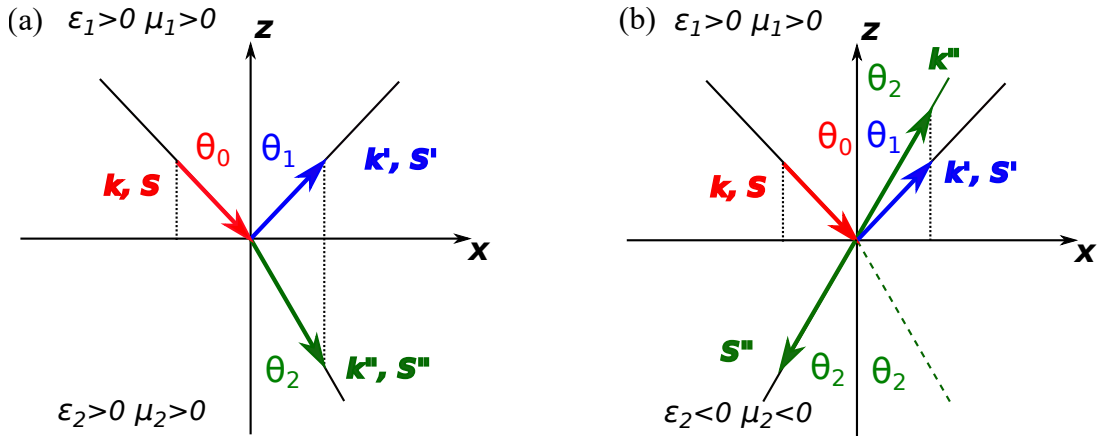

Figure 2.1: Illustration of how the EM wave refracts between two media. Red is the incident wave with $\vec{k}$ and $\vec{S}$, green is the refracted wave with $\vec{k'}$ and $\vec{S'}$, blue is the reflected wave with $\vec{k''}$ and $\vec{S''}$. The upper area where $z > 0$ is the medium 1 and the lower area where $z < 0$ is medium 2. The $z = 0$ plane is the interface. An EM plane wave travels from medium 1 to the medium 2. For simplicity without loosing generality, we consider the incident wave with $k_y = 0$, which means it will be confined in the $y = 0$ plane. (a) Normal situation where the media on both side of the interface have positive ϵ and μ. The refracted wave will be on the opposite side of the normal respect to the incident wave. (b) Negative index of refraction case that the medium on the bottom has both negative permittivity and permeability and the refracted wave is on the same side of normal respect to the incident wave. The energy $\vec{S''}$ flows into the medium 2 but the wave front $\vec{k''}$ is pointing the opposite direction. The reflected wave are the same for two different situations that $\theta_0 = \theta_1$.

More interestingly, when an EM wave travels from right-handed medium to left-handed medium, Eq. (2.4) is no longer valid and the index of refraction is actually negative. On the interface, the boundary condition requires the tangential part of $\vec{k}$ to be continuous. For

normal media, this leads to the Snell's law shown in Fig. 2.1(a). However, if the first medium has $\epsilon_1 > 0$ and $\mu_1 > 0$, while the second medium has $\epsilon_2 < 0$ and $\mu_2 < 0$ (or vice versa), the refracted wave will be bent to the same side of normal with respect to the incident wave. When the wave crosses the boundary, the tangential part of $\vec{k''}$ is still continuous, but $\vec{k''_z}$ switches direction because k_z is negative in medium 2. This causes the total wave vector $\vec{k''}$ to follow in the direction of the green arrow shown in the Fig. 2.1(b), and the energy $\vec{S''}$ flows in the opposite direction of $\vec{k''}$. Thus, in this case, the "left-handed Snell's law" is:

$$\frac{\sin\theta_1}{\sin\theta_2} = -\frac{n_2}{n_1}. \tag{2.22}$$

Eq. 2.22 suggests that medium 2 has a negative index of refraction.

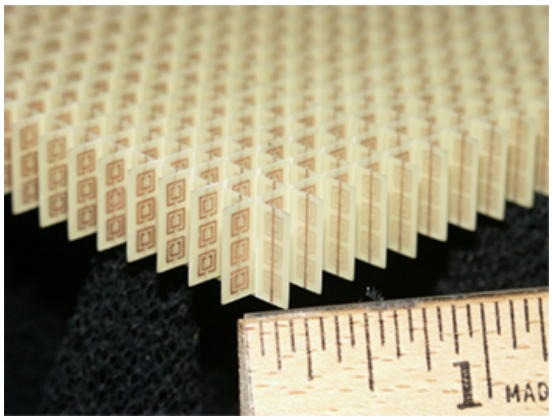

Figure 2.2: A metamaterial flat lens built by NASA with 2-D array of split-ring resonators [1]. The total array consists of 3 by 20×20 unit cells with overall dimensions of $10\times100\times100$ mm.

So far, scientists have not discovered any material that naturely exhibits both negative permittivity and permeability. However, this doesn't mean we cannot make a left-handed material. Engineers have developed metamaterials which can allow us to achieve desired EM properties from natural materials. Metamaterials are built by a series of individual unit cells arranged in a particular format. Each cell is normally much smaller than the EM wavelength and is designed so the combined structure can have some extraordinary properties in a certain frequency range of interest. Various types of metamaterials with left-handed properties have

been developed [1, 60–62]; we will focus here on one-dimensional circuit-based metamaterials.

To conclude, in this chapter, I have discussed materials with simultaneous negative permittivity and permeability and explained why they would exhibit negative index of refraction. I have also explained why they are called left-handed materials: the EM wave propagating in this material will have $\vec{E}$, $\vec{B}$ and $\vec{k}$ forming a left-handed set. No naturally found material exhibits this interesting property, so it can only be made by metamaterials.

Chapter 3

Conventional transmission lines

Superconducting transmission line resonators with high quality factors are used in cQED for readout and control of superconducting qubits [63–67] along with applications in quantum information storage [68–70] and qubit-qubit coupling [12, 71]. In this chapter, we discuss the general type of transmission line which includes microstrip, coaxial, or other two-port transmission lines and then we review the most typical conventional transmission-line resonator used in cQED formed from a coplanar waveguide (CPW) layout. Most derivations in this chapter are following Ref [72].

3.1 Circuit model of transmission line

It's commonly known that the normal metal type conducting wire is not a good material to carry high frequency AC current: it faces multiple problems, including significant losses due to the skin effect, and also the fact that such a single wire will have a significant impedance at high frequencies [57]. A much better approach for delivering high frequency electrical signals involves the use of two or more conductors in a transmission line (TL) configuration. By definition, a transmission line is a specialized cable or other structure designed to conduct alternating current of radio frequency.

A simple TL can be treated as a two-port network with impedance Z_0 as in Fig. 3.1a.

It can also be modeled as an infinite one-dimensional array of lumped elements, which are

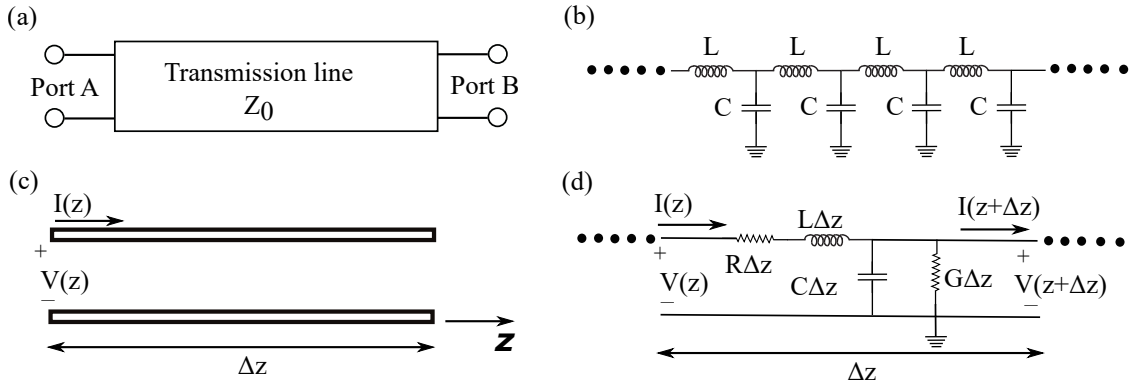

Figure 3.1: Transmission line circuit diagram. (a) Transmission line symbol: a two-port network with impedance Z_0. (b) Lumped element circuit model of lossless TL: an infinite network with series inductance and shunt capacitance. (c) Voltage and current definition in the TL. (d) Voltage and current defined within a unit cell for a lossy TL. $V(z)$ is the voltage applied on unit cell at z and $I(z)$ is the current through the same cell.

idealized electrical components, with unit cells size $\Delta z \to 0$, series inductance per unit length L, with series resistance per unit length R, and shunt capacitance per unit length C in parallel with shunt conductance per unit length G, as shown in Fig. 3.1(b,d) [72]. Applying Kichhoff's laws to the circuit in Fig 3.1(d), we get:

$$V(z) - V(z + \Delta z) = I(z)(R\Delta z + j\omega L\Delta z) \tag{3.1}$$

$$I(z) - I(z + \Delta z) = V(z + \Delta z)(G\Delta z + j\omega C\Delta z). \tag{3.2}$$

Here j is used as the imaginary unit instead of i to avoid any confusion between the current i and $\sqrt{-1}$, which is a engineering convention and will be used for the rest of this thesis. Dividing both sides by Δz and taking the limit of $\Delta z \to 0$, we get:

$$\frac{\partial V}{\partial z} = -I(R + j\omega L) \tag{3.3}$$

$$\frac{\partial I}{\partial z} = -V(G + j\omega C). \tag{3.4}$$

The above two equations can be solved simultaneously to get wave equations for $V(z)$ and

$I(z)$:

$$\frac{d^2V(z)}{dz^2} = \gamma^2 V(z) \tag{3.5}$$

$$\frac{d^2I(z)}{dz^2} = \gamma^2 I(z), \tag{3.6}$$

where

$$\gamma = \sqrt{(R + j\omega L)(G + j\omega C)} \tag{3.7}$$

is the complex propagation constant. The traveling wave solutions to Eqs. (3.5)-(3.6) are:

$$V(z) = V_0^+ e^{-\gamma z} + V_0^- e^{\gamma z} \tag{3.8}$$

$$I(z) = I_0^+ e^{-\gamma z} + I_0^- e^{\gamma z}. \tag{3.9}$$

Here, the negative exponential term indicates a wave traveling in the positive-z direction while the positive exponential term is the wave traveling in the negative-z direction. Applying Eqs. (3.8)-(3.9) to Eqs. (3.3)-(3.4), we get:

$$I(z) = \frac{\gamma}{R + j\omega L}\left(V_0^+ e^{-\gamma z} - V_0^- e^{\gamma z}\right). \tag{3.10}$$

We can relate the voltages and currents in the traveling waves by the characteristic impedance

$$\frac{V_0^+}{I_0^+} = \frac{-V_0^-}{I_0^-} = Z_0, \tag{3.11}$$

where Z_0 is defined as:

$$Z_0 = \sqrt{\frac{R + j\omega L}{G + j\omega C}}. \tag{3.12}$$

Thus, for an ideal lossless TL with $R = G = 0$, we have:

$$Z_0 = \sqrt{\frac{L}{C}}. \tag{3.13}$$

The typical superconducting TL that would be used in cQED has rather small losses, in which case Eq. (3.13) is a good approximation.

Following Eq. (3.7), we have[1]

$$\gamma = \alpha + j\beta, \tag{3.14}$$

and for ideal case

$$\alpha = 0 \tag{3.15}$$

$$\beta = \omega\sqrt{LC}, \tag{3.16}$$

where $\beta \propto \omega$ gives a linear dispersion. This also gives us the phase velocity and group velocity of:

$$v_p = \frac{\omega}{\beta} = \frac{1}{\sqrt{LC}} \tag{3.17}$$

$$v_g = \frac{\partial\omega}{\partial\beta} = \frac{1}{\sqrt{LC}}. \tag{3.18}$$

Both velocities are positive and identical, indicating that a lossless TL will have a linear dispersion relation. In the language of metamaterials discussed in the previous chapter, this would be described as a right-handed medium.

3.2 Terminated transmission line

Using a coplanar wave-guide (CPW) type of TL to form a circuit cavity requires knowledge of how the standing wave is distributed inside the TL. Here we consider the signal distribution for a TL with length l terminated with a load impedance Z_l at one end, as shown in Fig. 3.2.

Following Eq. (3.8) and (3.9), we will choose to make our origin at the right end $z = 0$ so that both exponential terms associated with V_0^+, I_0^+ and V_0^-, I_0^- are equal to 1 there. First,

[1]For the typical convention in Physics, this would be k, which is the magnitude of wave vector $\vec{k}$.

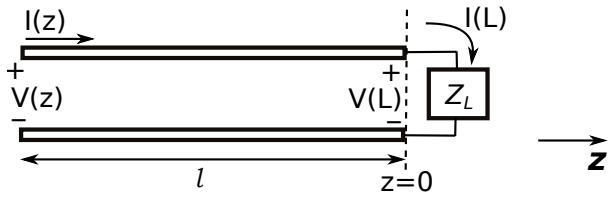

Figure 3.2: A transmission line terminated in a load impedance Z_l.

we consider a lossless case, with $I_0^+ = V_0^+/Z_0$ and $I_0^- = V_0^-/Z_0$, we have:

$$Z(0) = \frac{V_0^+ + V_0^-}{V_0^+ - V_0^-} Z_0 = Z_l. \tag{3.19}$$

This expression can be rearranged as follows:

$$V_0^- = \frac{Z_l - Z_0}{Z_l + Z_0} V_0^+. \tag{3.20}$$

Normally, the ratio of the amplitude of the reflected voltage wave to the amplitude of the incident wave is defined as the reflection coefficient, Γ [72]:

$$\Gamma = \frac{V_0^-}{V_0^+} = \frac{Z_l - Z_0}{Z_l + Z_0}. \tag{3.21}$$

In the limit of $Z_l \to \infty$, which corresponds to an open-end load, $\Gamma = 1$, while for $Z_l \to 0$, which corresponds to a short-end load, $\Gamma = -1$. Following the same method, we can easily prove that the current reflection coefficient is the same as the voltage reflection coefficient, thus the voltage and current at any point along the length of the TL can be:

$$V(z) = V_0^+ \left(e^{-j\beta z} + \Gamma e^{j\beta z}\right) \tag{3.22}$$

$$I(z) = \frac{V_0^+}{Z_0} \left(e^{-j\beta z} - \Gamma e^{j\beta z}\right), \tag{3.23}$$

where the input end of the TL is at $z = -l$. Thus, we can express the input impedance as:

$$Z_{in} = \frac{V_{-l}}{I_{-l}} = \frac{1 + \Gamma e^{-2j\beta l}}{1 - \Gamma e^{-2j\beta l}} Z_0. \tag{3.24}$$

Alternatively, we can use the definition of Γ from Eq. (3.21) in Eq. (3.24) to obtain [72]:

$$Z_{in} = Z_0 \frac{Z_l + jZ_0 \tan(\beta l)}{Z_0 + jZ_l \tan(\beta l)}. \tag{3.25}$$

If the loss factor for the TL α is not negligible, it is straightforward to show that [72]:

$$Z_{in} = Z_0 \frac{Z_l + Z_0 \tanh(\gamma l)}{Z_0 + Z_l \tanh(\gamma l)}. \tag{3.26}$$

3.3 Half-wave TL resonator

Eq. (3.25) is very important for understaning TL resonator and I'm going to discuss it in this section. The most typical one-dimensional TL resonators have boundary conditions so that the fundamental resonance is either a half-wavelength or quarter-wavelength standing wave pattern for the voltage and current. The half-wave resonator is made by adding small coupling capacitors on both ends to the environment to create big load impedance. The impedance is so large that it is a reasonable approximation to treat the input and load impedances as open circuits. This is called open-ended boundary condition. To simplify the calculation, we can treat load impedance as infinitely large, $Z_l \to \infty$. The quarter-wave resonator is formed by shorting one end of TL to the ground, making the load-impedance at that side equal to zero, $Z_l \to 0$, while the other end is coupled to the external circuitry through a coupling capacitor. For the remainder of this discussion, we will focus on half-wave resonators, but the physics of quarter-wave resonators is quite similar.

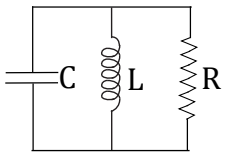

Figure 3.3: Parallel LCR circuit diagram

3.3.1 Parallel LCR resonator

Near resonance, a TL resonator can be modeled as a parallel LCR resonator formed from a lumped-element inductor, capacitor, and resistor [72, 73]. Here, we will briefly review the properties of a simple LCR resonator. The impedance of a parallel LCR circuit is given by:

$$Z_{in} = \left(\frac{1}{j\omega L} + j\omega C + \frac{1}{R} \right)^{-1}. \tag{3.27}$$

The quality factor Q is defined as the ratio of the energy stored in the LCR circuit to the energy dissipated by the resistor R per each cycle:

$$Q = \frac{E_{stored}}{E_{loss}}. \tag{3.28}$$

Following Ref. [72], it is straightforward to show that for a parallel LCR circuit, the quality factor can be expressed by:

$$Q = \omega_0 RC, \tag{3.29}$$

where ω_0 is the resonance frequency defined by

$$\omega_0 = 1/\sqrt{LC}. \tag{3.30}$$

Alternatively, the quality factor can be expressed as

$$Q = \frac{R}{Z_0}. \tag{3.31}$$

Near resonance, $\omega = \omega_0 + \Delta\omega$, we can rewrite Eq. (3.27) by:

$$Z_{in} \approx \frac{R}{1 + 2j\Delta\omega RC} = \frac{R}{1 + 2jQ\Delta\omega/\omega_0}. \tag{3.32}$$

3.3.2 TL half-wave resonator

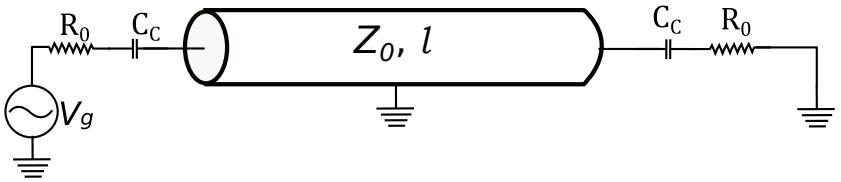

Figure 3.4: Circuit schematic of a TL half-wave resonator with external power source.

Now we will return to the TL half-wave resonator, and for now we will allow for the possibility of non-zero loss in the TL. As described previously, if we apply open-ended boundary conditions to a TL, it will form a half-wave resonator. In this case, from Eq. (3.21), we have $Z_l \to \infty$, so $\Gamma = 1$, also Eq. (3.26) would become:

$$Z_{in} = Z_0 \frac{1}{\tanh(\gamma l)}, \tag{3.33}$$

which can be rewritten as [72]:

$$Z_{in} = Z_0 \coth[(\alpha + j\beta) l] = Z_0 \frac{1 + j\tan(\beta l)\tanh(\alpha l)}{\tanh(\alpha l) + j\tan(\beta l)}. \tag{3.34}$$

At the fundamental half-wave resonance, we have: $\beta l = \pi$, since $\beta = 2\pi/\lambda$ and $l = \lambda/2$. Following the treatment of a parallel LCR resonator in Sec. 3.3 and the defintion of β [Eqs. (3.16)-(3.17)], we have

$$\beta l = \frac{\omega l}{v_p} = \frac{(\omega_0 + \Delta\omega) l}{v_p} = \pi + \frac{\pi\Delta\omega}{\omega_0}. \tag{3.35}$$

The $\tan(\beta l)$ term in Eq. 3.34 can be expanded for small $\Delta\omega$ as:

$$\tan(\beta l) = \tan\left(\frac{\Delta\omega\pi}{\omega_0}\right) \approx \frac{\Delta\omega\pi}{\omega_0}. \tag{3.36}$$

For small loss α, we can also approximate $\tanh \approx \alpha l$. By neglecting $\alpha l\Delta\omega/\omega_0$, i.e., the product of two small terms, Eq. (3.34) becomes [74]

$$Z_{in} \approx \frac{Z_0}{\alpha l + 2j\frac{\pi\Delta\omega}{2\omega_0}}. \tag{3.37}$$

Based on the similarity between Eq. 3.37 and the impedance of a parallel LCR resonator [Eq. (3.32)], we can use a parallel LCR resonator to approximate a half-wave TL resonator near resonance as follows [74]:

$$R = \frac{Z_0}{\alpha l} \tag{3.38}$$

$$C = \frac{\pi}{2\omega_0 Z_0} \tag{3.39}$$

$$L = \frac{1}{\omega_0^2 C}, \tag{3.40}$$

and

$$Q = \omega_0 RC = \frac{\pi}{2\alpha l} = \frac{\beta}{2\alpha}. \tag{3.41}$$

For a TL resonator, in addition to the fundamental mode, we can also consider higher harmonic resonances, where $\beta l = (n+1)\pi$, corresponding to $\omega_n = n\omega_0$. Thus, for higher order resonances, near resonance, Eq. (3.35) and (3.36) become:

$$\beta l = n\pi + \frac{\pi\Delta\omega}{\omega_0} \tag{3.42}$$

$$\tan(\beta l) \approx \frac{n\pi\Delta\omega}{\omega_n}. \tag{3.43}$$

Eq. (3.37) now become [74]:

$$Z_{in,n} = \frac{Z_0}{\alpha l + 2j\left(\frac{n\pi}{2}\right)\left(\frac{\Delta\omega_n}{\omega_n}\right)}. \tag{3.44}$$

Continuing the correspondence of mode n of an open-ended TL resonator with the equivalent parallel LCR resonator gives [74]:

$$R_n = \frac{Z_0}{\alpha l} \tag{3.45}$$

$$C_n = \frac{\pi}{2\omega_n Z_0} = \frac{\pi}{2Z_0\omega_0} \tag{3.46}$$

$$L_n = \frac{1}{\omega_n^2 C} = \frac{2Z_0}{\pi n^2 \omega_0} \tag{3.47}$$

$$Q_n = \omega_0 RC = \frac{n\pi}{2\alpha l}. \tag{3.48}$$

It is interesting to note that for the equivalent LCR model, the characteristic impedance is

$$Z_n = \sqrt{\frac{L_n}{C_n}} = \frac{2Z_0}{n\pi}, \tag{3.49}$$

which is no longer simply Z_0 for each mode, as is the case for the TL resonator [74].

3.3.3 Quality factor

Using the LCR model for TL resonances allows for a straightforward calculation of internal and coupling losses. Fig. 3.5(a) shows the circuit model of a parallel LCR circuit with coupling capacitors C_c to the input circuitry and a load impedance [8, 74]. The loading from the external resistor and capacitor will change the quality factor and the resonance frequency. As shown in Fig. 2.6(b), the Norton equivalent circuits for the input and output

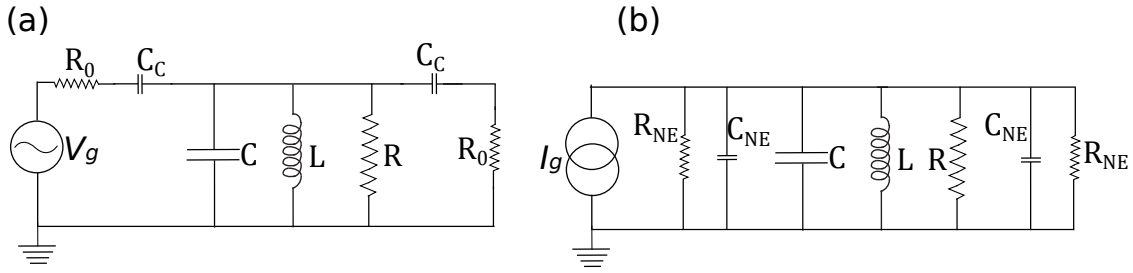

Figure 3.5: Diagram of (a) a loaded parallel LCR resonator circuit and (b) its Norton equivalent circuit.

circuitry can be written in the following way [8, 74]:

$$R_{NE} = \frac{1 + \omega_n^2 C_c^2 R_0^2}{\omega_n^2 C_c^2 R_0} \tag{3.50}$$

$$C_{NE} = \frac{C_c}{1 + \omega_n^2 C_c^2 R_0^2}. \tag{3.51}$$

Thus, the resulting circuit in Fig. 2.6(b) is a new parallel LCR circuit with effective $C_{eff} = 2C_{NE} + C$ and $R_{eff}^{-1} = 2/R_{NE}^{-1} + R^{-1}$. The new circuit will have a lower resonance frequency, ω_n^*, due to the higher effective capacitance and lower quality factor due to the lower effective resistance based on Eq. (3.30) and (3.31) [8]:

$$\omega_n^* = \frac{1}{\sqrt{L\left(C + 2C_{NE}\right)}} \tag{3.52}$$

$$Q_{ext,n} = \omega_n^* \frac{C + 2C_{NE}}{1/R + 2/R_{NE}} \tag{3.53}$$

In the limit where $C_c \ll C$, the shift of the loaded resonance frequency ω_n^* is negligible. So the loaded resonance frequency ω_n^* doesn't shift much:

$$\omega_n^* \approx \omega_n, \tag{3.54}$$

and the internal quality factor, which is the inverse of the loss due to R, is still:

$$Q_{int,n} = \omega_n R C_n = \frac{n\pi}{2\alpha l}, \tag{3.55}$$

while the combined external quality factor which is the inverse of the loss due to the two external resistors R_{NE} coupled through C_c is [74]:

$$Q_{ext,n} = \omega_n R_{NE} C_n \times \frac{1}{2} \approx \frac{n\pi}{4} \frac{1}{\omega_n^2 R_0 Z_0 C_c^2}. \tag{3.56}$$

With linear dispersion relation, $\omega_n = n\omega_0$, we have $1/Q_{ext,n} \propto n$. Thus, the coupling loss for a continuous TL half-wave resonator is linearly dependent on the mode number n. With the coupling loss determined, we can calculate the power in the resonator for a given external drive power [75, 76], which is very important in cQED. Since the total loss is the sum of both external loss and internal loss, the total Q should have the form of:

$$\frac{1}{Q} = \frac{1}{Q_{int}} + \frac{1}{Q_{ext}}. \tag{3.57}$$

The external quality factor is often noted as the "coupling quality factor", Q_c, and the internal quality factor is often written as Q_i.

3.3.4 Coplanar waveguide

The previous discussions apply to all types of TL. In cQED, the CPW type of transmission line is widely used. The CPW layout is a straightforward method for producing a transmission line with a single metallization layer on a dielectric substrate [72]. It consists of a single conducting trace in the center with a pair of ground planes on either side [77–79]. Fig. 3.6 shows the geometry of a conventional CPW.

To conclude, in this chapter, I have discussed the basic knowledge and properties, like the dispersion $\beta(\omega)$ and characteristic impedance Z_0, of conventional transmission lines and

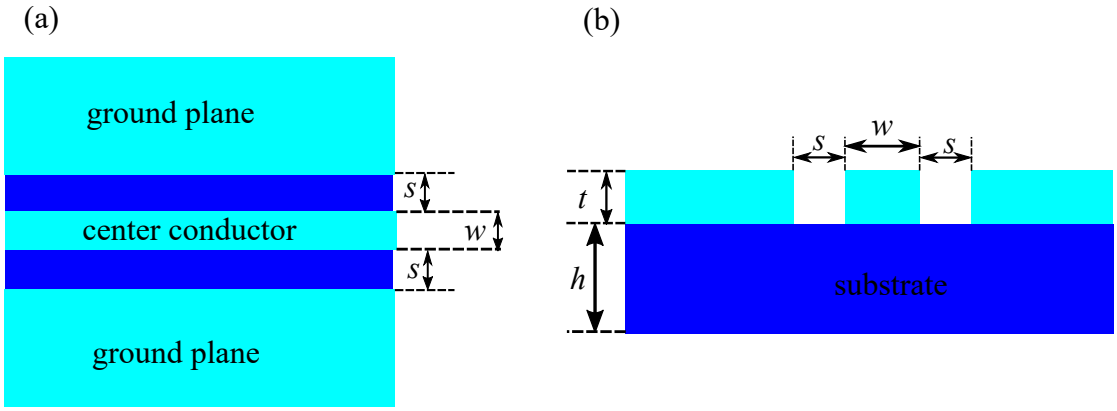

Figure 3.6: CPW geometry: (a) Top view of a CPW with center conductor width w and slot width s; (b) Side view of a CPW with film thickness of t on top a substrate with thickness of h.

properties of resonators like the coupling and internal quality factors.

Chapter 4

Left-handed transmission lines

The realization of left-handed materials in one dimension as left-handed transmission lines (LHTL) allows for the generation of novel dispersion relations in a system that is compatible with typical cQED layouts for coupling to qubits [3]. The LHTL supports EM waves with opposite propagation diretions for phase velocity and group velocity. The phenomenon of antiparallel phase and group velocity, or "backward waves" [80] has been known for some time, but the high intrinsic losses inherent in initial systems exhibiting these properties [81] limited the potential applications. In the early 21st century, researchers revisited LHTLs in a variety of contexts, including the development of novel microwave electronic devices [81–84]. The previous chapter in this thesis was about some well-know concepts of conventional transmission line and TL resonators. Now let's shift our focus to the exciting and interesting left-handed transmission line area.

4.1 LHTL: circuit model

It can be proved that a distributed LC network can be used to model the permeability and permittivity of a particular material with $L/m = \mu$ (H/m) and $C/m = \epsilon$ (C/m) [82, 85]. The discrete TL discussed in the previous chapter can be viewed as such a model of a 1D material. When Veselago originally proposed the concept of a negative index of refraction [28], which is

equivalent to the phase velocity being pointed in the opposite direction of group velocity, he showed that a material with simultaneously negative permittivity and permeability will fulfill the requirements [28]. Thus, there have been efforts to design LC networks to build such a left-handed material [41]. While it is unphysical for an individual inductor or capacitor to take on negative values, in a discrete TL, it is possible to produce the conditions for achieving left-handedness by swapping the positions of the inductors and capacitors [41, 43].

This type of design is essentially a series high-pass filter network [80, 81]. Although no naturally occurring material with left-handed properties has been discovered, we can build a left-handed TL using metamaterials composed of discrete, lumped-element components. Furthermore, we can fabricate such devices using superconducting traces to minimize the internal losses.

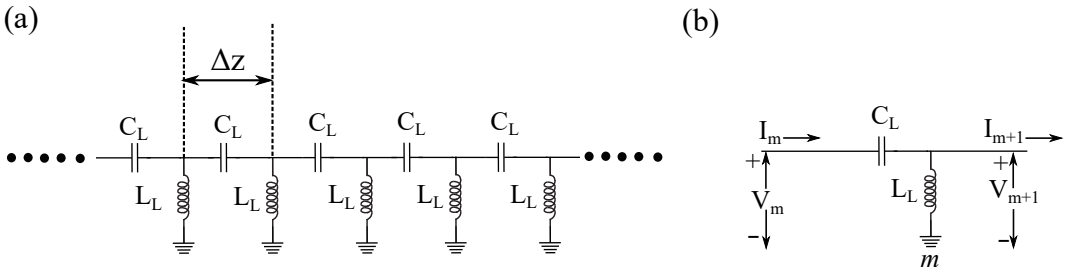

Figure 4.1: LHTL circuit model: (a) array of series capacitors C_L with shunt inductors L_L to ground; (b) definition of current and voltage supported by the LHTL at cell m.

Fig 4.1(a) shows a lossless left-handed transmission line (LHTL) circuit diagram, which is basically formed by swapping the L and C in the diagram of Fig. 3.1(b). The C_L (L_L) here is the capacitance (inductance) per unit cell which has an actual physical length of Δz. This means the LHTL is a discrete transmission line, with finite number of cells. In order to study the transmission properties of a LHTL, we can apply Kirchhoff's Law to the circuit

schematic in Fig. 4.1(b) to obtain:

$$V_m - V_{m+1} = I_m \left(\frac{1}{j\omega C_L} \right) \tag{4.1}$$

$$I_{m-1} - I_m = V_m \left(\frac{1}{j\omega L_L} \right) \tag{4.2}$$

$$V_{m-1} - V_m = I_{m-1} \left(\frac{1}{j\omega C_L} \right) \tag{4.3}$$

$$I_m - I_{m+1} = V_{m+1} \left(\frac{1}{j\omega L_L} \right). \tag{4.4}$$

We can use the admittance of the inductor $Y = 1/j\omega L_L$ and impedance of the capacitor $Z = 1/j\omega C_L$ to rewrite Eqs. (4.1)-(4.4) to obtain:

$$V_m[2 + ZY] = V_{m-1} + V_{m+1} \tag{4.5}$$

$$I_m[2 + ZY] = I_{m-1} + I_{m+1}. \tag{4.6}$$

We assume solutions for the wave propagating through the LHTL at cell number m with the following form:

$$V_m = V_0^+ e^{-j\beta m\Delta z} + V_0^- e^{j\beta m\Delta z} \tag{4.7}$$

$$I_m = I_0^+ e^{-j\beta m\Delta z} + I_0^- e^{j\beta m\Delta z}, \tag{4.8}$$

where Δz is the unit cell length and $\beta = 2\pi/\lambda$ is the magnitude of wavenumber. Using Eqs. (4.5)-(4.8), we arrive at:

$$[V_0^+ e^{-j\beta m\Delta z} + V_0^- e^{j\beta m\Delta z}][2\cos(\beta\Delta z) - (2 + ZY)] = 0. \tag{4.9}$$

For this expression to be true in general, the term in the second set of square brackets must

always be zero, which leads to the following condition:

$$2\cos(\beta\Delta z) = (2 + ZY), \tag{4.10}$$

which provides a relationship between $\beta\Delta z$ and ZY. Using standard trigonometric relationships combined with Eq. (4.10) leads to the following dispersion relation for an LHTL:

$$\omega_{LHTL} = \frac{1}{2\sqrt{L_L C_L}} \frac{1}{|\sin\left(\frac{\beta\Delta z}{2}\right)|}. \tag{4.11}$$

From Eq. (4.11), we can see that ω is a decreasing function of β. Since larger β means shorter wave-length, the largest possible value of $\beta\Delta x$ is π, corresponding to a wavelength of two unit cells; shorter wavelengths are unable to propagate in the LHTL. Thus, this type of discrete transmission line will have an infrared cut-off frequency, corresponding to the shortest wavelength:

$$\omega_{IR} = \frac{1}{2\sqrt{L_L C_L}}. \tag{4.12}$$

By substituting Eq. (4.7) into Eq. (4.1) and solving for i_m, one can then compare the result with Eq. (4.8) to obtain the following expressions for I_0^+ and I_0^-:

$$I_0^+ = 2je^{-j\beta\Delta z/2} \sin\left(\frac{\beta\Delta z}{2}\right) \frac{V_0^+}{Z} \tag{4.13}$$

$$I_0^- = -2je^{j\beta\Delta z/2} \sin\left(\frac{\beta\Delta z}{2}\right) \frac{V_0^-}{Z}. \tag{4.14}$$

Eq. (4.10) can be rewritten as:

$$2j \sin\left(\frac{\beta\Delta z}{2}\right) = \sqrt{ZY}, \tag{4.15}$$

which can be substituted into Eqs. (4.13)-(4.14) to yield:

$$I_0^+ = e^{-j\beta\Delta z/2}\frac{V_0^+}{Z_0} \tag{4.16}$$

$$I_0^- = -e^{j\beta\Delta z/2}\frac{V_0^-}{Z_0}, \tag{4.17}$$

with

$$Z_0 = \sqrt{\frac{L_L}{C_L}}, \tag{4.18}$$

which is now the characteristic impedance of the LHTL. Combining Eqs. (4.16)-(4.17)with Eq. (4.8), the current through unit cell m can then be rewritten as:

$$I_m = \frac{V_0^+}{Z_0}e^{-j\beta(m+\frac{1}{2})\Delta z} - \frac{V_0^-}{Z_0}e^{j\beta(m+\frac{1}{2})\Delta z}. \tag{4.19}$$

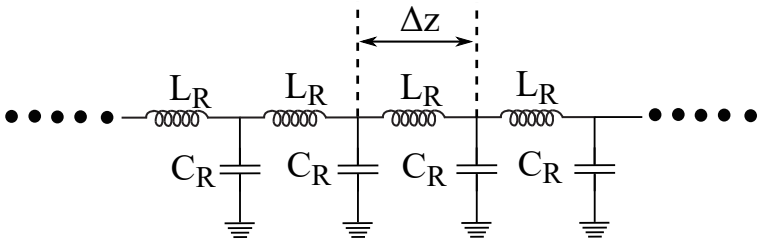

Figure 4.2: Circuit diagram of discrete right-handed transmission.

Although the treatment in Eqs. (4.1)-(4.10) was described in terms of a LHTL, this can be easily extended to treat a discrete right-handed transmission line RHTL as well. For example, a RHTL in Fig. 4.2 with $Z = j\omega L$ and $Y = j\omega C$ has the dispersion of:

$$\omega_{RHTL} = \frac{2}{\sqrt{L_R C_R}}\sin\left(\frac{\beta\Delta z}{2}\right). \tag{4.20}$$

For small $\beta\Delta z$, this becomes $\omega_{RHTL} \approx \beta\Delta z/\sqrt{L_R C_R}$. With continuum limit, $\Delta z \to 0$, and the definitions of $L = L_R/\Delta z$ and $C = C_R/\Delta z$, it is just $\beta = \omega\sqrt{LC}$. Similar to the LHTL, the maximum allowed value of $\beta\Delta z$ is π, corresponding to a wavelength of $2\Delta z$, but this

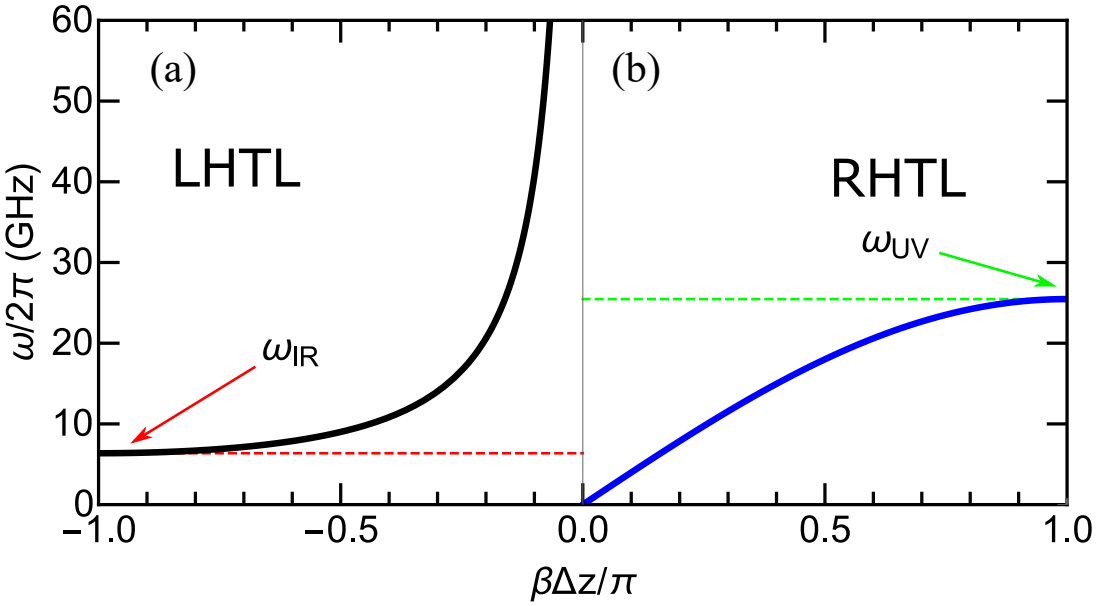

Figure 4.3: Dispersion relation of LHTL and discrete RHTL. (a) A LHTL dispersion with $\omega_{IR}/2\pi$=6 GHz. Due to its left-handed nature, β is negative which will be discussed in the next section. The dispersion is divergent at $\beta = 0$. (b) A discrete RHTL with $\omega_{UV}/2\pi$=25 GHz. At low frequency, the dispersion is close to linear which fits the continuous TL dispersion, as described in the previous chapter.

now occurs at high frequencies, and is thus an ultraviolet cutoff::

$$\omega_{UV} = \frac{2}{\sqrt{LC}}. \tag{4.21}$$

4.2 Continuum limit of discrete LHTL

Although the LHTL can only be realized using discrete metamaterial, to understand such a line in the continuum limit is still important.

Fig. 4.4 shows a circuit diagram of a LHTL in continuous limit. Following the same

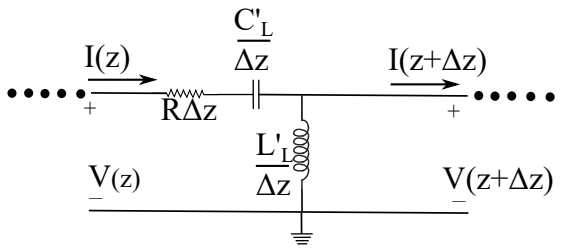

Figure 4.4: Voltage and current defined at positon z in imagined continuous LHTL unit cell diagram with times-unit-length parameters of ${C_L}'\,(F\cdot m)$ and ${L_L}'\,(h\cdot m)$. For simplicity, the loss only has series component, $R\,(\Omega/m)$.

analysis method in Sec. 3.1 for the continuous right-handed TL, we have:

$$V_z - V_{z+\Delta z} = I_z\left(\frac{\Delta z}{j\omega {C_L}'} + R\Delta z\right) \tag{4.22}$$

$$\left(I_z - I_{z+\Delta z}\right)\frac{j\omega {L_L}'}{\Delta z} = V_{z+\Delta z}, \tag{4.23}$$

which in the limit of $\Delta z \to 0$ become:

$$\frac{\partial V}{\partial z} = -\left(R + \frac{1}{j\omega {C_L}'}\right) I \tag{4.24}$$

$$\frac{\partial I}{\partial z} = -\frac{1}{j\omega {L_L}'} V, \tag{4.25}$$

and then can give:

$$\frac{\partial^2 V}{\partial z^2} = \left[-\left(R + \frac{1}{j\omega {C_L}'}\right)\left(-\frac{1}{j\omega {L_L}'}\right)\right] V \tag{4.26}$$

$$\frac{\partial^2 I}{\partial z^2} = \left[-\left(R + \frac{1}{j\omega {C_L}'}\right)\left(-\frac{1}{j\omega {L_L}'}\right)\right] I. \tag{4.27}$$

Similarly to Eqs. (3.5)-(3.6) in Sec.3.1, Eqs. (4.26)-(4.27) have solutions of:

$$V = V_0^+ e^{-\gamma z} + V_0^- e^{\gamma z} \tag{4.28}$$

$$I = I_0^+ e^{-\gamma z} + I_0^- e^{\gamma z} \tag{4.29}$$

$$\gamma = \pm\sqrt{(\frac{1}{j\omega {L_L}'})(R + \frac{1}{j\omega {C_L}'})}, \tag{4.30}$$

with characteristic impedance of

$$Z_0 = \sqrt{\frac{R + \frac{1}{j\omega {C_L}'}}{\frac{1}{j\omega {L_L}'}}}. \tag{4.31}$$

In a lossless case, it is just

$$Z_0 = \sqrt{\frac{{L_L}'}{{C_L}'}}. \tag{4.32}$$

Following Eq. (4.30), the absolute value of propagation constant γ can be rewrite as:

$$|\gamma| = \sqrt{\frac{R}{j\omega {L_L}'} - \frac{1}{\omega^2 {L_L}' {C_L}'}} = \frac{j}{\omega\sqrt{{L_L}' {C_L}'}}\sqrt{jR\omega {C_L}' + 1}. \tag{4.33}$$

When R is small, it becomes:

$$|\gamma| \approx \frac{j}{\omega\sqrt{{L_L}' {C_L}'}}\left(1 + \frac{1}{2} jR\omega {C_L}'\right) \tag{4.34}$$

$$= -\frac{1}{2}\frac{R}{Z_0} + j\frac{1}{\omega\sqrt{{L_L}' {C_L}'}}. \tag{4.35}$$

The real part of γ, which is α, is the loss so it can't be negative. Thus, we should have

$$\gamma = \frac{R}{2} - j\frac{1}{\omega\sqrt{{L_L}' {C_L}'}}, \tag{4.36}$$

and

$$\alpha = \frac{R}{2} \tag{4.37}$$

$$\beta = -\frac{1}{\omega\sqrt{L_L{}'C_L{}'}}. \tag{4.38}$$

Eq. (4.38) suggests that Eq. (4.11) should take the form of:

$$\omega_{LHTL} = -\frac{1}{\sqrt{L_L C_L}}\frac{1}{2\sin\left(\frac{\beta\Delta z}{2}\right)}. \tag{4.39}$$

In the lossless case with $\alpha = 0$, based on Eq. (4.38), β is negative. The phase velocity and group velocity can be found as:

$$v_p = \frac{\omega}{\beta} = -\omega^2\sqrt{L_L{}'C_L{}'} \tag{4.40}$$

$$v_g = \frac{\partial\omega}{\partial\beta} = \omega^2\sqrt{L_L{}'C_L{}'}. \tag{4.41}$$

They have the same magnitude and are both frequency dependent. The sign difference indicates they have different directions, which proves such a line is indeed left-handed. Similar treatment and analysis can be found in Refs. [43, 86].

4.3 Accounting for stray reactance in LHTL

For any practical metamaterial, the individual lumped elements will always have parasitic stray reactances that affect the behavior of the circuit. That means the inductor has its own parallel capacitance and the capacitor has its own series inductance [43, 83]. Thus, when we account for these stray reactances, our circuit becomes a composite left-handed/right-handed (LHRH) transmission line shown in Fig. 4.5. The unit cell series impedance is $Z = j\omega L_R + 1/j\omega C_L$ and the unit cell shunt admittance is $Y = j\omega C_R + 1/j\omega L_L$. Define the inductor's self-resonance frequency and capacitor's self-resonance frequency as $\omega_L =$

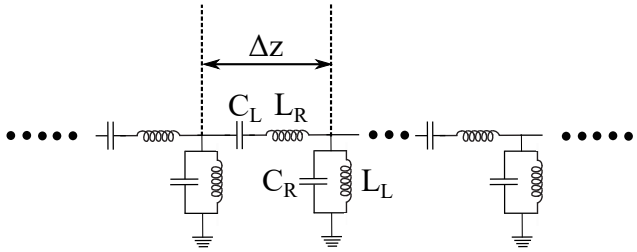

Figure 4.5: The circuit diagram of a LHRH transmission line, which is the LHTL with stray reactances included.

$1/\sqrt{L_L C_R}$ and $\omega_C = 1/\sqrt{C_L L_R}$, respectively. The earlier derivation for a simple LHTL can be easily extended for an LHRH with these new composite expressions for Z and Y so that Eq. (4.10) can be used to derive the dispersion relation for an LHRH:

$$\beta(\omega) = \frac{1}{\Delta z} \cos^{-1}\left[1 - \frac{1}{2}\left(\omega L_R - \frac{1}{\omega C_L}\right)\left(\omega C_R - \frac{1}{\omega L_L}\right)\right]. \tag{4.42}$$

We observe that this expression has solutions for both negative and positive values of β and we plot these in Fig. 4.6.

From Fig. 4.6, we can see that the LHRH dispersion has two branches: there is a left-handed branch at low frequency and is approaches the dispersion relation of a pure LHTL near ω_{IR}. For small, negative wavenumber, rather than diverging, as would be the case for an ideal LHTL with no stray reactance, the LHRH dispersion intersects the $\beta = 0$ line at the two self-resonance frequencies: $\min(\omega_L, \omega_C)$. Between the two self resonance frequencies, there is a gap with no propagating solutions, then a branch with right-handed dispersion begins at the larger of the two self-resonance frequencies, $\max(\omega_L, \omega_C)$. For even higher frequencies, there will eventually be an ultraviolet cutoff due to the discrete nature of the LHRH. The characteristic impedance of an LHRH will also be given by $\sqrt{Z/Y}$, but instead

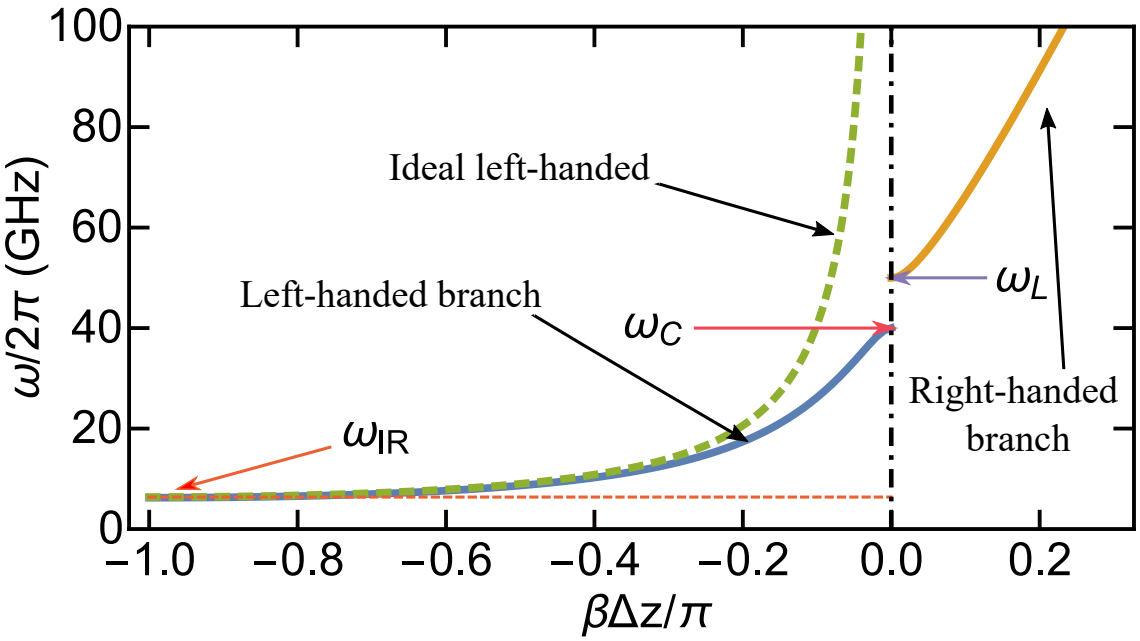

Figure 4.6: The dispersion relation of LHRH transmission line compared with pure LHTL dispersion. The $\omega_{IR}/2\pi$ is designed to be 6 GHz. The $\omega_C/2\pi$ and $\omega_L/2\pi$ are chosen to be 40 GHz and 50 GHz, respectively.

of being $\sqrt{L_L/C_L}$ for the ideal LHTL case, this becomes:

$$Z_0 = \sqrt{\frac{L_L}{C_L}}\sqrt{\frac{1-\omega^2 L_R C_L}{1-\omega^2 C_R L_L}} \tag{4.43}$$

$$= \sqrt{\frac{L_L}{C_L}}\sqrt{\frac{1-\omega^2/\omega_L^2}{1-\omega^2/\omega_C^2}}. \tag{4.44}$$

Although this characterstic impedance is frequency dependent, for typical parameters of the lumped elements for our metamaterials that will be described in the subsequent chapters, this will not deviate significantly from $\sqrt{L_L/C_L}$ over most of the frequency range of our experiments.

To conclude, in this chapter, I have discussed the basic knowledge and properties of the LHTL. The dispersion $\omega(\beta)$ of LHTL is a falling function of β, which results in v_p and v_g having different directions. The dispersion also makes high density of modes possible near low frequency end of LHTL spectrum. I've also discussed the stray reactance of the LHTL.

Chapter 5

Left-handed transmission line resonator

We discussed in Sec. 3.3 about the application of open-ended boundary condition using small coupling capacitors on either end of a transmission line for creating a resonant cavity with standing wave modes. In this chapter, we will apply a similar treatment to form standing-wave resonances with an LHTL. Since the LHTL is is always formed from a metamaterial, a resonator with fixed length l will have a total number of cells N. We will follow the notation from the previous chapter, with a shunt inductance L_L, series capacitance C_L, unit cell size Δz, and coupling capacitances C_c at either end of the LHTL. We will focus on layouts with symmetric coupling between the input and output, but it is straightforward to extend our treatment to situations with asymmetric coupling.

5.1 Ideal LHTL resonator

First, we will consider an ideal LHTL, which does not have any stray reactances. The dispersion relation is given by Eq. (4.39). For simplicity, let's fold the dispersion around the wavenumber axis so that the plot will fall in the first quadrant, as shown in Fig. 5.1 with $\omega_{LHTL} = 1/2\sqrt{L_L C_L}\sin(\beta\Delta z/2)$. As shown in Sec. 3.3 for a RHTL, the open-ended

boundary condition corresponds to a half-wave fundamental resonance with the resonance condition of $\beta l = n\pi$, $n = 0, 1, 2, \ldots, N$. Using the fact that $l = N\Delta z$, we obtain the following relationship:

$$\beta\Delta z = \frac{n\pi}{N}. \tag{5.1}$$

From Fig. 5.1 we can see that the dispersion diverges at high frequency, there is no $n = 0$ mode, which means $n \neq 0$. Also, mode with $n = N$ has infinite coupling quality factor according to Sec. 5.5, which will be discussed later, meaning the resonance is not measurable, thus $n \neq N$. Thus for a LHTL resonator of N unit cells, we shall have $N - 1$ different resonance modes. Due to the left-handed nature of the dispersion, the small number mode, which correspond to long wavelengths, are at high frequency. At the same time, the high$-n$ modes with short wavelengths correspond to the lowest frequencies. Near the infrared cut-

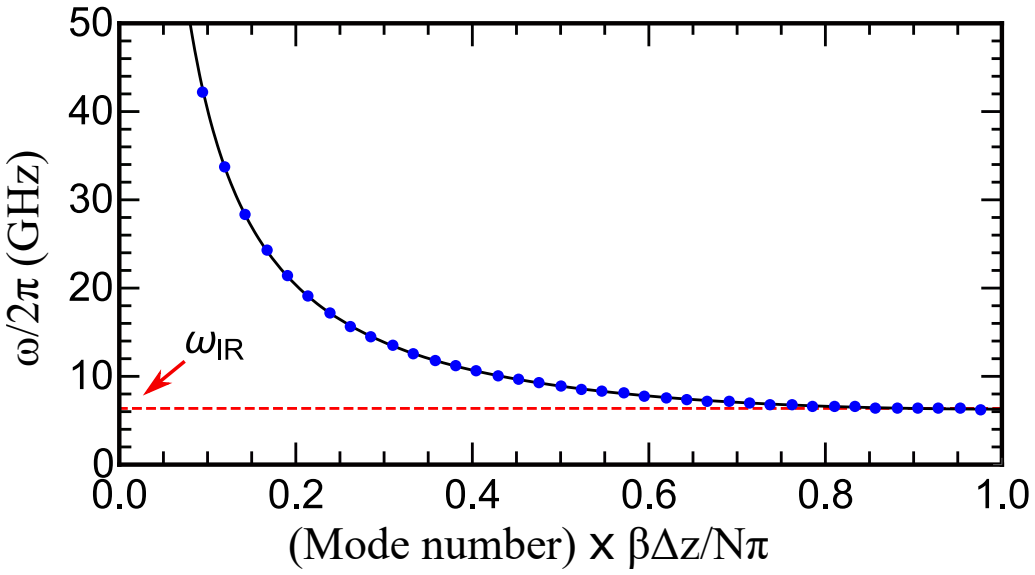

Figure 5.1: Dispersion relation of a LHTL resonator with normalized mode number. The blue points here correspond to the resonant modes where $\beta\Delta z = n\pi/N$, while the black line is the LHTL dispersion relation from Eq. (4.11) from Chap. 4. The parameters are chosen as $N = 42$, $C_L = 250$ fF and $L_L = 0.625$ nH.

off, the mode spacing is very small due to the flatness of the band there. From the example plot in Fig. 5.1, the lowest five resonances fall within a 100 MHz range. That means in a

very narrow frequency range, we can have multiple orthogonal resonances.

This potential for generating a high density of modes in a superconducting structure that is compatible with cQED provides a new pathway for generating novel mode spectra for coupling to qubits. As discussed in Chap. 1, we can use a conventional RHTL resonator, perhaps patterned with a CPW layout, to achieve high density of modes. However, due to the linear dispersion, in order to make the mode spacing in 10 MHz range, the fundamental mode has to be 10 MHz or less. This results in an ultra-long resonator [22], which can be impossible to fit on a typical 8×8 mm^2 cQED chip size. This introduces challenges with processing and cooling to mK temperatures, as well as the potential for low-frequency package modes. In addition, such a cavity will have resonance modes in the entire qubit frequency range so the qubit will always be coupled to the cavity. This could make qubit readout challenging and the relaxation will be strongly impacted by the Purcell effect due to coupling to all of the various modes [87]. An alternate approach involves a multimode scheme with multiple CPW resonators coupled together [25], but this still requires a rather large area. However, a LHTL resonator naturally has a ultra-high density of modes at frequencies near the infrared cut-off for the qubit to couple to. It is straightforward to design the unit cell parameters for a particular ω_{IR}, mode spacing, and size. In addition, the qubit can always be prepared at a frequency far below the cut-off without strongly interacting with the cavity. All of these potential advantages drive us to pursue the realization of LHTL cavities.

5.2 LHRH transmission line resonator

As described in the previous chapter, an LHTL cavity built by actual circuit elements will always have parasitic reactances, which may sound like undesirable properties. But in fact, such stray reactances could actually be beneficial for making the mode spacing even smaller. As shown in Fig. 5.2, due to the self-resonance frequencies of capacitors and(or) inductors,

the dispersion $\omega(\beta)$ gets pushed down at high frequency, which reduces the mode spacing between all the modes since the same number of modes will now be compressed into a smaller frequency span. Meanwhile, the structure can now support an $n = 0$ mode: At the two self-resonance frequencies, the resonance will have infinite wavelength, which leads to essentially no series loss since all the cells will have the same potential and no current will be flowing through the cell which eliminates dissipation [44]. We call the this type of general resonator the Left-handed/Right-handed (LHRH) TL resonator. Because our microwave

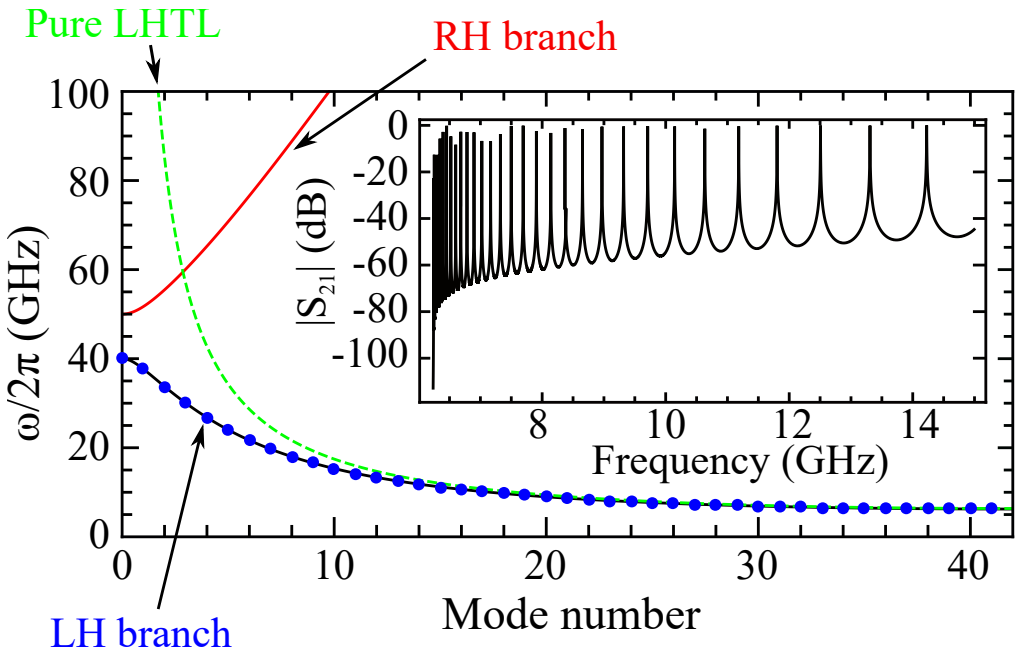

Figure 5.2: LHRH transmission line resonator dispersion plotted in solid line from Eq. (4.42) compared with a pure LHTL dispersion plotted in dashed line. The LHRH resonator has two braches: The bottom (black line) is the left-handed branch and the top (red line) is the right-handed branch. The parameters are chosen as $\omega_{IR}/2\pi = 6.36$ GHz and the two self-resonance frequencies are 40 GHz and 50 GHz. The LH branch agrees well with a pure LHTL dispersion which has the same ω_{IR} at the low frequency end. The LHRH resonator has 42 cells and the blue dots are the resonance frequencies of all 42 modes including the $n = 0$ mode on the LH branch of the dispersion. is a simulated transmission $|S_{21}(f)|$ spectrum of the LHRH resonator simulated by AWR near the low frequency end.

electronics hardware and cabling typically operates in the 1-20 GHz range, the dispersion relation of a practical LHRH resonator that we would fabricate will be dominated by the

left-handed branch. Similarly to an ideal LHTL resonator, in the left-handed branch, the LHRH resonator shall have N different modes including the $n = 0$ mode. Thus, for certain values of L_L and C_L, more cells will result in more modes and smaller mode spacing. We can also increase the density further by intentionally adding stray reactance to drive the high-frequency gap down to lower frequencies to compress the spectrum.

5.3 Terminated LHRH transmission line impedance

In order to develop a quantitative understanding of the properties of a lossless LHRH resonator, we consider such a circuit with a load impedance Z_l at the output end and input circuitry at the input end, as shown in Fig. 5.3.

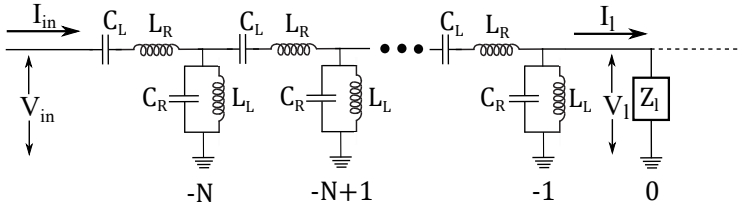

Figure 5.3: The circuit diagram of a lossless LHRH transmission line with load impedance Z_l on the right end. For calculational convenience, the loaded end is marked as $m = 0$. The first cell counting from the input end of the metamaterial is the $m = -N$ cell and the last cell is $m = -1$ cell, which gives total number of cell as N.

Equations (4.7) and (4.19) give us the voltage and current in a given discrete TL as functions of cell number m. To simplify the calculation, load impedance position will be defined as the zeroth cell, $m = 0$, but not a unit cell in the metamaterial. The reflection coefficient Γ is defined the same as in Eq. (3.21), which is V_0^-/V_0^+. Thus, we have the current and voltage at $m = 0$:

$$V_0 = V_0^+ + \Gamma V_0^+ \tag{5.2}$$

$$I_0 = \frac{V_0^+}{Z_0} e^{-j\beta\frac{\Delta z}{2}} - \frac{\Gamma V_0^+}{Z_0} e^{j\beta\frac{\Delta z}{2}}, \tag{5.3}$$

from which we can compute the impedance at $m = 0$, $Z_0 = V_0/I_0$:

$$Z_{m=0} = Z_0 \frac{1+\Gamma}{e^{\frac{-j\beta\Delta z}{2}} - \Gamma e^{\frac{j\beta\Delta z}{2}}}. \tag{5.4}$$

At cell 0, we require that $Z_m = Z_l$. Thus we have

$$\Gamma = \frac{Z_l e^{\frac{-j\beta\Delta z}{2}} - Z_0}{Z_l e^{\frac{j\beta\Delta z}{2}} + Z_0}. \tag{5.5}$$

which corresponds to the limit $Z_l \to \infty$, Γ has the form of:

$$\Gamma_{Z_l\to\infty} = e^{-j\beta\Delta z}, \tag{5.6}$$

which, unlike the continuous TL resonator with open-ended boundary condition [72], is not simply equal to one. With the reflection coefficient calculated, we can then calculate the impedance from the input end, with the left end cell number being $-N$. Thus, based on Eqs. (4.7-4.19) we have

$$V_{-N} = V_0^+ e^{j\beta N\Delta z} + \Gamma V_0^+ e^{-j\beta N\Delta z} \tag{5.7}$$

$$I_{-N} = \frac{V_0^+}{Z_0} e^{-j\beta(-N+\frac{1}{2})\Delta z} - \Gamma \frac{V_0^+}{Z_0} e^{j\beta(-N+\frac{1}{2})\Delta z}, \tag{5.8}$$

which yields:

$$Z_{-N} = Z_0 \frac{e^{j\beta N\Delta z} + \Gamma e^{-j\beta N\Delta z}}{e^{-j\beta(-N+\frac{1}{2})\Delta z} - \Gamma e^{j\beta(-N+\frac{1}{2})\Delta z}}. \tag{5.9}$$

Eq. (5.9) is the input impedance of a metamaterial LHRH transmission line with impedance Z_0 [Eq. (4.44)] and wavenumber $\beta\Delta z$ [Eq. (4.42)] loaded by an impedance Z_L corresponding to a reflection coeffeicient Γ [Eq. (5.5)]. It is important to note that this derivation is quite general and can be easily extended to other types of discrete TL resonators with different $\beta\Delta z$, Z_0, and Γ.

5.4 S_{21} parameter calculation

An important measurement quantity for characterizing a $n-$port microwave device is the scattering parameter, or S parameter, matrix. In Fig. 5.4(a), we show the schematic for a 2-port network, with S parameters defined in terms of the power relationship of the outgoing wave b_1, b_2 to the incoming wave a_1, a_2 [72, 88, 89]:

$$\begin{bmatrix} b_1 \\ b_2 \end{bmatrix} = \begin{bmatrix} S_{11} & S_{12} \\ S_{21} & S_{22} \end{bmatrix} \times \begin{bmatrix} a_1 \\ a_2 \end{bmatrix}.$$

In the transmission line cavity setup, the S parameter, S_{21}, characterizes the transmission

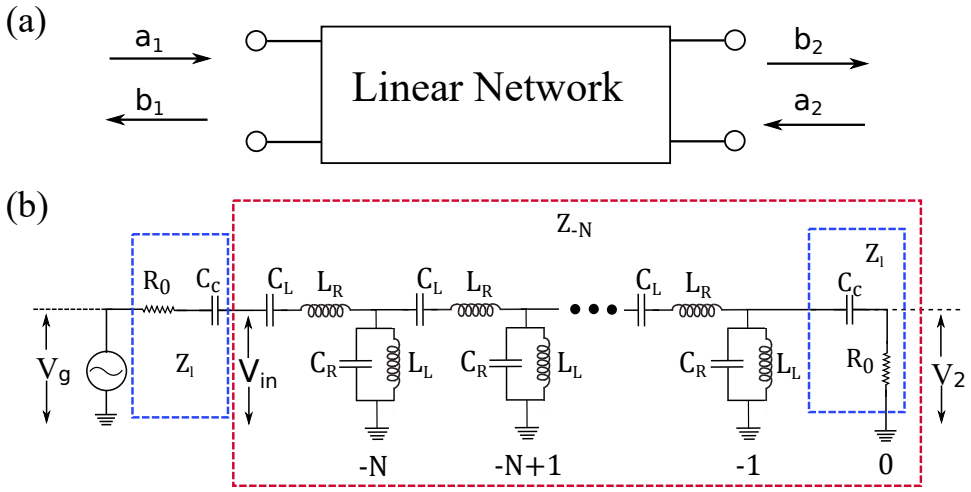

Figure 5.4: (a) The schematic of a general 2-port network. (b) The realization of the S_{21} measurement setup setup for a metamaterial transmission line resonator. The number of cells is N, the input end load impedance and the output load impedance are both Z_l for symmetric coupling and are marked in blue dashed boxes. The total impedance of the LHTL resonator looking from the left end is Z_{-N} and is marked in red dashed box. The source voltage is V_g. S_{21} represents the output voltage at port 2, V_2, relative to the input voltage at port 1, V_g.

through the TL resonator from the input to the output. When the load impedance is matched

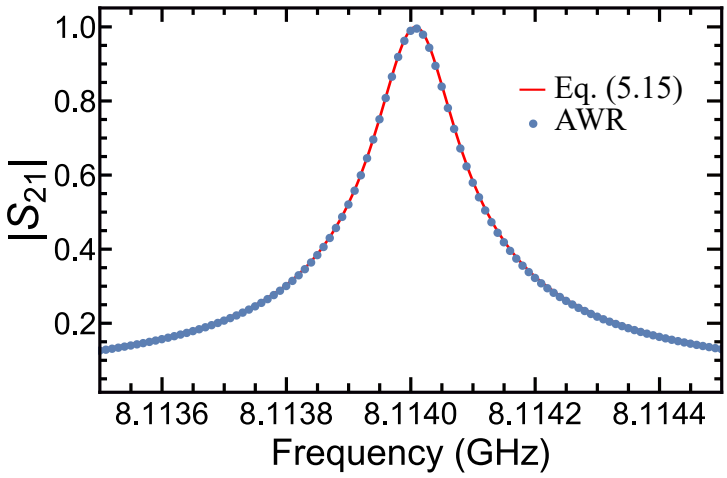

Figure 5.5: The plot of one mode of a 42-cell metamaterial resonator S_{21} calculated from numerical model Eq. (5.15) compared with AWR simulation. The unit cell parameters are: $C_L = 266$ fF, $L_L = 0.6$ nH, $C_R = 21.806$ fF and $L_R = 0.595$ nH. The values are picked based on the discussion in Sec. 8.2.2 and the Sonnet simulation result of the stray reactances that will be discussed in Chap. 8. The numerical result matches the simulation quite well.

to the source impedance at the input end, the S_{21} is simplified as [72]

$$S_{21} = \frac{b_2}{a_1} = \frac{V_2^-}{V_1^+}. \tag{5.10}$$

We can also express the input voltage V_1 in terms of the source voltage V_g: With perfect matching of the source impendance and the transmission line impedance, $Z_{-N} = Z_l$, we should have: $V_1 = V_g/2$, thus we have [90]

$$S_{21} = \frac{2V_2^-}{V_g^+}. \tag{5.11}$$

Fig. 5.4(b) shows a S_{21} measurement setup for a metamaterial transmission line with N unit cells. Once we can calculate the voltage V_2 across the load resistor, we can then calculate S_{21} for an LHRH resonator using Eq. (5.11). First, we calculate the voltage at the input end V_{in}:

$$V_{in} = V_g \frac{Z_{-N}}{Z_l + Z_{-N}}. \tag{5.12}$$

We can also recall from Eq. (5.7) that V_{in} should equal to $V_0^+ e^{j\beta N\Delta z} + \Gamma V_0^+ e^{-j\beta N\Delta z}$, from which we can solve for V_0^+:

$$V_0^+ = V_{in}/[e^{j\beta N\Delta z} + \Gamma V_0^+ e^{-j\beta N\Delta z}]. \tag{5.13}$$

The next step is to calculate the voltage at the output end, which, according to Eq. (5.2), should be $V_0^+(1+\Gamma)$. The voltage V_2 across the load R_0 is then given by:

$$V_2 = V_0^+(1+\Gamma)\frac{R_0}{Z_l}. \tag{5.14}$$

Combining Eqs. (5.12)-(5.14), we obtain an analytic expression for S_{21} for an LHRH resonator:

$$S_{21} = 2\frac{Z_{-N}}{Z_l + Z_{-N}}\frac{1+\Gamma}{[e^{j\beta N\Delta z} + \Gamma e^{-j\beta N\Delta z}]}\frac{R_0}{Z_l}. \tag{5.15}$$

Since β is a function of ω, or f for $f = \omega/2\pi$, Eq. (5.15) can be written as $S_{21}(f)$. Fig. 5.5 is the plot of Eq. (5.15) compared with AWR simulation of one mode showing quite good agreement. All other modes show comparable agreement between Eq. (5.15) and the AWR numerical simulations.

5.5 Resonator losses

Understanding loss mechanisms is a critical part of the design and characterization of any resonant structure. Resonator losses can be divided into two broad categories: interal and external or coupling losses [72]. In typical cQED structures, one of the dominant sources of internal loss is dielectric loss at the substrate-metal and substrate-air interfaces [91–93]. Through careful materials processing, this loss can be as low as 10^{-6} [90], although 10^{-5} is more typical. The coupling loss is determined by the external dissipation coupled to the resonator through the coupling capacitor. In Sec. 3.3, we have discussed the coupling loss for a conventional continuous TL resonator. For a practical superconducting metamaterial

resonator, we expect coupling losses to dominate at most of the frequency range that could be measured based on numerical simulation results. Thus, we will be mainly focusing on quantitative description of coupling losses for metamaterials here.

5.5.1 RHTL resonator coupling loss

First let's look at the coupling loss for a discrete for a RHTL resonator, since this actually has some key differences from a continuous RHTL resonator due to the different dispersion relations:

$$\omega_{TL} = \beta\sqrt{LC} \tag{5.16}$$

$$\omega_{RHTL} = \frac{2}{\sqrt{L_R C_R}} \sin\left(\frac{\beta\Delta z}{2}\right). \tag{5.17}$$

Based on Eq. (3.56), the coupling loss for a continuous TL resonator is given by:

$$\frac{1}{Q_c} = \frac{4\omega_n^2 R_0 Z_0 C_c^2}{n\pi}$$

where R_0 is the source impedance. With the linear dispersion characteristic of a continuous TL resonator, $\omega_n = n\omega_0$, the loss increases linearly with mode number n. In order to investigate the coupling quality factor of the discrete RHTL resonator, we have simulated S_{21} for a 40-cell discrete RHTL resonator in AWR with no internal loss. By fitting each resonance to a Lorentzian, we extract the resonance frequency f_0 and the full-width at half maximum (FWHM) Δf. The total Q is given by $Q = f_0/\Delta f$. Because the internal loss is set to be zero, this Q is just the coupling quality factor. In Fig. 5.6 we compare plots of the coupling loss for a continuous RHTL resonator computed with Eq. (3.56) and the simulated values for a discrete RHTL resonator from AWR.

Fig. 5.6 shows that the coupling loss for the discrete RHTL resonator matches that for the continuous case described by Eq. (3.56). However, starting around 5th mode, the coupling

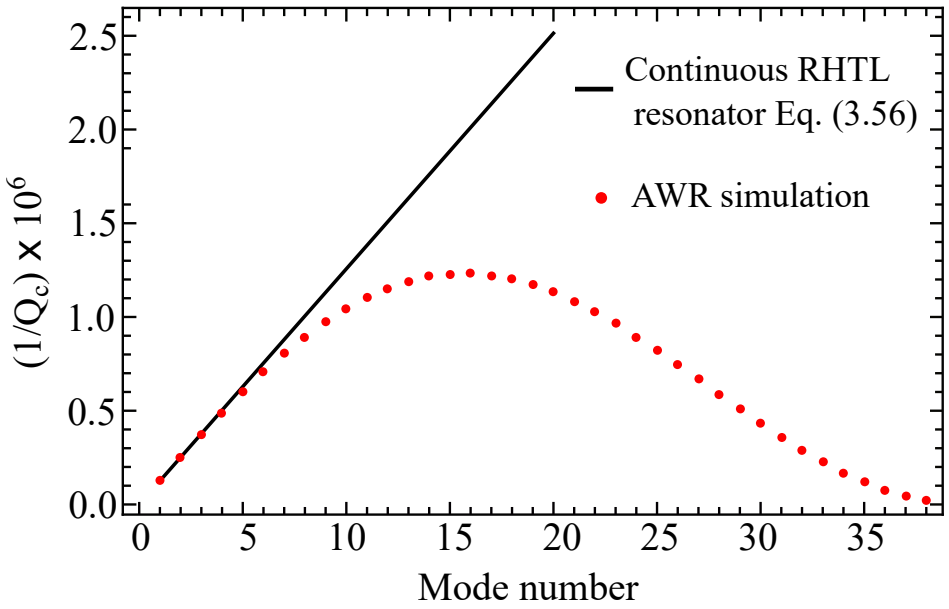

Figure 5.6: Solid line is $1/Q_c$ for a continuous RHTL resonator as described by Eq. (3.56). The plot should of course be discrete but we have plotted it as a straight line so it's more obvious how the Q_c would change with different mode number and how the discrete case is different from the continuous case. The red dots are the $1/Q_c$ values of different modes of a 40-cell RHTL resonator extracted from AWR simulation. The parameters are chosen so that the two cases have the same inductance and capacitance per length.

loss for the discrete RHTL resonator shows noticeable deviation from the linear dependence on mode number. The coupling loss reaches a maximum around the 15th mode before decreasing until the ultraviolet cutoff. In order to understand this surprising behavior, it is difficult to extend the treatment of coupling loss for a continuous RHTL resonator from Chap. 3 to the case of a discrete RHTL resonator. The method used there was to expand the impedance of a terminated lossy TL around the resonance frequency and compare its frequency dependence to that of an LCR resonator to map the TL resonator [Eq. (3.34)] to a parallel LCR circuit [Eq. (3.32)]. Then the Norton equivalent circuit was used to transform the capacitive coupling circuits to a parallel RC circuit [Eq. (3.50-3.51)]. The terminated impedance as Eq. (5.9) with $Z_L \to \infty$ of the discrete RHTL is a lossless expression, and it gives an infinite internal quality factor and the LCR mapping will fail. Even if the actual coupling of the resonator takes the form of $Z_L = 1/j\omega_n C_c + R_0$, which makes Eq. (5.9) no

longer lossless, it is still extremely difficult to expand Eq. (5.9) around ω_n

Instead of studying the discrete RHTL resonator in the impedance perspective, inspired by Ref. [75], we can treat it from the energy perspective. On resonance, with a certain input voltage V_{in}, we can derive the total stored electric energy in the capacitors and the stored magnetic energy in the inductors and compare that with the electric energy and magnetic energy in a LC circuit with the same input voltage. This in principle give us the effective capacitance $\tilde{C_R}$ and effective indutance $\tilde{L_R}$ for mapping the RHTL resonator to a loaded LC resonant circuit. Based on Eq. (3.56), we should have:

$$Q_c = \frac{\tilde{C_R}}{2\omega_n C_C^2 R_0}. \tag{5.18}$$

For an RHTL resonator, based on the resonance condition of $\beta\Delta z = n\pi/N$, we have:

$$\omega_n = \frac{2\sin\left(\frac{n\pi}{2N}\right)}{\sqrt{L_R C_R}} = \frac{2\sin\left(\frac{n\pi}{2N}\right)}{Z_0 C_R}. \tag{5.19}$$

Combining Eqs. (5.18) and (5.19), we have:

$$Q_{c,RHTL} = \frac{Z_0 C_R \tilde{C_R}}{4R_0 C_c^2 \sin\left(\frac{n\pi}{2N}\right)}. \tag{5.20}$$

Now we derive an expression for $Q_c(\tilde{C})$ for an RHTL resonator. The total electric energy stored in the capacitors of an RHTL resonator takes the form of:

$$E_{e,RHTL} = \frac{1}{2}\sum_{N=-m}^{-1} C_R |V_m|^2. \tag{5.21}$$

When C_c is small, we can take the limit of $Z_L = (1/j\omega_n C_c + R_0) \to \infty$. Thus, with Eqs. (4.7), (3.21) and (5.6), we have the voltage $V_{m,n}$ of mode n at each unit cell m to ground as:

$$V_{m,n} = V_0^+ \left(e^{-j\frac{mn\pi}{N}} + e^{j\frac{(m-1)n\pi}{N}}\right). \tag{5.22}$$

If we substitute Eq. (5.22) into Eq. (5.21), we obtain:

$$E_{e,RHTL} = C_R(V_0^+)^2 N. \tag{5.23}$$

At the same time, the electric energy stored in the equivalent LC resonator should be:

$$E_{e,LC} = \frac{1}{2}\tilde{C_R}|V_1|^2. \tag{5.24}$$

From Eq. (5.13), we have:

$$V_{1,n} = V_0^+ \left(e^{jn\pi} + e^{-\frac{jn\pi}{N}} e^{-jn\pi}\right). \tag{5.25}$$

So $|V_{1,n}|^2$ is:

$$|V_{1,n}|^2 = 4V_0^2 \cos^2\left(\frac{n\pi}{2N}\right), \tag{5.26}$$

which gives us the electric energy stored in the LC capacitor $\tilde{C_R}$:

$$E_{e,LC} = 2\tilde{C_R}V_0^2 \cos^2\left(\frac{n\pi}{2N}\right). \tag{5.27}$$

Equating Eqs. (5.23) and (5.27), we can obtain the equivalent LC circuit capacitance $\tilde{C}_R$ for a discrete RHTL resonator:

$$\tilde{C}_{R,n} = C_R \frac{N}{2\cos^2\left(\frac{n\pi}{2N}\right)}. \tag{5.28}$$

Plugging this result back into Eq. (5.20), we have the analytic expression of Q_c for a discrete RHTL resonator as:

$$Q_{c,RHTL,n} = \frac{C_R^2 Z_0 N}{8C_c^2 R_0 \sin\left(\frac{n\pi}{2N}\right)\cos^2\left(\frac{n\pi}{2N}\right)}. \tag{5.29}$$

If the RHTL has a characteristic impedance Z_0 that matches the source impedance R_0, the

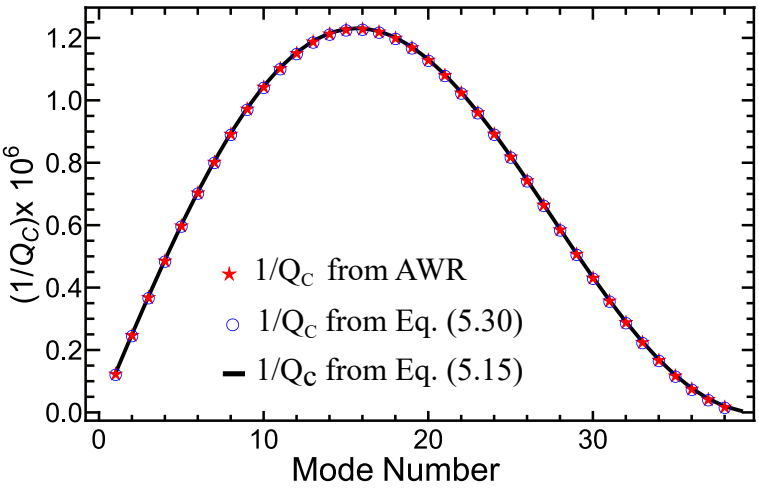

Figure 5.7: $1/Q_c$ comparison for an LHTL resonator between AWR simulations and the numerical calculation of both Eq. (5.15) and Eq. (5.29). The parameters for the RHTL are: $C = 250$ fF, $L = 0.625$ nH, $C_C = 1$ fF, $N = 40$.

coupling is then:

$$Q_{c,RHTL,n} = \frac{C_R^2 N}{8C_c^2 \sin\left(\frac{n\pi}{2N}\right)\cos^2\left(\frac{n\pi}{2N}\right)}. \tag{5.30}$$

In Fig. 5.7 we compare this expression with the simulated Q_c values for a discrete RHTL resonator from AWR and the two approaches agree quite well.

The effective inductance $\tilde{L}_R$ can be found from $1/\sqrt{\tilde{L}_R\tilde{C}_R} = \omega_n$ as:

$$\tilde{L}_{R,n} = \frac{L_R}{2N\tan^2\left(\frac{n\pi}{2N}\right)}. \tag{5.31}$$

5.5.2 LHTL resonator coupling loss

Now that we have developed an approach for treating the coupling loss for a discrete RHTL resonator, we will follow a similar treatment for an LHTL resonator. By studying the RHTL case, it's clear that the mapping of a discrete resonator to a LC circuit is still valid. Based on the derivation for an RHTL in Eqs. (5.20)-(5.23), with the LHTL dispersion relation:

$$\omega_n = \frac{1}{2\sqrt{L_L C_L}\sin\left(\frac{n\pi}{2N}\right)} = \frac{1}{2Z_0 C_L \sin\left(\frac{n\pi}{2N}\right)},$$

then the coupling quality factor will be given by:

$$Q_{c,LHTL,n} = \frac{Z_0 C_L \sin\left(\frac{n\pi}{2N}\right) \tilde{C}_L}{C_c^2 R_0}. \tag{5.32}$$

In order to calculate $\tilde{C}_L$, we again calculate the stored electric energy in the LHTL resonator on its nth resonance. Since all the capacitors are in series in an LHTL, while the cell voltage V_m is defined as the voltage to ground, voltage across the capacitor in cell m is $V_{m-1} - V_m$. Thus, we have:

$$E_{e,LHTL} = \frac{1}{2} \sum_{m=-N}^{-1} C_L |V_{m-1} - V_m|^2. \tag{5.33}$$

Based on Eq. (5.22), the result of the direct sum term is:

$$\sum_{m=-N}^{-1} C_L |V_{m-1} - V_m|^2 = 8N \sin^2\left(\frac{n\pi}{2N}\right). \tag{5.34}$$

Eq. (5.33) then becomes:

$$E_{e,LHTL} = 8NC_L (V_0^+)^2 \sin^2\left(\frac{n\pi}{2N}\right). \tag{5.35}$$

Equating this to the electric energy stored in the equivalent LC circuit given by Eq. (5.27) allows us to solve for $\tilde{C}_L$:

$$\tilde{C}_{L,n} = \frac{2N \sin^2\left(\frac{n\pi}{2N}\right)}{\cos^2\left(\frac{n\pi}{2N}\right)} C_L. \tag{5.36}$$

Upon substituting this expression for $\tilde{C}_L$ back into Eq. (5.32), we obtain:

$$Q_{c,LHTL,n} = \frac{2NZ_0 C_L^2 \sin^3\left(\frac{n\pi}{2N}\right)}{R_0 C_c^2 \cos^2\left(\frac{n\pi}{2N}\right)}. \tag{5.37}$$

Again, if the characteristic impedance Z_0 matches the source impedance R_0, the Q_c is just:

$$Q_{c,LHTL,n} = \frac{2NC_L^2 \sin^3\left(\frac{n\pi}{2N}\right)}{C_c^2 \cos^2\left(\frac{n\pi}{2N}\right)}. \tag{5.38}$$

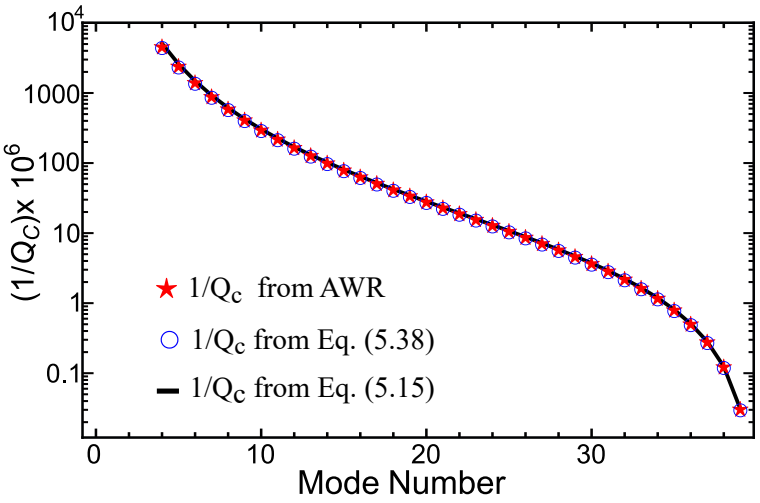

Figure 5.8: $1/Q_c$ comparison for an LHTL resonator between AWR simulations and the numerical calculation of both Eq. (5.15) and Eq. (5.38). The parameters for the LHTL are: $C_L = 250$ fF, $L_L = 0.625$ nH, $C_c = 10$ fF, $N = 40$. The first three small n modes are in extremely high frequency range and the peaks are too wide due to large loss, finding and fitting them are very difficult. Thus, they are not included here.

Eq. (5.38) indicates that the coupling Q is infinite if $n = N$, which makes $n = N$ mode undetectable and explains the reason for $n \neq N$. In Fig. 5.8 we show the $1/Q_c$ comparison for an LHTL resonator between an AWR simulation and the linewidth calculation based on the expression for S_{21} from Eq. (5.15), and Eq. (5.38). Again, as with the discrete RHTL resonator, all three approaches agree quite well. For completeness, the inductance $\tilde{L}_L$ for the effective LC circuit is given by:

$$\tilde{L}_{L,n} = \frac{2L_L \cos^2 \frac{n\pi}{2N}}{N}. \tag{5.39}$$

5.5.3 LHRH resonator coupling loss

As discussed previously, the actual metamaterial LHTL always has stray reactances associated with the lumped elements. Although the stray reactances typically generate only modest changes in the dispersion in the low frequency range, it is not clear in advance how much the stray reactances will affect the coupling loss. Analytically, the same method used in the last section for mapping the LHRH resonator to a LC circuit is still valid. For the

LHRH, it will have contributions to E_e from both $\frac{1}{2}\sum C_L|(V_{m-1}-V_m)|^2$ and $\frac{1}{2}\sum C_R|V_m|^2$. With Eq. (5.27), (5.23) and (5.35), the equivalent capacitance can be derived as:

$$\tilde{C}_{LR} = \frac{2NC_R + 8NC_L \sin^2\left(\frac{n\pi}{2N}\right)}{4\cos^2\left(\frac{n\pi}{2N}\right)}. \tag{5.40}$$

The expression for ω_n of LHRH resonator is quite complicated. By solving the dispersion relation of Eq. (4.10) with $\beta\Delta z = n\pi/N$, we get the resonance frequency as:

$$\omega_n = \sqrt{\frac{1}{2}\left(\frac{1}{C_R L_L} + \frac{1}{C_L L_R} + \frac{4\sin^2\left(\frac{n\pi}{2N}\right)}{C_R L_R} - \frac{\sqrt{-\frac{4C_R L_R}{C_L L_L} + \left(-\frac{C_R}{C_L} - \frac{L_R}{L_L} + 4\sin^2\left(\frac{n\pi}{2N}\right)\right)^2}}{C_R L_R}\right)}. \tag{5.41}$$

Plugging Eq. (5.40)-(5.41) back to Eq. (5.18) gives the expression of coupling quality factor of a LHRH resonator, but it is too long to be printed it here. Fig. 5.9(a) shows the numerically calculated coupling loss compared with the coupling loss extracted from calculated S_{21}. We can see that they agree to each other very well.

Although the expression for the coupling quality factor of an LHRH resonator becomes quite complex, Fig. 5.9(b) shows that the coupling loss for an LHRH only deviates from that for an ideal LHTL resonator for the lowest few modes, which occur at the highest frequencies. Thus, over much of the frequency range, the much simpler expression in Eq. (5.38) does a reasonable job, even for an LHRH resonator.

To conclude, in this chapter, I have discussed the physics of the LHTL resonators, including the dispersion relation, the transmission S_{21} calculation and coupling quality factor Q_c calculation. These calculations can also be extended to general discrete TL resonators like RHTLs and LHRH transmission lines.

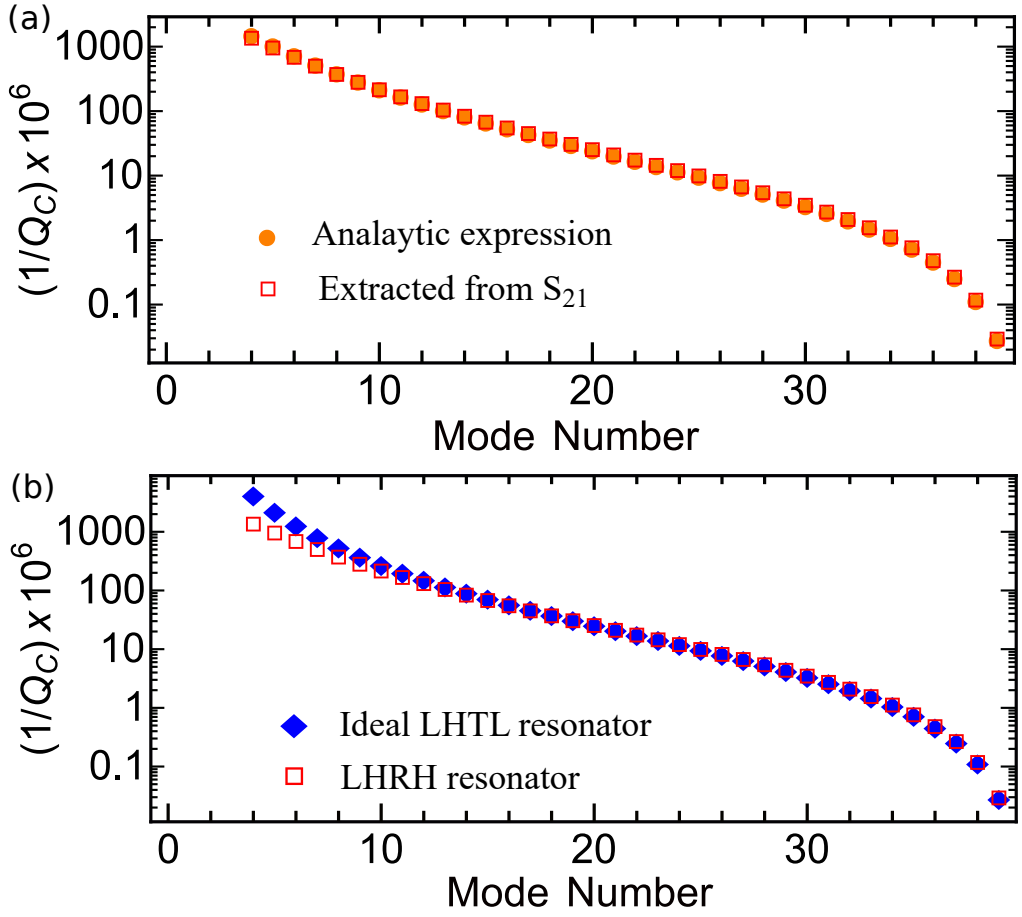

Figure 5.9: LHRH resonator coupling loss for different modes. (a) Comparison of the analytic approach derived from substituting Eq. (5.40)-(5.41) into Eq. (5.18) with the approach based on extracting the linewidths from $S_{21}(f)$ using Eq. (5.15). (b) Coupling loss comparison between a pure LHTL resonator and a LHRH resonator created by adding stray reactances using the approach based on the linewidth extraction from the corresponding S_{21} expressions. They are both extract from numerically calculated S_{21}. The parameters are: $C = 250$ fF, $L = 0.625$ nH, $C_c = 1$ fF, $N = 40$, $L_R = 0.033$ nH and $C_R = 16.21$ fF. For similar reasons to Fig. 5.8, the first three small n modes are not included here.

Chapter 6

Metamaterial resonator sample design

After the theoretical introduction in the previous chapters, we are now ready to design the actual circuit layout and parameters. Our goal is to realize a dense spectrum using a metamaterial resonator and eventually coupling a qubit to that spectrum. The first step is to successfully make a working metamaterial resonator.

There are several fundamental constraints and conditions that need to be taken into consideration. First, based on the dispersion relation of the LHTL (or LHRH line if we count the stray reactances, which are expected to be small) shown in Fig. 5.2, we need to pick a cut-off frequency. Because the flux-tunable transmon qubit that is commonly used in our lab typically has a upper sweet spot in between 5-9 GHz (that will be further discussed in Chap. 9), ω_{IR} should be below this range. Also, due to the limitation from the working frequency range of our High-electron-mobility transistor (HEMT) and room-temperature amplifiers, ω_{IR} should be above 2 GHz. Thus, aiming for a 5-7 GHz infrared cut-off frequency is ideal. Second, we need to consider the unit cell size. As discussed in Sec. 5.1, the number of resonances for the LHTL resonator is proportional to the total number of cells. So we hope to have as many cells as possible. Additionally, the sample holder that we are going to use has an opening window of 5×5 mm^2, which limits the size of our chip. Besides, we want to keep the characteristic impedance which is approximately

$\sqrt{L_L/C_L}$ to be 50 Ω.

6.1 Inductor design

Since metamaterial LHTL is basically repeated capacitors and inductors, let's first focus on the design of the inductor. An inductance of 0.625 nH and a capacitance of 250 fF are a good fit for our requirements: the cut-off is around 6.37 GHz which is in between 5 and 7 GHz, and the characteristic impedance is just 50 Ω. We also want to achieve this inductance in a small area in order to have more cells. Inspired by Ref. [47], we chose the meander-line inductor. The dimension and parameters are shown in Fig. 6.1.

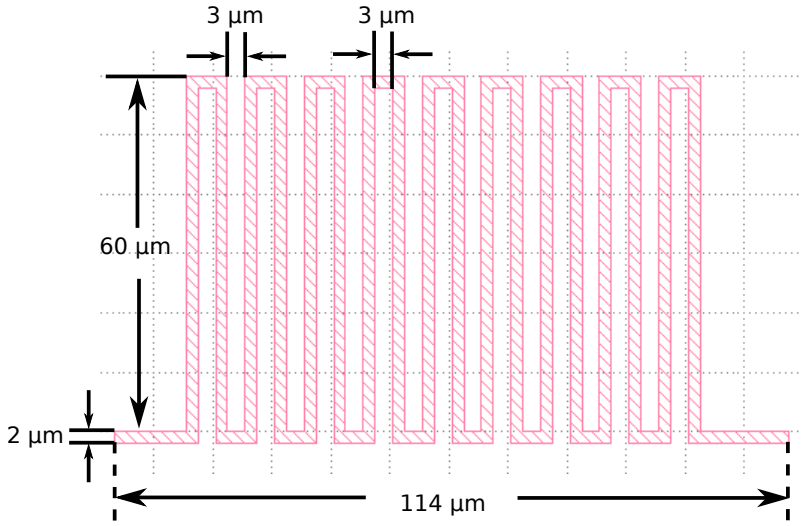

Figure 6.1: Inductor gds file rotated counter-clockwised by 90 degrees.

We simulated this geometry in Sonnet and the inductance of this design is around 0.6 nH which is very close to desired value. Sonnet also gives the self-resonance frequency of the meander-line geometry to be around 68 GHz which is much higher than the cQED frequency range. The meander-line shape is easy to fabricate and simulate, but it requires relatively large areas to provide a certain value of inductance [94]. Other candidates include spiral inductors and Josephson junctions [95]. The spiral inductor can provide large inductance in a relatively small area [96], but it requires a triple-layer fabrication process, which is

more complicated compared to a single-layer meander-line. The Josephson junction has a nonlinear inductance of

$$L_J = \frac{\Phi_0}{2\pi I_C \sqrt{1 - \left(\frac{I}{I_C}\right)^2}},$$

where I_C is the junction's critical current [97], which will be discussed in detail in Chap. 9. It also can provide a relatively large inductance. But the fabrication process is not easy to control, especially to control the variations between different cells. Also, the junctions need to be operated at low power otherwise the current can easily exceed the critical current at resonance frequencies. Thus, meander-line inductor design is selected.

6.2 Capacitor design

Similarly to the inductor, we hope to achieve the desired capacitance using the smallest possible area. We decided to use interdigitated capacitor. This kind of design is very commonly used in cQED and we have a lot of experience of adopting it to the circuit layout. Researchers have obtained very accurate expressions to estimate the capacitance [98]. The designed geometry is shown in Fig. 6.2. Based on Sonnet and Q3D [99] simulations, this geometry can provide around 250 fF of capacitance, very close to our target value. The self-resonance frequency given by Sonnet is about 52 GHz, which is also much higher than the cQED working frequency range and is below the self-resonance frequency of meader-line inductor.

Another very promising route is to use a parallel-plate capacitor design. It can provide larger capacitance per unit area than the interdigitated capacitor. However, it is a triple-layer process and the dielectric materials like SiO_x that are commonly used could be very lossy, which will limit the internal quality factor.

Be making the actual metamaterial resonator, we have designed and tested a series of lumped-element test oscillators fabricated using Al on Si with the same process and lumped-

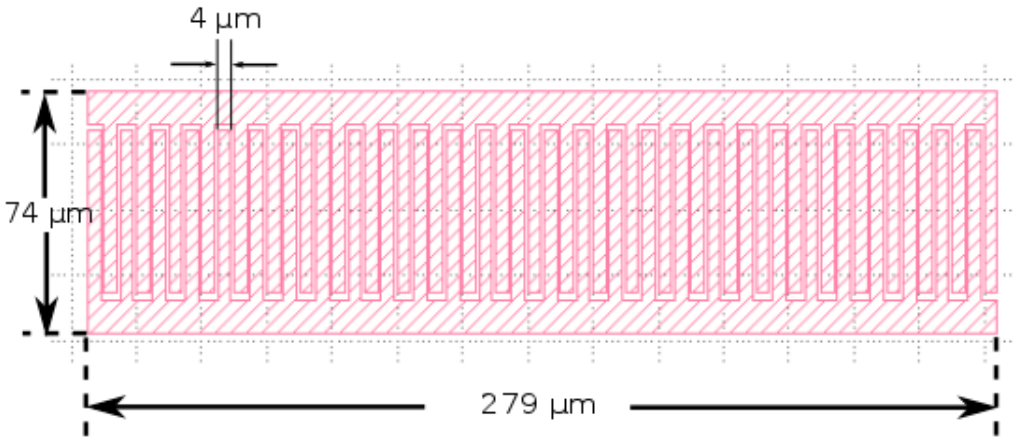

Figure 6.2: Capacitor gds file with dimensions

element parameters as in the design for metamaterials shown in Fig. 6.3(a,b). The test oscillator chip consists of four lumped-element LC oscillators, each one capacitively coupled to a CPW feedline. We were aiming for a lower ω_{IR} when the test oscillators were designed, so each one of them has a longer inductor than the meander-line in a unit cell of our metamaterial layout presented in this chapter, but the capacitor has the same interdigitated finger parameters as in the corresponding metamaterial line, although the capacitor is split in two halves that are arranged in parallel on either side of the inductor. The total number of finger pairs in the capacitor for oscillator number 1-4 is 29, 33, 37, or 41, respectively, thus allowing us to study the variation in capacitance for different numbers of fingers [2].

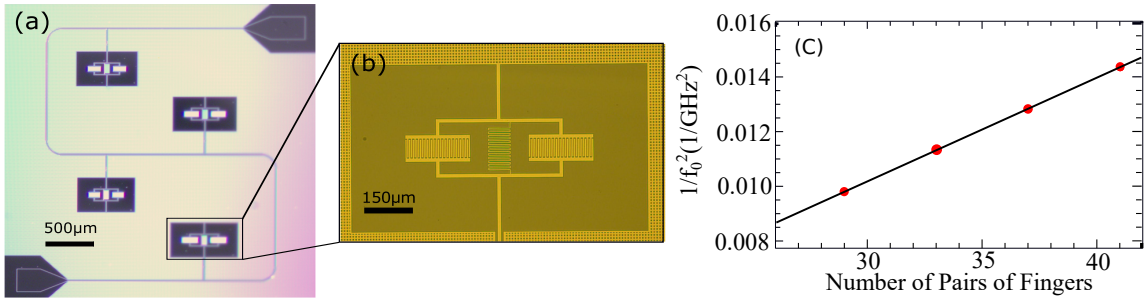

Figure 6.3: Optical micrographs of test oscillator chip as described in the text: (a) zoomed out; (b) close-up of single oscillator; (c) Plot of $1/f_0^2$ vs. number of finger pairs in capacitor of each test oscillator along with linear fit [2].

By studying the dip type resonances in S_{21}, we were able to extract the internal quality

factors and resonance frequencies for all four of them. The $1/Q_i$ is in the range of 10^{-5}, which is consistent with loss due to two-level systems at interfaces and surfaces in thin-film superconducting circuits at low temperatures [100, 101], which will also be discussed in Chap. 9. The linear fit of $1/f_0^2$ plotted in Fig. 6.3(c) indicates that the meander-line has an inductance of ∼0.7 nH if the capacitance per pair of fingers is 8.35 fF based on Q3D simulation and theoretical calculation based on Ref. [98], which is slightly higher than our Sonnet simulation discussed in Sec. 6.1. It could be because the capacitance estimation is slightly off, or the Sonnet does not include kinetic inductance, which could effectively lower the resonance frequency [2].

6.3 Metamaterial configuration and layout

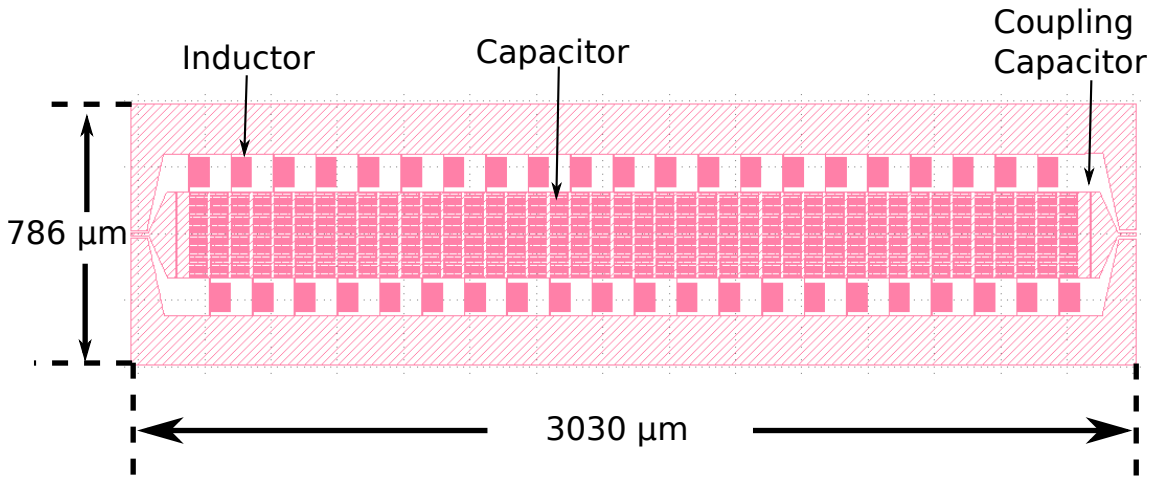

Figure 6.4: LHL gds file with dimensions

Since our meander line inductor has a large horizontal length, if we place them all on one side respect to the capacitors, they will need more space than the capacitor width to avoid overlapping. Even if we make sure they are not touching each other, they still could have strong cross-talk effect that the mutual inductance between the meander lines arises which will change our mematmaterial's transmission property. So, we decide to use a

"staggered" configuration shown in Fig. 6.4 with the neighboring cells having the inductors pointing to the opposite directions. In other words, the odd number of cells would have the inductors connecting to the bottom ground plane while the even number of cells have the inductors connecting to the top ground plane. In this way, the space between inductors is at a maximum. This design is expected to have better symmetry than placing all the inductors on one side. We decided to use a gap-capacitor design as the coupling capacitor, as shown in Fig. 6.4. We should be able to minimize the distance between the coupling capacitor and the LHTL to avoid any unwanted parasitic resonance mode. Besides, the gap width is very easy to control during the fabrication. For the 2 μm gap, it should have the capacitance of roughly 30 fF based on Q3D simulation. Based on Eq. 5.38, the coupling quality factor Q_c for the mode around 7 GHz should be about 10^5, which is close to our internal quality factor discussed in Sec. 5.5 estimation; thus, it should be able to reach the critical coupling range. With all these designs combined together, the chip layout is shown in Fig. 6.5. The total number of cells we can fit in an active area of 4×4 mm^2 is 42.

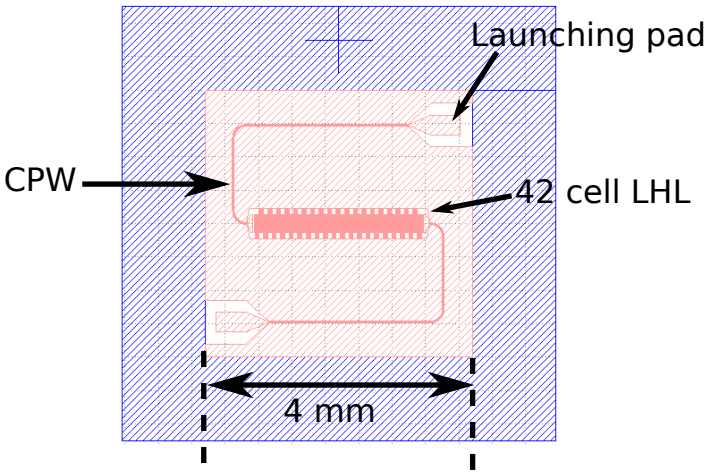

Figure 6.5: Metamaterial resonator chip layout with dimensions.

Chapter 7

Measurement of metamaterial resonators

In this chapter, I will cover the microwave measurements of the metamaterial resonances, the measurement setup, and imaging experiments to visualize the microwave modes structure. The fabrication process of the metamaterial resonator will be described in detail in Chapter 10.

7.1 Experimental setup for microwave measurements

Once our 42-cell metamaterial resonator has been fabricated, it is loaded into a printed circuit board (PCB) with the dimension discussed in Chap. 6 as shown in Fig. 7.1. The launching pads are connected using aluminum wire-bonds to the center traces of the board which then connects to the outside through SubMiniature version A (SMA) connectors. The ground plane of the sample is connected with the PCB ground plane through numerous wire-bonds in order to maintain a low impedance microwave ground around the entire perimeter of the chip. Some jumper wires are also used to keep the sample ground plane equipotential. The wire-bonds are made of aluminum with 1% silicon with diameter of 32 μm. An aluminum cover is used to protect the sample from unwanted black body radiation and magnetic fields.

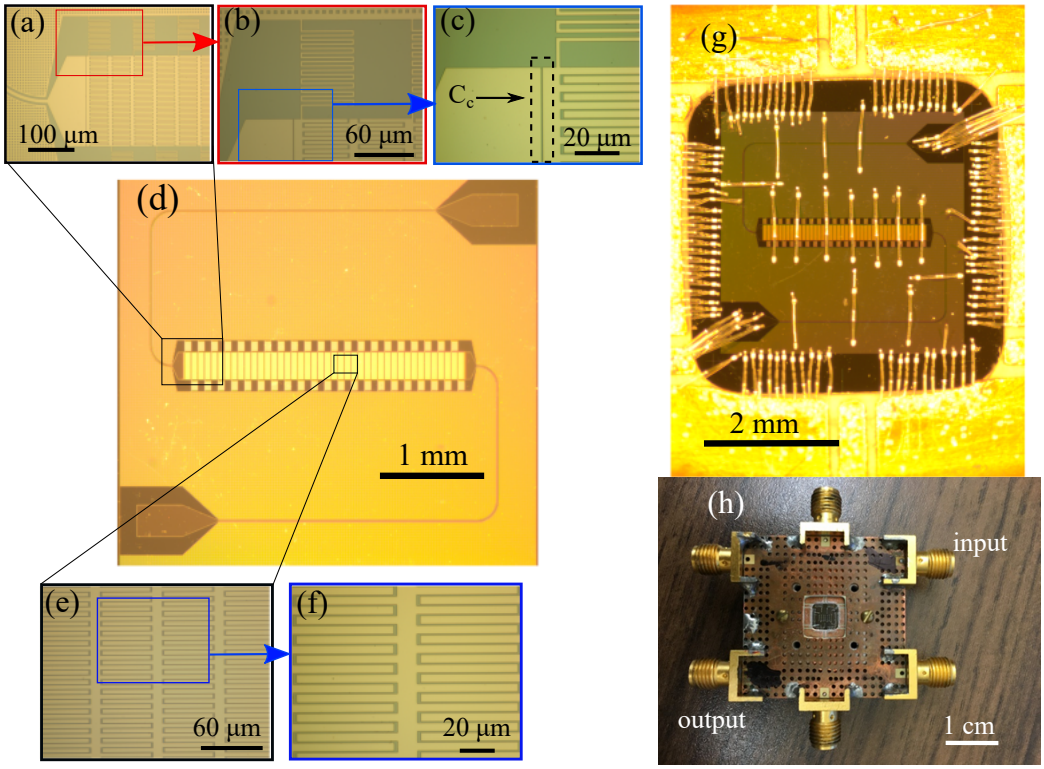

Figure 7.1: Optical micrograph images of a chip identical to the metamaterial sample used for measurement: (a) close-up image of input gap capacitor C_c and the first few cells; (b) meander-line inductor of the first cell; (c) detail of input gap capacitor and connection between inductor and capacitor of first unit cell; (d) zoomed-out image of entire chip; (e) zoomed-in image of inter-digitated capacitors; (f) detail of fingers and gaps in inter-digitated capacitors; (g) zoomed-out image of the chip fitting in the sample holder and the wire bonds; (h) the entire sample holder with chip bonded in place and input/output connections marked.

The sample is then mounted on the cold finger of our Adiabatic Demagnetization Refrigerator (ADR) from High Precision Devices. Our ADR has 4 different temperature stages: 60 K stage, 3 K stage, 700 mK stage and the cold finger which can cool to a base temperature of 50 mK. The 60 K and 3 K stages use a Pulse Tube Refrigerator to keep the temperature stable at these levels. A superconducting magnet which is placed on the 3 K stage will create a magnetic field up to 4 T when operated using a current of 9 A. Two paramagnetic salt pills, one made of Gadolinium Gallium Garnet (GGG) is on the 700 mK stage, and one made of Ferric Ammonium Alum (FAA) on the 50 mK stage, can be polarized by ramping the magnet to full field and soaking for roughly one hour. This ensures the magnetization

of the salt pills are as close to maximum as possible so the entropy of the salt pills is at the minimum. The salt pills are thermally connected to the 3 K stage through a heat switch that is kept closed during the soaking in order to stabilize the temperature of the salt pills to 3 K. After soaking for one or two hours, the heat switch is then opened so that the salt pills are thermally isolated from the rest of the system so that no heat can flow in or out of the salt pills or cold finger. Then the magnetic field is slowly reduced by reducing the DC current. The salt pills are magnetized after the soaking step. As the magnetic field is reduced, the interaction energy between the spins and the magnetic field decreases, but since no heat can flow in or out of the salt pills, the temperature must decrease [102]. As a result of this process, the GGG stage cools to 700 mK and the FAA stage reaches 50 mK Ideally, this process is reversible: ramping up the magnetic field again increases the interaction energy between the spins and the magnetic field, which must raise the temperature. This provides an effective way of controlling the temperature to stay at a value between the base temperature and 3 K.

We use a Vector Network Analyzer (VNA, model N523A, 300 kHz-20 GHz) to perform the microwave transmission $S_{21}(f)$ measurement discussed in Sec. 5.4. It provides an input AC voltage through port 1 with impedance of 50 Ω and measures the complex ratio of the output voltage on port 2 of 50 Ω load impedance to the input voltage. The microwave signal sent from the port 1 of VNA is transmitted through a transmission line to the top of ADR and down to the input end of the metamaterial passing through 39 dB of cold attenuation for thermalization. The measurement setup schematic is shown in Fig. 7.2. The signal then passes through the metamaterial resonator and then goes back to the port 2 of VNA amplified by a HEMT mounted on the 3 K plate of the ADR and again with a room-temperature amplifier (NARDA West) with 35 dB gain. For magnetic shielding, a cryogenic mu-metal can mounted on the 3 K plate is placed to surround the sample. In order to characterize the transmission baseline, a separate measurement of full transmission is performed. We load a sample with a CPW type of feedline in the same type of sample

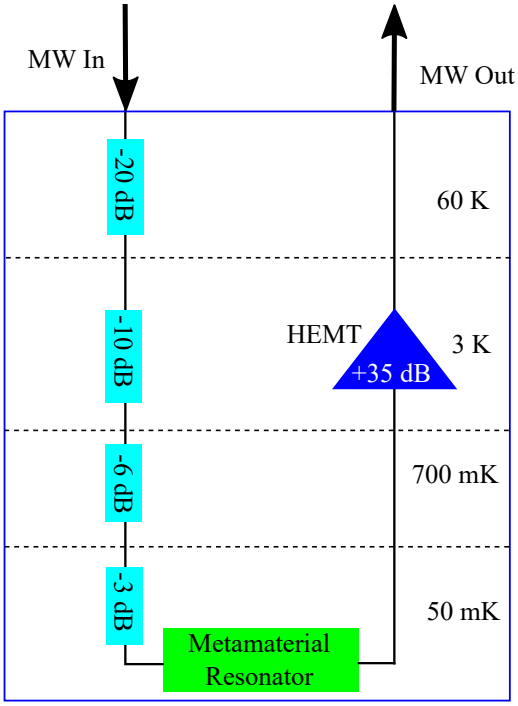

Figure 7.2: Microwave measurement setup inside ADR with attenuation/amplification specified on each temperature stage.

holder and connect it in the same way as our metamaterial sample and cool it down to the same temperature to measure the $S_{21}(f)$. Ideally, this could give us a full transmission which can serve as a baseline to our metamaterial measurement although there are always small chip to chip differences which can introduce small variations in the baseline transmission.

7.2 $S_{21}(f)$ measurement result

In this section, we present measurements for one of our metamaterial resonators at two different temperatures: 65 mK and 3 K with input power of ~ -90 dBm applied on the input end of the sample. Fig. 7.3 is the calibrated measurement results: black solid line is the base temperature while the blue dashed line is the high temperature result. It can be found that the spectrum exhibits numerous sharp modes that generally get further apart for higher frequencies, except for the lowest few modes where the spacing is somewhat larger.

The infrared cut-off of our metamaterial resonator occurs at 4.245 GHz. The measured

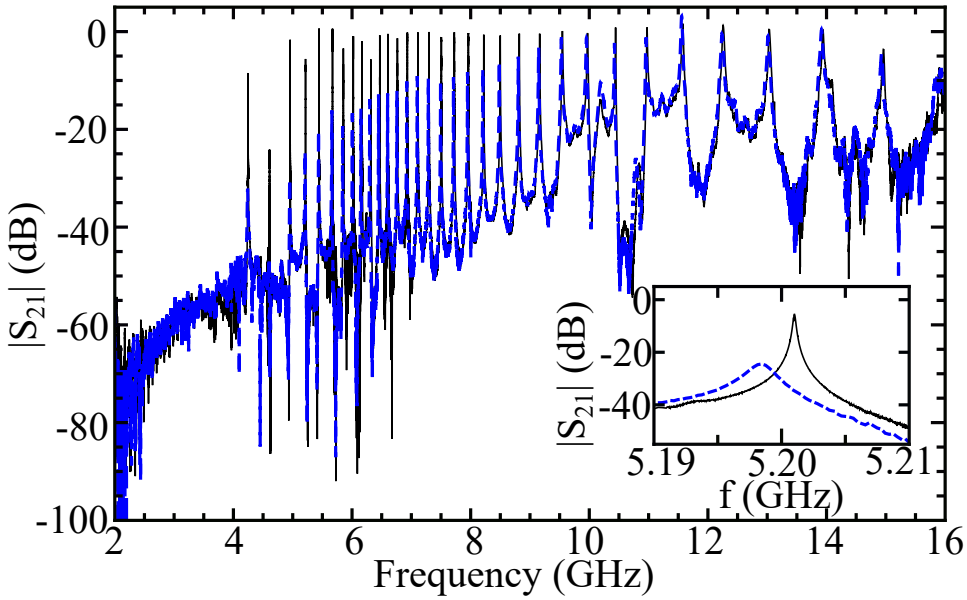

Figure 7.3: Measurements of the magnitude of the microwave transmission $|S_{21}(f)|$ on the ADR at two different temperatures: 65 mK (black solid line); 3 K (blue dashed line). Inset: zoomed-in plot in the vicinity of $n = 38$ mode near 5.20 GHz.

smallest mode spacing is 147 MHz, which is between mode 33 and mode 32, while according to Eq. (5.41), the smallest mode-spacing should be around 14 MHz between mode 39 and 38. After mode 32, the mode spacing increases as the frequency increases, which agrees with theory prediction as shown in Fig. 5.2. Due to the limitation of our HEMT bandwidth which is roughly 2-16 GHz, the highest frequency resonance we can measure is roughly 15 GHz, which corresponds to the 9th mode. The highest Q we measured at base temperature is around 26,000. I'll discuss the quality factor in detail in Sec. 7.3. From the two different curves at different temperatures, it's clear that quality factors and the resonance frequencies both depend on temperature. Due to an increased population of thermal quasiparticles which brings higher internal loss, Q is lower at higher temperature which is far away from the T_c of Nb at 9.26 K [103]. Also, due to higher kinetic inductance at higher temperature, the resonance frequency will shift down [104], which is reflected clearly in the inset of Fig. 7.3. Understanding the temperature dependence of the modes' frequency response will be important for interpreting the LSM imaging results presented in section 7.5.2.

7.3 Quality factor

Once $S_{21}(f)$ is measured, we can fit the resonance trajectory in the complex plane using a standard function described in numerous papers on superconducting resonators, including [91]

$$S_{21}(f) = \frac{Q}{Q_c} \frac{e^{j\phi}}{1 + 2jQ(f - f_0)/f_0}, \tag{7.1}$$

where Q, Q_c and ϕ are the total quality factor, the coupling quality factor and the rotation of resonance circle on complex plane respectively. The internal quality factor Q_i can be separated by using the relation in Eq. 3.57 of

$$\frac{1}{Q} = \frac{1}{Q_c} + \frac{1}{Q_i},$$

as discussed in Sec. 3.3. This method works very well for absorption type of resonance, for which the transmisson is always full away from the resonance and only shows a Lorentzian dip at the resonance frequency, thus allowing for the baseline to be self-calibrated [105]. However, for a transmission measurement that yields a peak on resonance, extracting the internal and external quality factors requires a separate calibration of the baseline transmission through the system, so that a measurement of $|S_{21}| = 1$ corresponds to full transmission. The accuracy of the fit then depends crucially on the quality of the baseline subtraction. As introduced in Section 7.2, the baseline was taken in a separate measurement. This technique was used and the result was tested multiple times in our lab so that the variation in the transmission levels between different baseline measurements is in the range of ± 2 dB. It turns out that since the quality factor of a LHTL resonance decreases quickly as the frequency goes up, many of our modes are in a over-coupled regime with $Q_c \ll Q_i$, so the total Q is dominated by the coupling Q. In this situation, it's difficult to extract Q_i accurately. Also, a small change in the baseline will result in a big change in the internal loss fit rather than the coupling loss. Here, we focus on the fitting for the coupling loss first. In order to counter the baseline inaccuracy, we manually add an offset of ± 2 dB to the baseline. On the other

hand, for a passive device, such as these LHTL resonances, $|S_{21}|$ should never exceed unity. Thus, if a certain resonance is higher than 0 dB after counting the offset, we only shift it up to -0.01 dB.

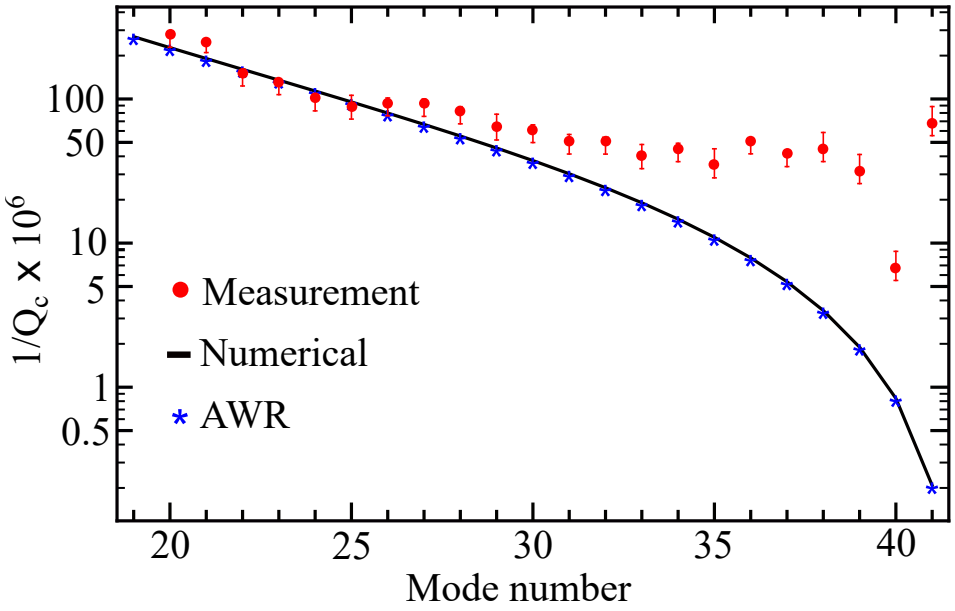

Figure 7.4: The external loss plot in log scale of the measurement result compared with AWR simulation and theoretical dependence calculated from Eq. (5.15) with parameters of $L_L = 0.625$ nH, $C_L = 250$ fF, $L_R = 59.5$ pH and $C_R = 21.8$ fF.

Fig. 7.4 is the comparison of the coupling loss between the measurement data, AWR simulation data with no internal loss, and the numerical calculation of the Q extracted from the FWHM of S_{21} by Eq. (5.15). We can see that the numerical result agrees very well with the AWR simulation, which is what we expected. However, the measurement data has higher coupling loss than the numerical calculation at low frequency and high mode number. At high frequency, it falls close to the numerical curve. Figure 7.5 is the comparison between the extracted $1/Q_i$ and $1/Q_c$ from the measured S_{21} data. It can be seen that for most modes, the metamaterial resonator is in the over-coupled regime where $Q_c \ll Q_i$, so extracting accurate Q_i values from the fit $S_{21}(f)$ fits is difficult. Overall, the internal loss is around 5×10^{-6}, which is consistent with previous experiments of superconducting resonator on Si substrate, where the loss is dominated by dielectric loss at the substrate surface and interfaces with the

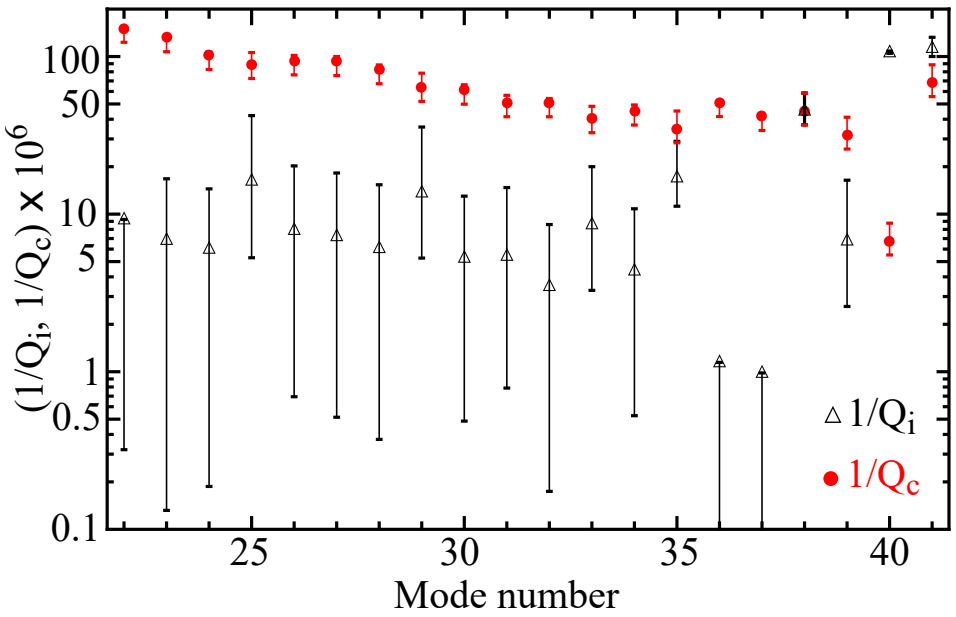

Figure 7.5: Comparison of internal loss and coupling loss extracted from the measured $S_{21}(f)$.

metal traces [100, 101]. The large error bars on the $1/Q_i$ points indicate that modest changes in the baseline level have a significant impact on the extracted $1/Q_i$ levels. We note that the first two low frequency modes have anomalously high internal loss, which is consistent with results on other metamaterial resonators that we measured, including Al samples. We are still investigating the source of this excessive internal loss on the lowest frequency modes. It may perhaps be related to grounding issues or the staggered inductor geometry which may especially impact these shortest wavelength modes.

7.4 Temperature-dependence and power-dependence measurements

Besides the measurements of metamaterials fabricated with Nb films, we have also made similar devices using Al thin films and performed similar microwave transmission measurements [2] and Fig. 7.6 shows the measured transmission of one of them. The spectrum is similar to the Nb metamaterial described in Sec. 7.2. However, due to the lower T_c of Al

compared to Nb, when we measured the sample at different temperature or power, there were significant differences that will be addressed here.

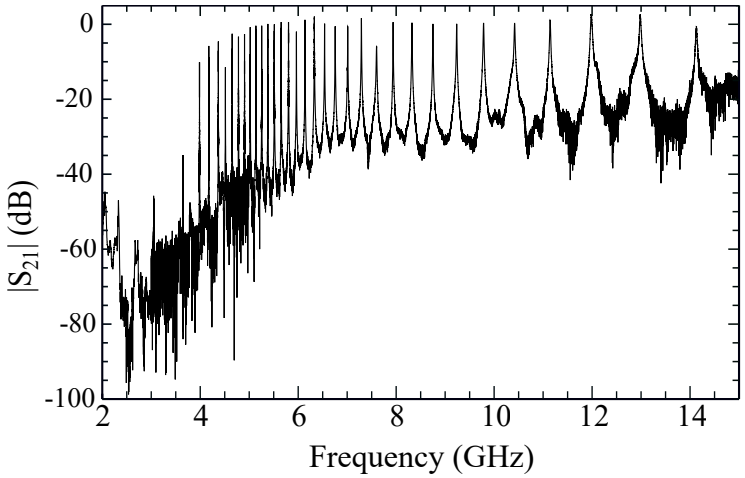

Figure 7.6: Measured $S_{21}(f)$ of a Al metamaterial resonator from Fig. 4(a) in Ref. [2] with inset removed.

We measured the Al metamaterial chip on the ADR and adjusted the temperature by tuning the ADR magnetic field. As discussed in Section 7.1, when operating in the adiabatic regime with the ADR heat switch opened, starting from 3 K with maximum magnetic field strength, the ADR can cool down to base temperature if fully demagnetized. This process is reversible: if the magnetic field is increased, the temperature will also increase. Thus, we can control the temperature in the range between 50 mK to 3 K by adjusting the magnetic field. Since the T_c of Al is $\sim$1.2 K which is below 3 K, we are able to measure the chip at a temperature close to T_c and expect to see the resonance shift to lower frequency due to higher kinetic inductance [42] and quality factor drop due to higher loss associated with increased number of quasiparticles. The results for one of the modes are shown in Fig. 7.7. At the base temperature of 50 mK, the peak is sharp and the transmission is high. As the temperature rises, the peak almost has no change in transmission or frequency at 120 mK-220 mK, and then starts to shift to lower frequency where it becomes broader and lower, just as we expected. The T_c of Nb is much higher than 3 K, thus the shift in frequency and Q in the same temperature range is much less obvious.

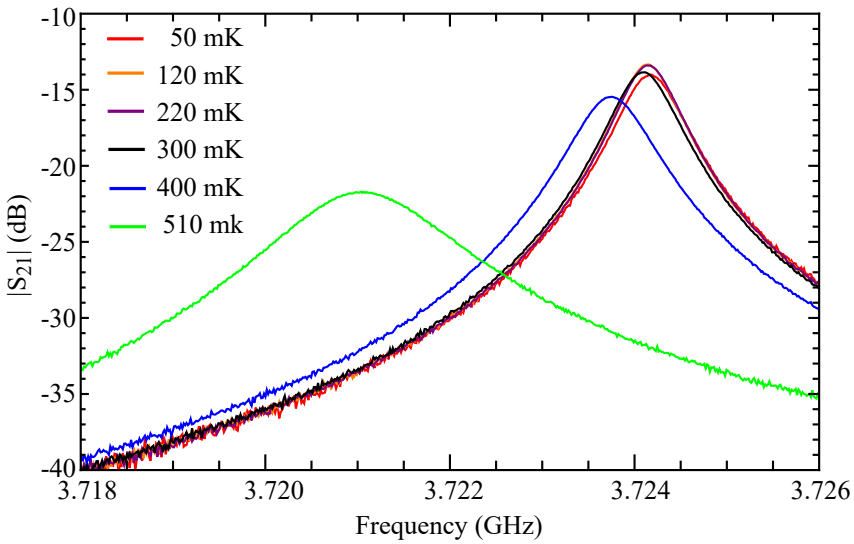

Figure 7.7: One of the Al metamaterial resonator modes at 3.724 GHz measured at different temperature on ADR.

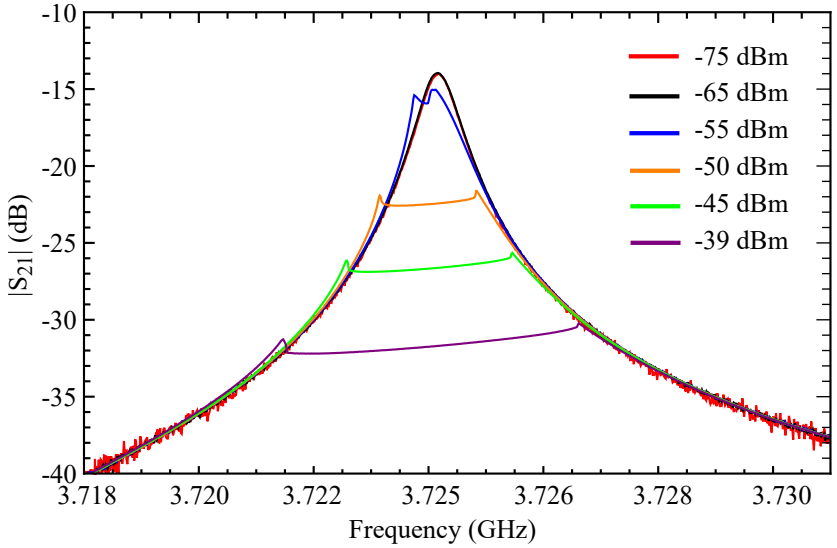

Figure 7.8: One of the Al metamaterial resonator modes at 3.724 GHz measured at different input power on ADR.

We also measured the transmission at different input power on the metamaterial and the results for the same mode in Fig. 7.7 are shown in Fig. 7.8. At relatively low power, the peak is well defined. As the power increases, the peak starts to show some nonlinearity where it is no longer a Lorentzian shape and the transmission is suppressed. This can be interpreted by the current on resonance exceeding the critical current of some of the meander-line inductors, which makes them no longer superconducting. Thus, the loss will increase and the transmission near the resonance frequency is lowered. For the same type of thin-film meander-line geometry, Nb has a larger critical current, which makes the power-dependent effect on the resonance much weaker than in the Al sample.

7.5 Laser Scanning Microscopy imaging

In addition to microwave measurement of S_{21} at low temperature, a low-temperature Laser Scanning Microscopy (LSM) imaging experiment of our sample was done by Alexander Zhuravel and Alexey Ustinov at the Karlsruhe Institute of Technology. The LSM is a technique that has been used previously to image the microwave current distributions in a wide variety of superconducting structures under rf excitation [106, 107]. The various modes of LSM operation have been described in detail in Refs. [108, 109].

Here I am going to briefly discuss the basic principle of the operation of the LSM. The LSM uses a localized energy deposition instrument that deposits a portion of energy into a superconducting sample locally as a perturbation and then measures some global response of the sample, like $S_{21}(f)$, to that energy at that particular location. A focused beam of a diode laser is used as the energy source. It acts on the surface of the planar objects, including superconducting microwave devices, to form a non-contact light (and/or thermal) probe for 2D rf and optical characterization. The laser beam raster scans the surface of the sample while the beam intensity is modulated at a low frequency. By using a lock-in technique, an image of the photoresponse $PR(x, y, f)$ can be produced by correlating the output signal

with the location of the laser spot.

7.5.1 LSM imaging result

In the metamaterial resonator measurement, the chip was mounted inside a vacuum cavity of a cryostat with optical access which stabilizes the temperature of the sample. Although the temperature ideally could be controlled in the range of $2.5 - 30$ K with an accuracy of 1 mK by using a resistive heater bifilarly coiled around a copper cold stage, it is much higher than the T_c of Al which is a metal commonly used in cQED. This is one of the reasons why we use Nb instead of Al in the fabrication process. The temperature of the chip was $\sim$5 K during the imaging of our metamaterial resonator. The laser with wavelength of 640 nm was focused to a spot of 12 μm diameter on the sample with a power of $\sim$ 10 μW at the sample, resulting in a local temperature modulation on the sample at the location of the laser spot of no more than a few mK. The laser intensity was modulated at 100 kHz while the microwave transmission $S_{21}(f)$ was measured with semi-rigid cryogenic coaxial cables carrying microwave signals to and from the sample. The maximum frequency accessible on the LSM was 20 GHz, similar to the limitation of the measurement electronics on our ADR.

LSM imaging provides us a way of looking at the standing wave patterns of our metamaterial transmission line resonators. Figure 7.9(a) contains an image of the metamaterial in the LSM, with an arrow indicating the orientation of 1D scans that were measured in the LSM. As the frequency was varied, the average PR signal exhibited sharp peaks, shown in Fig. 7.9(b), which precisely line up with the microwave transmission resonances in $|S_{21}(f)|$ that were measured simultaneously and shown in Fig. 7.9(c). In Fig. 7.9(d), the density plot of $PR(x, y_0, f)$, where y_0 indicates the location of the linescan on the chip, again shows the sharp features at the resonant frequencies, but also exhibits fine structure along the scan direction. Thus, it is clear that the LSM imaging of the device can be used to investigate resonances in the metamaterial and their corresponding standing-wave patterns.

We then performed 2D scans of $PR(x, y, f_n)$ while exciting one of the metamaterial

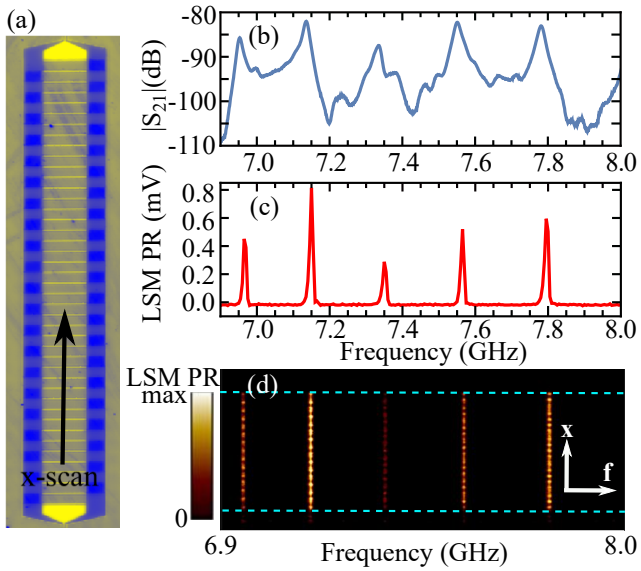

Figure 7.9: (Color online) (a) LSM reflectivity image with arrow indicating direction of 1D linescans. (b) Microwave transmission $|S_{21}(f)|$ measured on LSM. (c) Average LSM photoresponse $\overline{PR}(y_0, f)$ along 1D linescans. (d) 1D linescans $PR(x, y_0, f)$ vs. frequency; dashed lines indicate location of input/output coupling capacitors.

modes, in this case the $n = 40$ mode at 3.34 GHz, which is the next-to-lowest resonant frequency in the device [Fig. 7.10(b)]. The LSM image exhibits a clear standing wave pattern with two antinodes along the length of the transmission line. We have performed numerical electromagnetic simulations of our metamaterial layout using Sonnet, as will be described in detail in Sec. 8.2. Figures 7.10(c, d) contain plots of the simulated charge density and current density in the metamaterial, also excited on the $n = 40$ mode. Fig. 7.10(b) shows the a 2D image of the LSM photoresponse when the $n = 40$ mode of the metamaterial is excited. In the Fig. 7.10(b) for the capacitors in the LHTL near an antinode, we observe that the photoresponse is highest at the edges of the capacitor where the inductors are connected. This effect can be attributed to the enhanced reflectivity of the laser signal from the regions covered with Nb compared with the bare Si regions beyond the capacitor edge. When the laser spot straddles the edge of the capacitor and the bare Si beyond, the excess absorbed energy in the Si enhances the photoresponse signal.

When the LSM imaging is applied to superconducting structures, a bolometric response

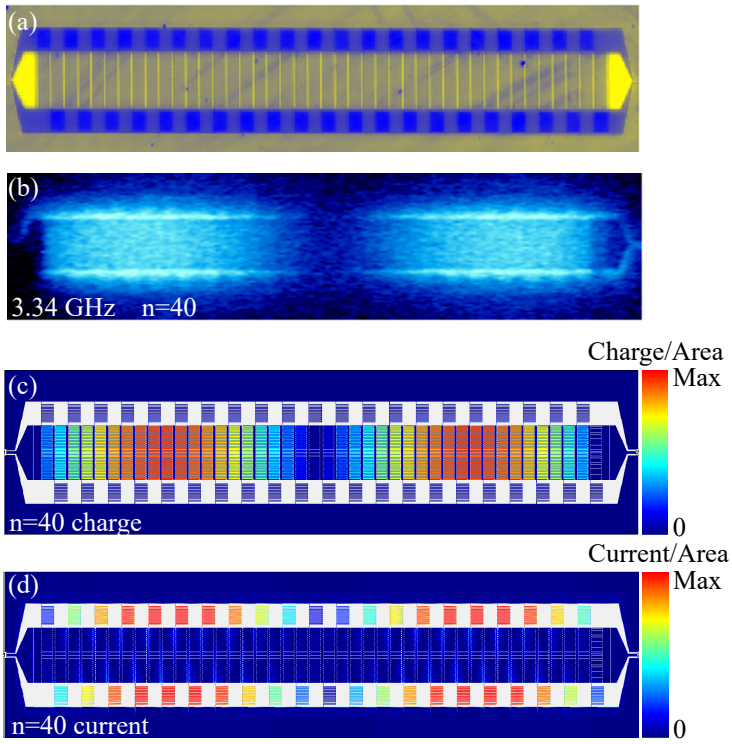

Figure 7.10: (Color online) LSM photoresponse compared with Sonnet current/charge density simulation: (a) the reflectivity map showing details of the metamaterial design in the scanned area; (b) 2D distribution of microwave photoresponse $PR(x, y, f_{40})$ that illustrates standing wave pattern of RF current density distribution in $n = 40$ mode at frequency of 3.34 GHz; (c) Sonnet charge density simulation of $n = 40$ mode; (d) Sonnet current density simulation of $n = 40$ mode.

will be produced by the interaction of the laser spot with the superconductor. Due to local heating of the superconductor by the absorbed laser probe, this response has both inductive and resistive components. In addition, a non-thermal response due to the generation of nonequilibrium quasiparticles in the superconductor from the deposited pair-breaking laser energy can be caused. All three types of photoresponse signals are proportional to the square of the local microwave current density in the superconductor, $J_{MW}(x, y)$ [110]. In our LSM imaging experiments on the LHTLs, we have observed a significant photoresponse in the vicinity of the meander-lines near the current antinodes in the standing wave patterns which is precisely in regions where we expect large microwave currents will occur. The frequency-dependence of the PR on our LHTLs [Fig. 7.10(b)] and correlated $|S_{21}(f)|$ [Fig. 7.10(c)] is

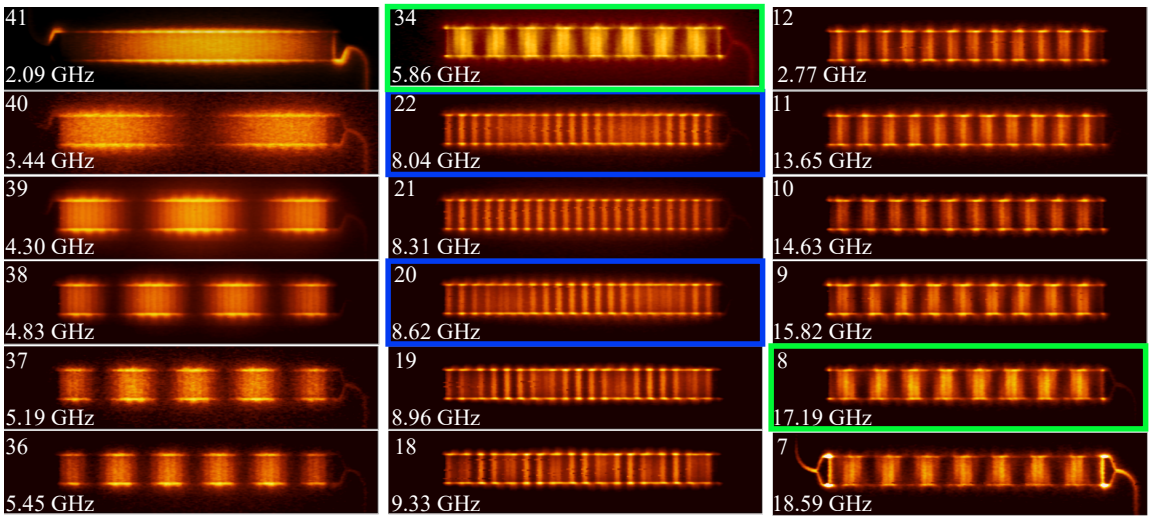

Figure 7.11: (Color online) Array of LSM images of metamaterial for different modes, labeled by mode number and frequency. The under-sampling effect is very clear for the images of low frequency modes in the left column where wavelength should be short but appear to be long. The green boxes are the pair of $n = 34$ and $n = 8$ modes where they both have 8 anti-nodes. The blue boxes are the pair of $n = 22$ and $n = 20$ modes where they both have 22 anti-nodes.

most consistent with the non-thermal LSM response mechanism [107]. However, an even larger photoresponse was observed in regions where we expect large microwave voltages, around the capacitors near the standing-wave antinodes for the charge density. We suspect this to be caused by an enhanced loss in the capacitors that can be explained by photo-induced carriers in the Si substrate in between capacitor fingers. This mechanism results in the largest PR in regions with large microwave electric fields. We are not aware of reports of prior LSM imaging experiments on superconducting interdigitated capacitors on Si. Thus, the nature of our sample layout and substrate material provide us with a photoresponse image of both the microwave current and charge density distributions in our LHTLs.

We have repeated the LSM imaging for all of the modes in our metamaterial below 20 GHz and many of them are presented in an array shown in Fig. 7.11. The various features in these images will be discussed in the section 7.5.2.

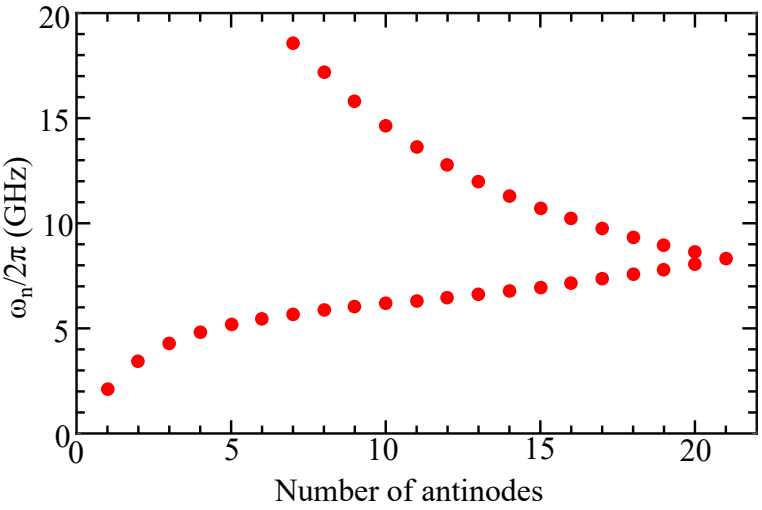

Figure 7.12: Plot of mode frequency vs. number of antinodes from the corresponding LSM images.

7.5.2 LSM imaging analysis

From the LSM images of the metamaterial resonator for the high-frequency modes, we observe a stepwise change in the number of antinodes in the standing-wave pattern as we move between modes. For all of the modes that we can image above mode 21, it is clear that the wavenumber is decreasing with increasing frequency, consistent with the left-handed dispersion relation from Eq. (4.42). However, for the lower frequency modes, from mode 41 to 21, the images show a standing-wave pattern with an increasing number of antinodes for increasing mode frequency. Fig. 7.12 is the plot of mode frequency vs. number of antinodes in the corresponding LSM image. From this plot, we observe that each low-frequency mode has a high-frequency partner mode with the same number of antinodes in its standing wave pattern; for example, modes 34 and 8 in Fig. 7.11 both exhibit 8 antinodes.

We can understand this behavior as an undersampling effect for the shorter wavelength modes (low frequency modes) due to the discrete lumped-element nature of our metamaterial transmission line. Although non-ideal lumped element effects may be important, especially at short wavelengths, for now we assume that the currents and voltages are constant within each unit cell. Thus, we cannot sample the standing-wave structure on any finer scale

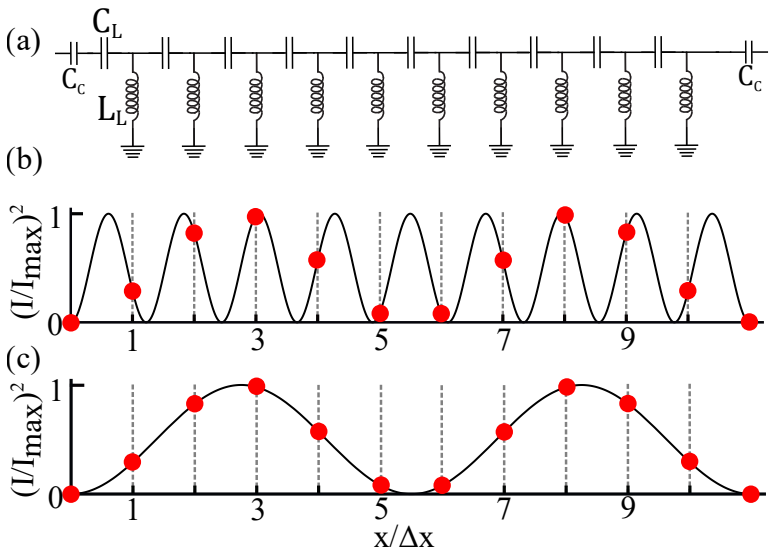

Figure 7.13: (a) Circuit schematics for ideal 10-cell metamaterial resonator. Waveform for square of standing-wave current for hypothetical continuous LHTL for (b) mode 8 and (c) mode 2 including red circles corresponding to location of each unit cell.

than the unit-cell length Δx. This can be seen in a simplified model of an ideal 10-cell metamaterial resonator with no stray reactances.

For now, we focus on the microwave currents in the inductors, but the same analysis would also apply to the voltages across the capacitors. Here we assume the standing-wave pattern for the current in a hypothetical continuous metamaterial is given by $\sin(k_n x)$ based on our open-ended boundary condition. Since the signal in the LSM images is proportional to the square of the local current density, in Fig. 7.13 we plot the square of this continuous waveform. The figure contains the continuous waveforms for a low-frequency mode $N - j$ and its partner high-frequency mode j, which are clearly different. However, with the points included on top of each curve corresponding to the unit cell locations, the undersampling of the lower-frequency mode results in the sampled wave patterns appear to be the same. This is consistent with the LSM images and the plot of ω_n vs. k_n in Fig. 7.12 if we extend the example case to $N = 42$ cell.

Besides a comparison with the LSM images, we can also use this approach to understand more details about the nature of the mode patterns in the metamaterial resonators. If we

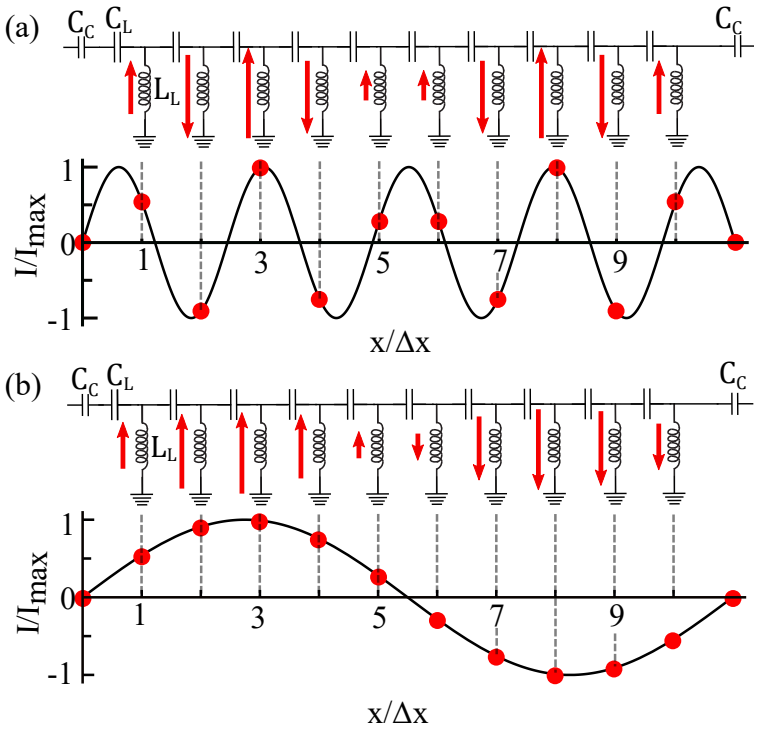

Figure 7.14: Circuit schematics for ideal 10-cell metamaterial resonators with arrows indicating relative sense of currents flowing in each unit cell along waveform for standing-wave current for hypothetical continuous LHTL and red circles corresponding to location of each unit cell for (a) mode 8 and (b) mode 2.

again consider the ideal 10-unit cell device but plot the local current vs. position rather than the square of the current, we can again compare the continuous waveform for the standing wave current along with the corresponding discrete values at each of the unit cells (Fig. 7.14). This approach indicates that modes $n > N/2$ should have currents that alternate in sign between adjacent unit cells, while for the higher frequency modes with $n < N/2$, the currents should flow in the same direction for all of the unit cells within a given half wavelength of the standing-wave pattern.

The LSM images also show an interesting beating-like pattern, especially for modes with n close to $N/2 = 21$. As shown in Fig. 7.15(a) there's a clear beating pattern for the mode $n = 23$. A line-cut scan in the center of the capacitors was taken and in Fig. 7.15(b) we plot the square root of the result from that line-cut and compare it with Fig. 7.15(c) based on the relation described previously that the LSM PR corresponds to the square of the local

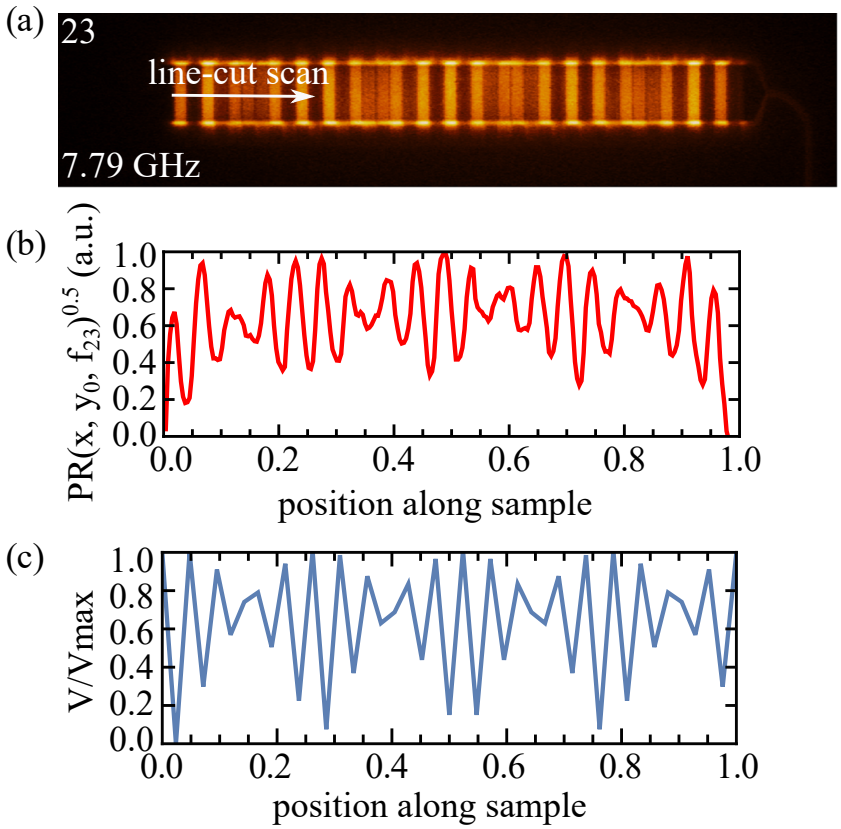

Figure 7.15: (Color online) Beating pattern caused by under-sampling effect: (a) LSM PR of mode 23 and an arrow showing the location and direction of the line-cut scan; (b) Square root of the line-cut of LSM photoresponse of mode 23 in the center of capacitors; (c) voltage standing wave pattern calculated by Eq. (8.5) of mode 23 of a 42 cell metamaterial resonator. The calculated wave pattern and the LSM PR both show a similar beating patter.

rf field. Fig. 7.15(c) is the calculated voltage standing wave pattern on the capacitors of mode $n = 23$, which will be discussed in detail in section 8.2.3. It can be found that they both exhibit a very similar beating pattern. The voltage of mode $n = 23$ at each unit cell is described by the magnitude of Eq. (8.5), which is a discrete sine wave. The agreement indicates that the under-sampling effect is the origin of the beating.

Chapter 8

Numerical simulations

In this chapter, I will describe two powerful numerical simulation tools that were used to study the behavior and properties of the metamaterial resonators: AWR Microwave Office and Sonnet. AWR simulations are a quick way to model the metamaterial spectrum with a lumped-element approach. But this approach has limitations of not being able to simulate the geometry effects of staggered inductors, non-ideal grounding, and the short-wavelength effects that deviate from ideal lumped-element behavior, etc. Sonnet on the other hand runs EM simulation of the actual sample layout with high accuracy but requires much longer time and massive computing resources. I will discuss the AWR simulations in section 8.1 and Sonnet simulations in section 8.2.

8.1 Lumped element circuit simulation using Applied Wave Research (AWR) Microwave Office

A lumped-element model simulation is very useful for understanding the behavior of a metamaterial resonator. We select Applied Wave Research (AWR) Microwave Office as the circuit simulation software.

Figure 8.1(a) shows the transmission spectrum $S_{21}(f)$ of a 42 cell metamaterial resonator.

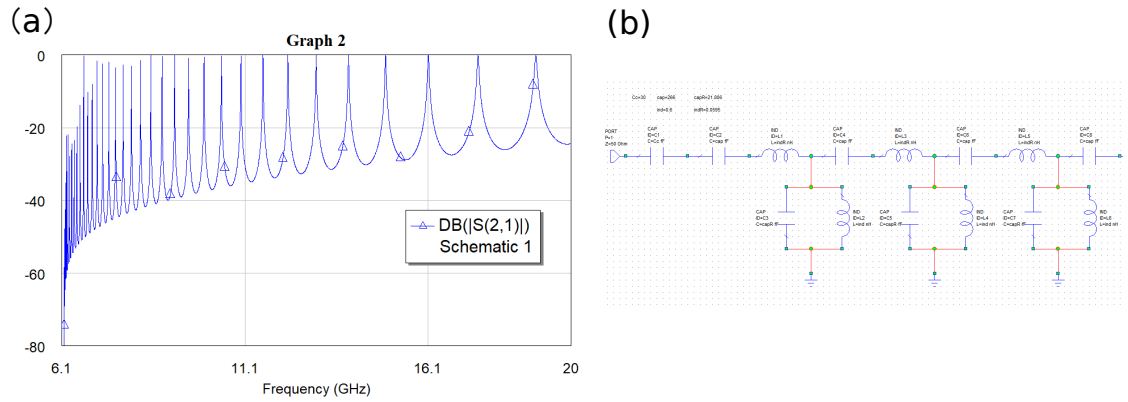

Figure 8.1: (a) AWR simulation S_{21} result of a 42 cell metamaterial with the parameters of $L_L = 0.625$ nH, $C_L = 250$ fF, $L_R = 59.5$ pH and $C_R = 21.8$ fF, consistent with the acutal metamaterial sample. (b) The left-end of the schematic of the metamaterial simulated by AWR.

AWR can only support a number of 10,000 steps when sweeping the frequency, so this spectrum is not going to reflect the actual peak height at low frequency end where the peaks are sharp and higher resolution is needed. Besides that, the lumped-element simulations will not reflect the the geometry effects of staggered inductors, non-ideal grounding, and the short-wavelength effects that deviate from ideal lumped-element behavior, etc. But it has the speed advantage: to obtain such a spectrum would only take a few seconds. Thus, we could always easily test our schematic in a very efficient manner. Fig. 8.1(b) is the circuit schematic of the input port, coupling capacitor of left-end and the first three cells of the metamaterial. The software supports many types of lumped-elements, which is very convenient.

8.2 EM field simulation using Sonnet software

Beyond the lumped-element circuit modeling with AWR, simulating the actual chip layout in an electromagnetic (EM) field solver is essential for interpreting the measurement results and improving the design. It can provide us a chance to test the design with different metal property, substrate property, and to make small changes in the design without actually

fabricating the sample and measuring it in the fridge. However, a real challenge is that to simulate a layout as large and complicated as our metamaterial resonator, it requires a significant level of computing resources. Here in the Plourde Lab at Syracuse University, we have a Sonnet software cluster that has 10 slave machines, each with 64 GB of memory, which is just powerful enough to handle the simulation. Through the generosity of the Sonnet company, which is located in Syracuse, we have been granted a complete license to the Sonnet software tool, allowing us to run complete simulations of our metamaterial resonators. Since we have gained a lot of very useful and important information about the metamaterial from Sonnet simulation, I will introduce both how to simulate metamaterial in Sonnet and discuss the simulation results in this section.

8.2.1 Sonnet Simulation setup

Although Sonnet is capable of simulation of multi-layer structures [111], we only need to use the simplest setting as a top dielectric layer plus a metal layer then a bottom dielectric layer corresponding to the Si substrate. In order to obtain better simulation results, all the conditions should be as close to the actual measurement as possible. Our metamaterial chip is a 90 nm thick layer of Nb on top of Si with no direct cover. So, first we import a gds file of the area that we are going to simulate. In order to get the most accurate result, simulating the entire 4×4 mm^2 area of the metamaterial resonator chip is ideal. However, the memory space required for this is far beyond the computing power we have, which would be impossible for Sonnet to simulate. Instead, we import a gds file that just covers the resonator with a reasonable width of ground-plane on the top and bottom as shown in Fig. 8.2, then we add input and output ports of 50 Ω on the edge of the left and right side of the CPW segment connecting to the metamaterial. The meshing size used here is 2 μm $\times$ 1 μm, which is the smallest feature size in the device layout. Any smaller meshing size would increase the memory required for the simulation that would either exceed the capability of our cluster or add an unreasonable amount on the simulation time.

The pressure inside the ADR at experimental temperature is in the range of 10^{-8} Torr. Thus, the top dielectric can be defined as vacuum. In our case, the parameters we chose are: thickness = 1100 μm , $\epsilon_r = 1$, $\mu_r = 1$, dielectric loss tangent = 0 and conductivity = 0. The

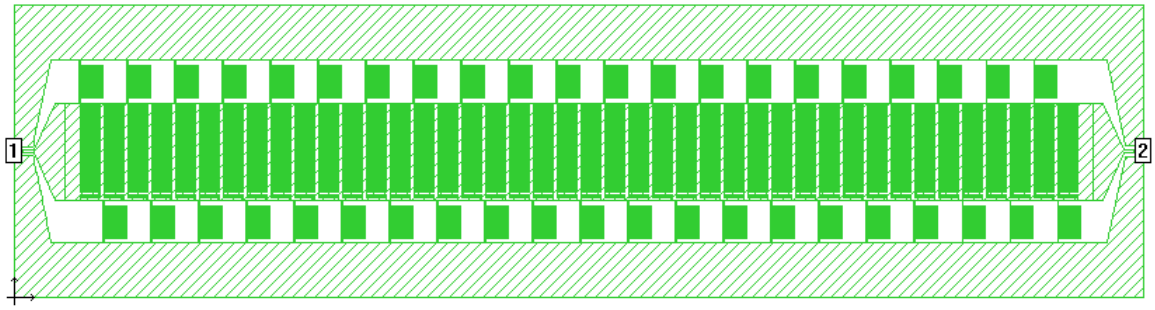

Figure 8.2: Sonnet simulation layout of the metamaterial resonator with the same geometry as the measured sample mabe of Nb.

metal can be defined as lossless since the measurement is done at 50 mK which is much colder than the T_c of Nb, so the resistive loss can be neglected. The bottom substrate is defined as Si with $\epsilon_r = 11.9$, $\mu_r = 1$, thickness = 500 μm, conductivity = 0. Based on various experiments looking at low-power, low-temperature measurements of superconducting resonators on Si, where the loss is limited by a distribution of two-level system defects at the surfaces and interfaces, we chose the dielectric loss tangent to be 5×10^{-6} [100, 101] even though it's much larger than the bulk loss tangent for Si. Since the internal loss expected in the metamaterial comes mainly from the capacitors, and the internal quality factor for capacitance in a LC oscillator would correspond to $Q_i = 1/\tan\delta$, the internal quality factor is expected to be around 2×10^5.

The next step is to define a frequency range and sweeping steps of the simulation. Since the peaks are very narrow and close in the low frequency end and there are no resonances expected below the infrared cut-off, we start the simulation from 3 GHz with 0.01 GHz stepsize up to 7 GHz and then 0.05 GHz step-size to higher frequency. The resolution is fine enough to find the peaks. Then we need to zoom-in on the peaks to find the actual shape and height. One technique within Sonnet that is quite helpful involves the "find Maximum using ABS" function for frequencies near the center of the resonance peaks.

8.2.2 Simulated transmission spectra

Sonnet does not have the frequency range limitation as we have in the actual microwave measurement setup, so we can easily extend the spectrum up to 50 GHz or higher if needed. Fig. 8.3(a) shows the S_{21} spectrum from Sonnet and comparison with measured S_{21} in Chap-

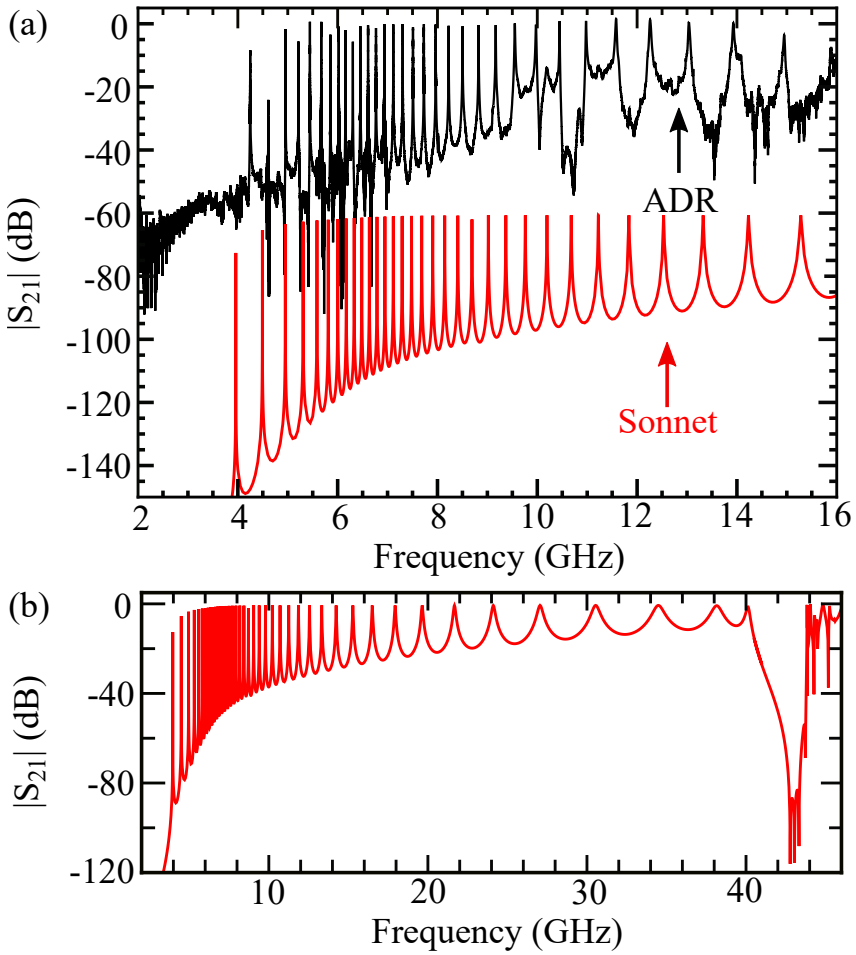

Figure 8.3: (a) $|S_{21}(f)|$ from Sonnet simulation offset by 60 dB compared with measured LHTL spectrum from ADR at 65mK. (b) $|S_{21}|$ from Sonnet simulation plotted out to 46 GHz showing gap beyond n=0 mode near 40 GHz ($n = 0$).

ter 7 (Fig. 7.3). The Sonnet simulation agrees with the measurement reasonably well. They both have the IR cut-off around 4 GHz and the first few modes deviate from the ideal dispersion for both cases. The Sonnet spectrum also has the highest density of peaks around 6 GHz. The smallest mode-spacing is around 150 MHz, which is the spacing of 31st mode

and 30^{th} mode. By extending the Sonnet simulation beyond the 16 GHz upper limit of our measurement range, we observe that 40 GHz marks the end of the first 42 modes. Then we find a gap in between 40 GHz and 44 GHz. As discussed in Sec. 5.2, the above evidence shows that we have successfully realized a 42 cell LHRH transmission line resonator. The left-handed branch has the zeroth order mode at 40 GHz and the 41^{st} mode at 4 GHz. The two zeroth order modes – one at the lower end of the gap and the other at the upper end – correspond to the self-resonance frequencies of indutor or capacitor in each unit cell. The Sonnet self-resonance simulation results of the inductor and capacitor that were discussed in Chapter 6 suggest that the self-resonance frequency of the capacitor to be lower than the inductor. Based on that, we can estimate the stray reactances values to be $L_R = 59.5$ pH and $C_R = 21.8$ fF, respectively.

8.2.3 Current/charge density simulation

Sonnet also provides us with the ability of simulating the spatial distribution of the current and charge density for any given frequency. We extract the center frequency for each of the metamaterial resonator modes from the $S_{21}(f)$ simulation. We then select the Sonnet settings to perform either a current or charge density simulation with the frequency point as individual resonance frequencies. This type of simulation requires a significant amount of time compared to the simple transmission simulation. However, we only need a few dozen frequency points since we are primarily interested in the current and charge density patterns on resonance. So, the overall time to run the current density simulation of all 42 modes would be less than two days if we use all of the computing resources available in our cluster. The result automatically contains both the information of current and charge density of both magnitude and phase. The software itself would only be able to plot the magnitude, but users can always save all the data and separately plot the real or imaginary part if needed. Depending on the actual size of the simulation area and how we select the mesh size, the data files could be quite large.

We simulated the current/charge density distribution of the metamaterial resonator for all of its left-handed resonance frequencies. From the result, we found clear standing wave patterns for both current and charge densities. In the charge density simulations, the capacitors have a much stronger response than the inductors, while in the current density, the inductors show stronger reactance. This phenomenon is consistent with LC oscillators, where most of the electric energy is stored in capacitors, which have high charge density, and most of the magnetic energy would be stored in the inductors, which have high current density.

Like the LSM imaging results, the Sonnet charge/current density [Fig. 8.5(a) and 8.4(a)] also exhibits the undersampling effect discussed previously. The number of anti-nodes in the charge density distribution for pairs of modes, p and $N-p$, is equal to p for both modes. The current density distributions exhibit a similar effect at low frequency. Both modes p and $N-p$ have the same number of antinodes in the current density patterns, but now there is also an added phenomenon that the position of the antinodes between the low-n and high-n modes has a half wavelength shift.

Following Chapter 5, a discrete transmission line resonator with open-ended boundary conditions would have the voltage and current at cell m as:

$$V_m = V_0 \left[e^{-jm\beta\Delta x} + e^{j(m-1)\beta\Delta x} \right] \tag{8.1}$$

$$I_m = I_0 \left[e^{-j(m+\frac{1}{2})\beta\Delta x} - e^{j(m-\frac{1}{2})\beta\Delta x} \right]. \tag{8.2}$$

If we fold the dispersion relation around the y-axis into the first quadrant, as discussed in Chapter 5, the voltage and current of the n-th resonance become:

$$V_{m,n} = V_0 \left[e^{-jm\frac{n}{N}\pi} + e^{j(m-1)\frac{n}{N}\pi} \right] \tag{8.3}$$

$$I_{m,n} = I_0 \left[e^{-j(m+\frac{1}{2})\frac{n}{N}\pi} - e^{j(m-\frac{1}{2})\frac{n}{N}\pi} \right]. \tag{8.4}$$

Here the voltage represents the voltage on each cell to the ground and the current represents

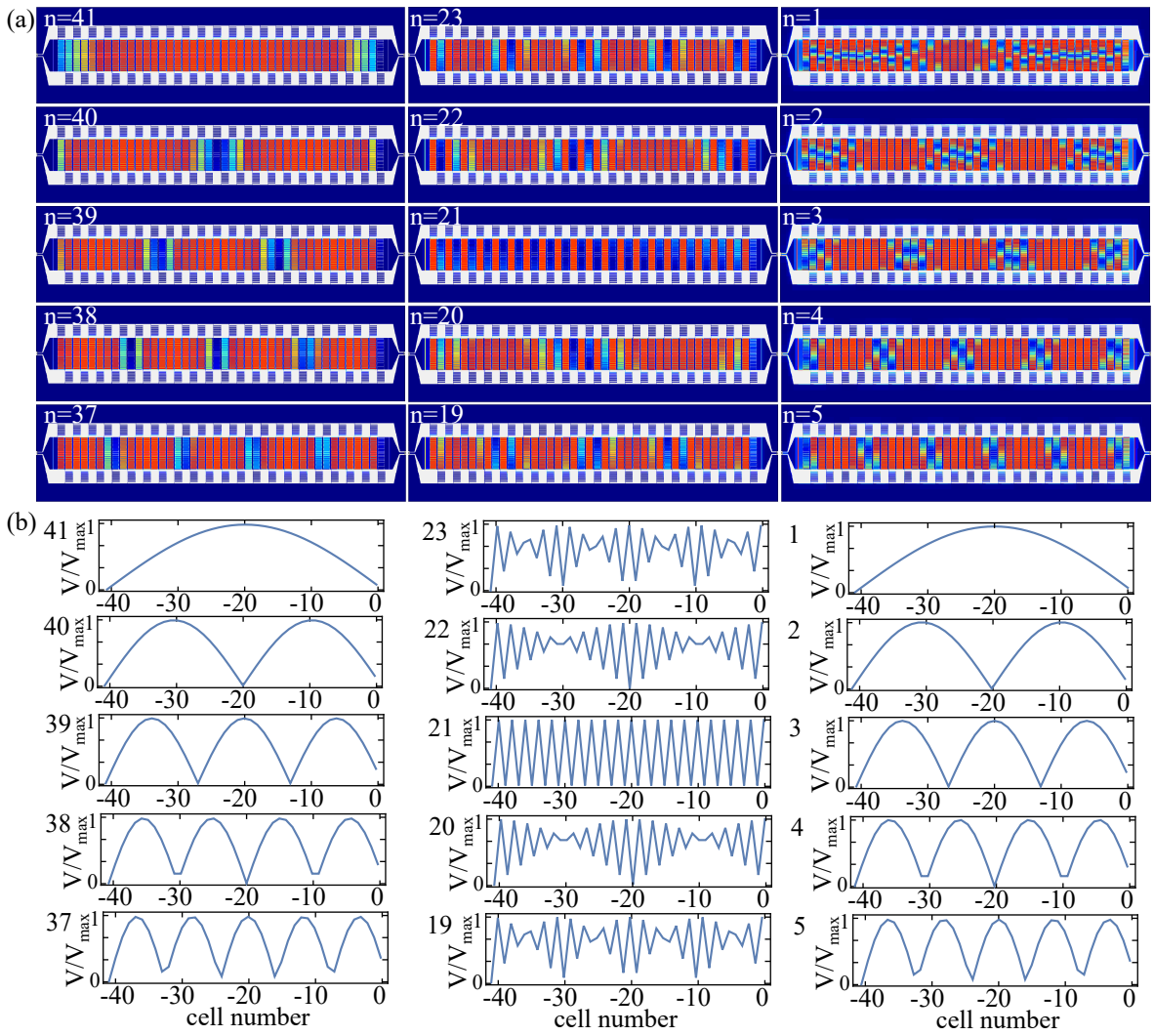

Figure 8.4: (a) Sonnet charge density simulation result labeled by the mode number. The color bar is not shown for each individual image but red means high response and blue means low response. Similarly to the LSM images, the high frequency modes on the right column show clear standing wave patterns as well as the low frequency modes on the left column but with under-sampling effect. The high frequency modes appear to have in-cell modulations. The pairing modes from the left column and the right column are appear to be in phase. (b) Plot of standing wave patter of voltage from Eq. (8.5) to compare with charge density patterns.

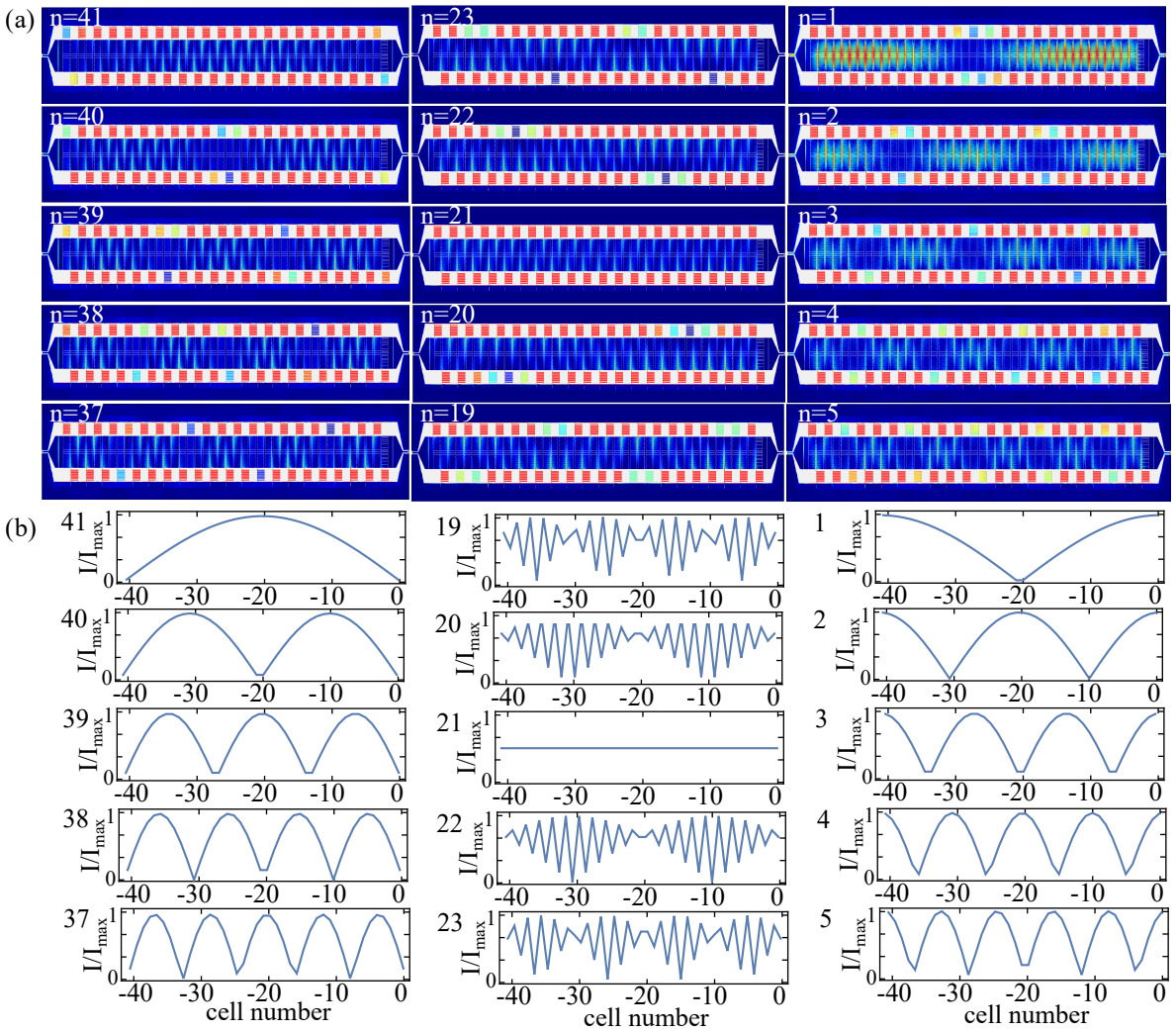

Figure 8.5: (a) Sonnet current density simulation result labeled by the mode number. Similarly to Fig. 8.4(a), the color bar is not shown for each individual image but red means high response and blue means low response. The color scale is different for each image and these are not included here for clarity. The high frequency modes on the right column show clear standing wave patterns as well as the low frequency modes on the left column but with under-sampling effect. The pairing modes from the left column and the right column, which means the $n = p$ and $n = 41 - p$, exhibit the same number of antinodes. However, the positions of the antinodes have a half-wavelength shift. (b) Plot of standing wave patterns of current from Eq. (8.6) to compare with current density patterns.

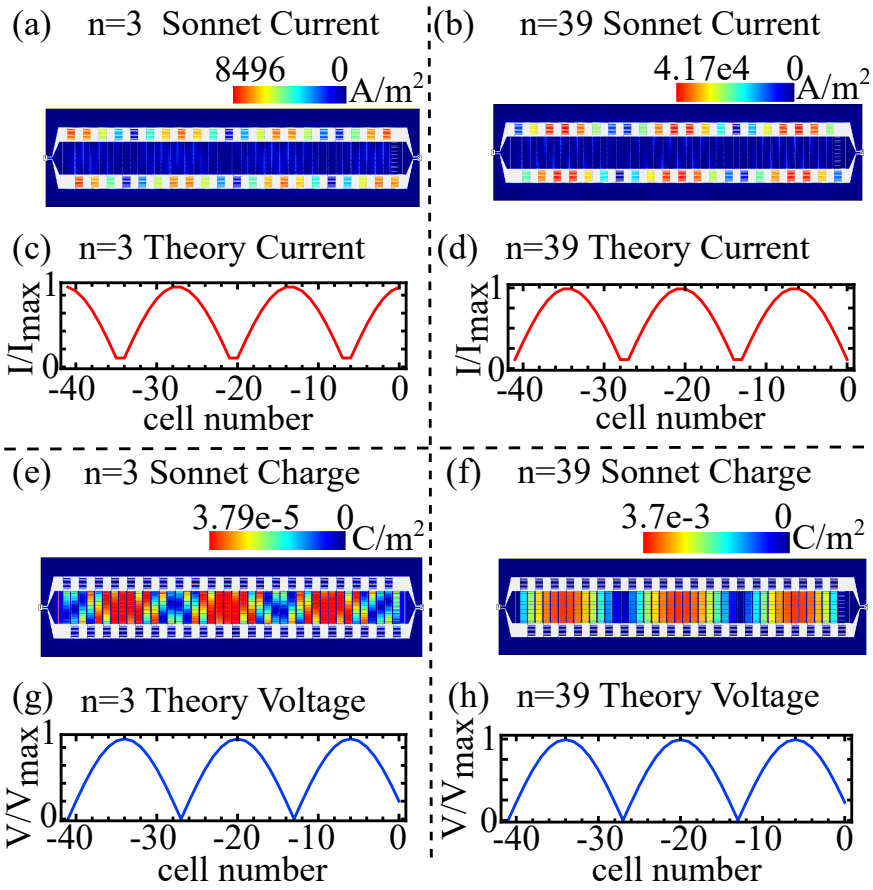

Figure 8.6: Current and charge density pattern of a 42-cell LHTL resonator with the same geometry of the sample we measured and discussed in the main paper simulated by Sonnet and compared with Eq. (8.5) and (8.6) with corresponding value of mode number n: (a) Sonnet current density at the $n = 1$ mode, (b) Sonnet current density at the $n = 39$ mode, (c) plot of Eq. (8.5) at $n = 3$ mode, (d) plot of Eq. (8.5) at $n = 39$ mode, (e) Sonnet charge density at $n = 3$ mode, (f) Sonnet current density at the $n = 39$ mode, (g) plot of Eq. (8.6) at $n = 3$ mode, (h) plot of Eq. (8.6) at $n = 39$ mode.

the current through each cell. Thus, the voltage across each capacitor of the LHTL is the voltage difference of neighboring cells: $V_{C_L,m} = V_{m-1} - V_m$ and the current flowing through the inductor is the current difference of neighboring cells: $I_{L_L,m} = I_{m-1} - I_m$. Therefore, on resonance n, the voltage across capacitor m and the current through inductor m are given

by:

$$V_{C_L,m,n} = 2V_0 \sin\left[(m-1)\,\frac{n\pi}{N}\right]\left[\sin\left(\frac{n\pi}{N}\right) + j - j\cos\left(\frac{n\pi}{N}\right)\right] \tag{8.5}$$

$$I_{L_L,m,n} = 2I_0 \cos\left[\left(m-\frac{1}{2}\right)\frac{n\pi}{N}\right]\left[1-\cos\left(\frac{n\pi}{2N}\right) - j\sin\left(\frac{n\pi}{2N}\right)\right]. \tag{8.6}$$

The charge density, which is related to the voltage across the capacitors, and the current density, which is related to the current through the inductors, in the Sonnet images can be compared with the magnitude of the quantities described by Eqs. (8.5)-(8.6). As shown in Figs. 8.4(a) and 8.5(a), these expressions are in good agreement with the charge and current density distributions from the Sonnet images. In the limit of small n and large N, we have:

$$|V_{C_L,m,1}| \sim 2V_0\left|\left(\frac{\pi}{N}\right)\sin\left[\frac{(m-1)\,\pi}{N}\right]\right| \tag{8.7}$$

$$|I_{L_L,m,1}| \sim 2I_0\left|\left(\frac{\pi}{N}\right)\cos\left[\frac{\left(m-\frac{1}{2}\right)\pi}{N}\right]\right|. \tag{8.8}$$

From Eqs. (8.7)-(8.8), the voltage and current on resonance are close to out of phase spatially, as we expect to see in a continuous right-handed resonator. On the other hand, in the limit of $n = N-1$, we have:

$$|V_{C_L,m,N-1}| \sim 4V_0\left|\sin\left[\left(\frac{N-1}{N}\right)(m-1)\,\pi\right]\right| \tag{8.9}$$

$$|I_{L_L,m,N-1}| \sim 4I_0\left|\sin\left[\left(\frac{N-1}{N}\right)(m-1)\,\pi\right]\right|, \tag{8.10}$$

thus, the voltage and current standing wave patterns are now in phase spatially. Although this is counter-intuitive, it is supported by Sonnet simulations (shown in Fig. 8.6) that the current and charge are out of phase for the $n = 3$ mode but in phase for the $n = 39$ mode. The LSM imaging experiments on our metamaterial resonators also exhibit this behavior. Shown in Fig. 8.7, although the LSM signal in the inductors is considerably weaker than in the capacitors, we can still see some evidence that the antinodes in the inductors are shifted

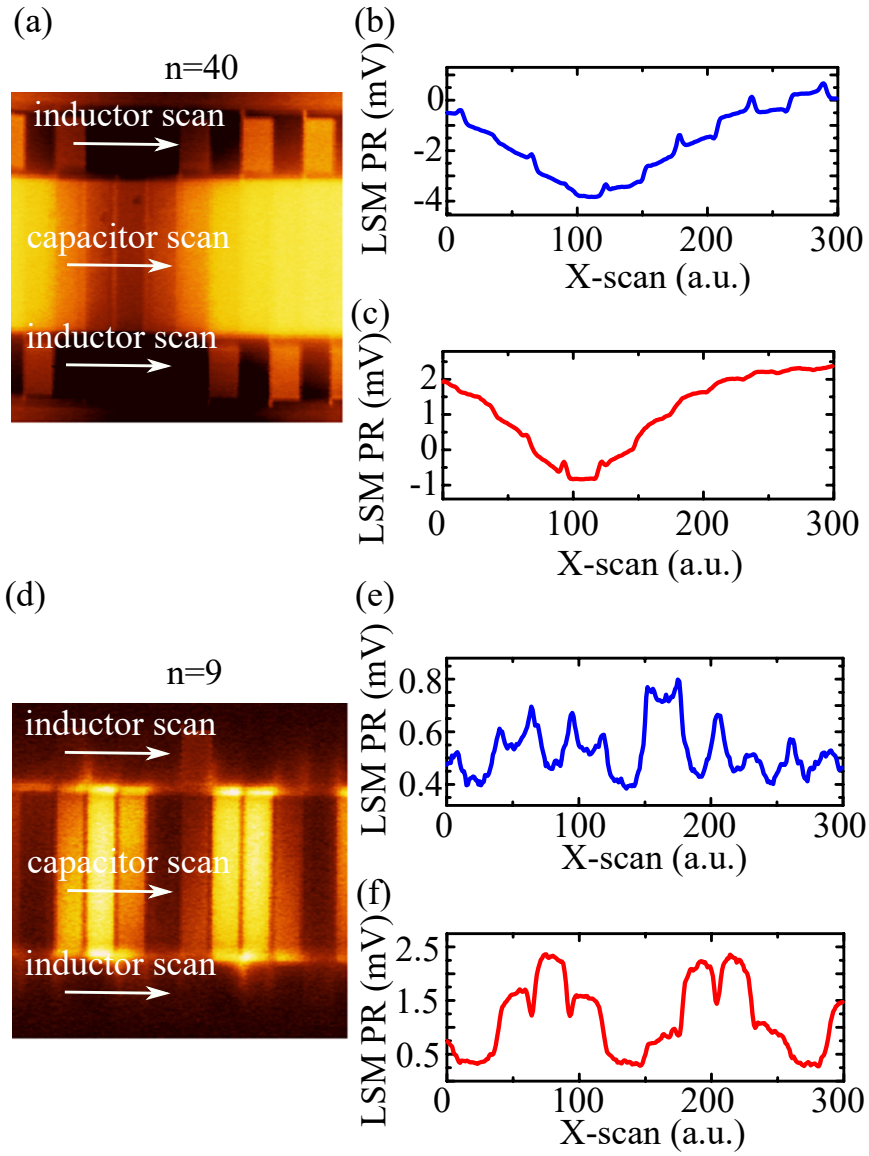

Figure 8.7: The high-resolution LSM images of $n = 40$ and $n = 9$ modes. (a) high-resolution image of 11 cells of $n = 40$ mode. (b) sum of the LSM PR line-scan near the center of inductors on the top and bottom. (c) LSM PR line-scan near the center of capacitors. (d) high-resolution LSM imaging of 11 cells of $n = 9$ mode. (e) sum of the LSM PR line-scan near the center of indutors on the top and bottom of $n = 9$ mode. (f) LSM PR line-scan near the center of capacitors of $n = 9$ mode. For $n = 40$ mode, the response of inductors and capacitors are clearly in phase. For $n = 9$ mode, the response of inductors and capacitors are out of phase, although the PR signal in the inductors is rather weak.

with respect to those in the capacitors at high frequencies, while for the low-frequency resonances, they line up.

The same analytic analysis applies also to the discrete RHTL resonator. Eqs. (8.1)-(8.2) are just current through inductors and voltage across the capacitors, so when n is small, like $n = 1$, we have:

$$|V_{C_R,m,1}| \sim 2V_0 \left|\cos\left(\frac{2m-1}{2N}\pi\right)\right| \tag{8.11}$$

$$|I_{L_R,m,1}| \sim 2I_0 \left|\sin\left(\frac{m\pi}{N}\right)\right|. \tag{8.12}$$

The voltage and current standing wave patterns from these two expressions are close to be spatially out of phase, as one would expect for a continuous right-handed resonator. In the high-n limit, for $n = N - 1$, voltage and current standing wave patterns become:

$$|V_{C_R,m,N-1}| \sim 2V_0 \left|\sin\left(\frac{N-1}{N}m\pi\right)\right| \tag{8.13}$$

$$|I_{L_R,m,N-1}| \sim 2I_0 \left|\sin\left(\frac{N-1}{N}m\pi\right)\right|. \tag{8.14}$$

As with the LHTL standing wave patterns in the high-n limit, the voltage and current distributions are spatially in phase. We have also confirmed this behavior through Sonnet simulations of a discrete RHTL. To summarize, for a discrete transmission line resonator – with either a left- or right-handed dispersion relation, for small n modes, the antinodes in the voltage and current standing wave patterns will be spatially out of phase, while for large n modes, they will approach being spatially in phase.

8.2.4 Quality factor

As with the experimental measurements, we can extract the quality factor for each resonance from the Sonnet simulations of $S_{21}(f)$ through the same fitting procedure using Eq. (7.1) to fit the resonance trajectory of $S_{21}(f)$ in the complex plane and extracting Q_c and Q_i using

Eq. (7.3).

As described previously, for the Sonnet simulations, loss was included as a substrate dielectric loss, while the metal traces were modeled as lossless components. So, the internal quality factor Q_i for each mode is expected to be dominated by $1/\tan\delta$, where $\tan\delta$ is the dielectric loss tangent that can be defined directly in the Sonnet substrate loss parameters. As discussed in Section 8.2.1, this value is set to be 5×10^{-6}. In Fig. 8.8, it's clear that the first few low frequency modes have almost constant Q_i that is very close to $1/\tan\delta$. At high frequency, where Q_c is much larger than Q_i and extracting Q_i becomes more difficult, the internal loss has increased somewhat, although the resonances in this regime are still strongly overcoupled.

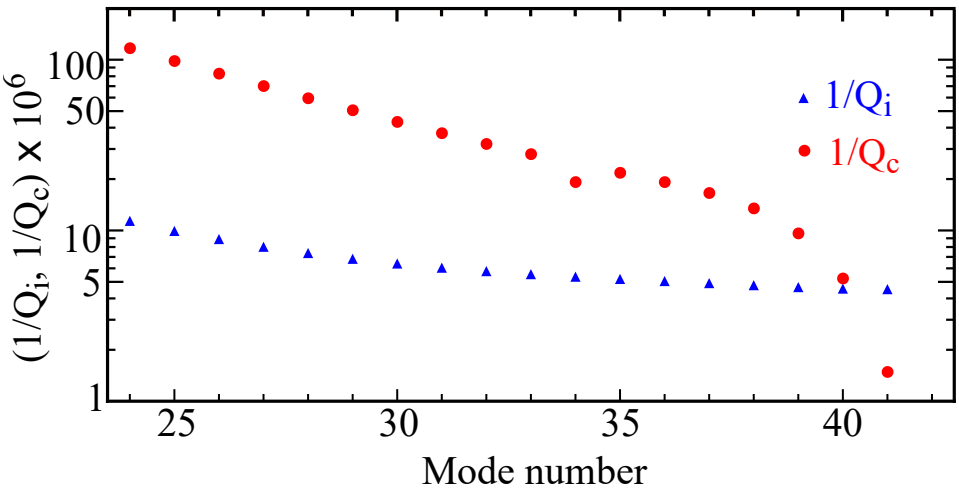

Figure 8.8: Q_i and Q_c values extracted from Sonnet $|S_{21}(f)|$ simulation. The substrate loss tangent is set to be $\tan\delta = 5 \times 10^{-6}$.

The coupling quality factor Q_c for each mode from the Sonnet simulation can also be extracted from the resonance fits following the same procedure as was applied to the fits of the experimental data. However, unlike the fits to the experimental resonances that were subject to uncertainties in the baseline transmission, the Sonnet simulation results do not have such an issue since the simulated transmission is normalized perfectly. The coupling loss for the various resonances from the Sonnet simulations are shown in both Fig. 8.8 and Fig. 8.11. Overall, the result is similar to the theoretical curve which is quite low for high-n

modes and with a rapid increase as the mode number decreases. While at the low-frequency end of the spectrum, the Sonnet result for coupling loss is higher compared to the theoretical prediction from Eq. (5.38).

8.2.5 Effects of inductor staggering in metamaterial resonators

As introduced in Chapter 6, our metamaterial resonator layout has the inductors of neighboring cells directed in opposite directions. We can examine the effects of this staggered arrangement for the inductors in Sonnet and compare with the spectra for a non-staggered inductor layout.

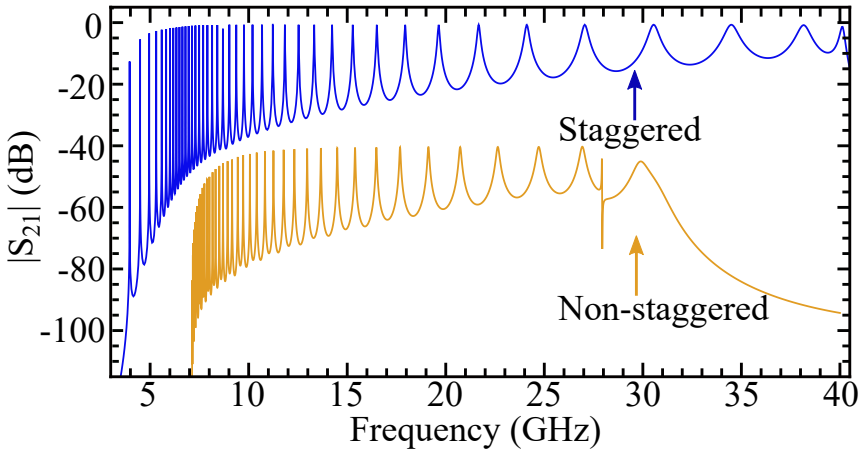

Figure 8.9: $|S_{21}(f)|$ spectrum of Sonnet simulation of non-staggered 42 cell LHTL resonator and comparison with staggered geometry spectrum. The former is shifted down by 40 dB for clarity.

To make this comparison, we construct a similar LHTL pattern in Sonnet like the staggered one, but with all the inductors connecting to the upper ground plane. The capacitor finger width, length, spacing, number of pairs and the meander-line width and number of turns are kept the same to maintain the unit cell capacitance and inductance. In order to avoid the inductors overlapping with each other, the interdigitated capacitor spines are widened so the unit cell size will increase to 66 μm, which results in the total length of a 42 cell design being increased by 252 μm. With all other conditions and parameters unchanged, we simulate this geometry in Sonnet to find the S_{21} spectrum.

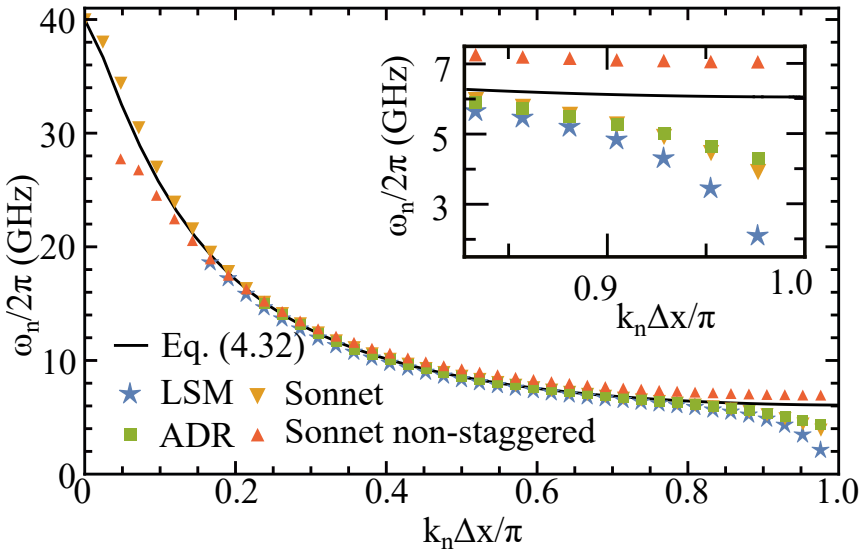

Figure 8.10: The comparison of dispersion with normalized wave number between the theory curve, experimental results from ADR measurements, $S_{21}(f)$ measurement done with LSM, Sonnet simulation of the staggered inductor configuration and non-staggered inductor configuration. The inset is a zoomed-in plot of the low-frequency end of the spectrum.

As shown in Fig. 8.9 and Fig. 8.10, the staggered and non-staggered configurations have some significant differences. First, the cut-off is 2 GHz higher for the non-staggered configuration compared to the staggered inductor layout. Second, the non-staggered spectrum exhibits the highest mode density just above ω_{IR}, as expected from the theoretical prediction [Eq. 4.11)]. Third, dispersion of the modes for the non-staggered layout comes quite close to the dependence given by the theoretical expression over most of the range. Fourth, the gap at the high-frequency end of the spectrum appears at a significantly lower frequency compared to the staggered inductor case. These phenomena suggest that both geometries have extra loading effects for the high-n, low-f modes, which deviate the dispersion from the theory curve. The fact that the non-staggered configuration has condensed modes at the low frequency end while all the measurements and simulation of the staggered one do not indicate that the deviation from the theory curve of our staggered design is mainly a geometry issue. Some in-cell dynamics that are not captured by the LHTL theory discussed in Chapter 4 in the staggered LHTL could prevent modes being too close to each other at low frequency.

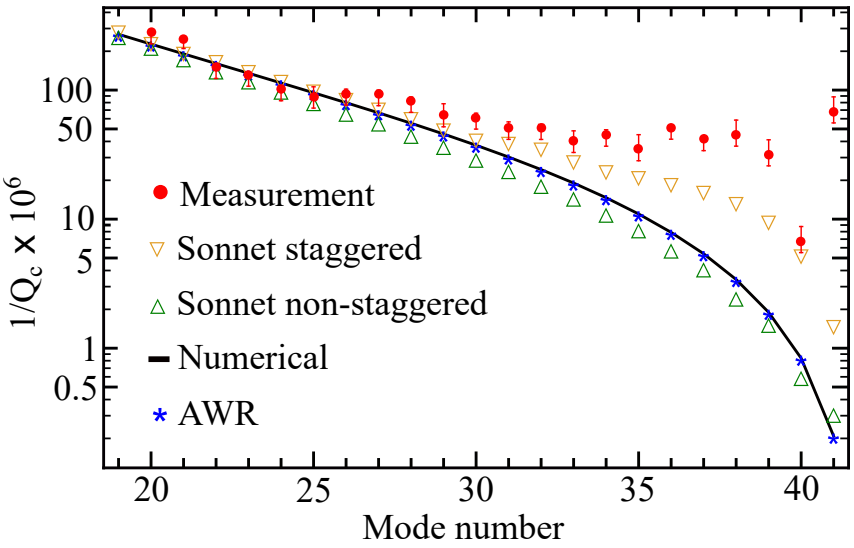

Figure 8.11: Coupling loss vs. mode number from Fig. 7.4 with the results from the Sonnet simulations of the non-staggered inductor configuration included.

In addition to comparing the spectra and dispersion relations, it is also illuminating to compare the coupling loss for the different inductor configurations. As shown in Fig. 8.11, when we place the inductors all on one side for the non-staggered layout, the coupling loss for the low frequency peaks match closely to the theory curve and pure lumped-element simulation from AWR. On the other hand, for the staggered inductor configuration, the coupling loss is enhanced at low frequency and high n. Overall, the effect of staggering the inductors is very complicated. At low frequency end, the not-staggered configuration matches the LHTL better while at high frequency, the staggered one is closer to the LHTL.

8.2.6 Effect of imperfect grounding

In the measurement setup, the chip was grounded via aluminum wire bonds to the sample holder's grounding edge. There were also jumper wires across the left-handed line structure and CPW regions to ensure the ground plane was as close to a uniform equipotential as possible. However, the wire bonds themselves have self inductance, which can limit the performance of the ground plane across the entire area of the chip. Here, we simulate the imperfect grounding condition using Sonnet to see how much it will affect the spectrum and

coupling quality factor.

The typical grounding setup in Sonnet involves defining a grounding box and attach the metal layer boundaries to the sides of the grounding box. The grounding box and the drawing are normally both rectangular to fit exactly to each other, thus the metal layer is perfectly grounded. Here, we study four different grounding conditions. First is the conventional setup as described before. This is by default a perfect grounding condition so we call it "grounded ". Second, we make the grounding box bigger than the metal layer area and then use twelve 6×200 μm^2 metal strips to connect the device area to the grounding box to mimic the use of wire bonds to establish the ground connections on the experimental devices. This setup is referred to as "12 bonds". Although the actual wire bonds would have dimensions around 32×500 μm^2, we designed the strips with this size to enhance the effects of an imperfect grounding configuration. Third, we reduce the number of the metal strips to 3 to create an even worse grounding configuration and we refer to this as "3 bonds". Fourth, we completely separate the metal and the grounding box so that there is no dc path to ground at all and we refer to this configuration as "floating". These four conditions are marked as "Grounded", "12 bonds", "3 bonds" and "Floating" in the Fig. 8.12 respectively.

As shown in Fig. 8.12, they do have some systematic differences. The plot in Fig. 8.12(a) indicates that the coupling loss increases as the grounding condition becoming progressively worse from perfectly grounded to floating. The effect is especially strong for the first few low frequency modes. This means that if the sample is not well grounded, the first few low frequency resonance peaks would get broader due to higher coupling loss. On the right, we can see that the bad grounding conditions would push the low frequency modes to even lower frequencies. This effect can explain the frequency deviation from the theory curve. And it is clear that with worse grounding, the frequency shift is bigger. The imperfect grounding effect becomes weaker as the frequency goes higher. After about 10 modes counting from low frequency end, the grounding condition effect becomes hard to notice.

Frequency shifts due to the grounding issues are also found in the LSM experiments.

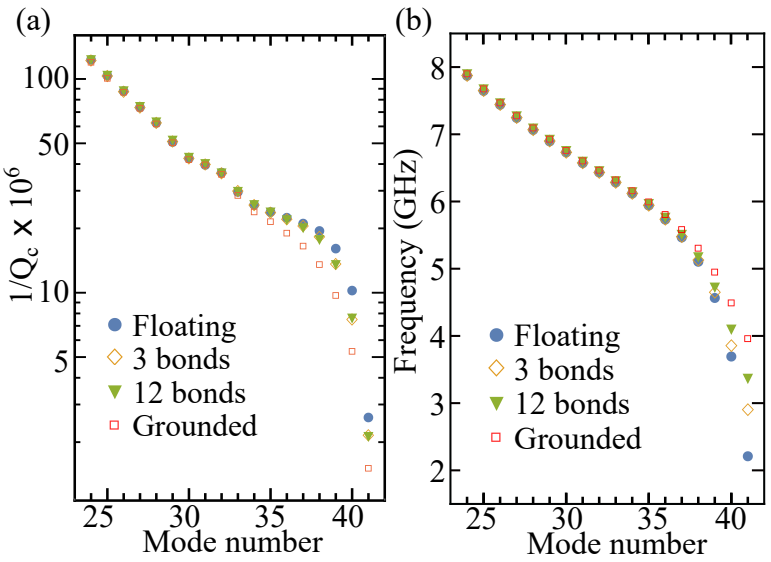

Figure 8.12: (Color online) We have simulated four different grounding conditions in Sonnet as discussed in the section 8.2.6. (a) The coupling losses for these four different conditions extracted using Eq. (7.1). (b) The dispersion of these four conditions. It's clear that the imperfectness in the grounding could increase the coupling loss and push the low frequency modes to even lower frequencies.

LSM requires a laser beam shinning on the sample, so the jumper wires across the LHTL region have to be removed. This will make the ground planes on the two sides of the LHTL have possible imbalanced potential (which is not easy to simulate in Sonnet). By comparing the S_{21} spectrum before and after removing the wires, we find the first few peaks are all lower than the measurement without removing the jumper wires shown in Fig. 8.10. The above discussion shows that the grounding condition of the sample is very critical for getting a well behaved left-handed transmission line resonator.

Chapter 9

Ongoing and future work: Metamaterial resonator coupled to a transmon qubit

One direct and exciting application of the metamaterial resonator is to realize a high-density spectrum of modes coupled to qubits. As introduced in the Chap. 1, multi-mode coupling and entanglement is always an interesting and fascinating topic in cQED and even in the entire quantum information processing area. The metamaterial resonator provides us a possible way of engineering a high-density spectrum in the GHz range with limited chip area requirement. It also has an IR-cutoff, so the flux-tunable transmon qubit can be prepared at a certain state without strongly interacting with the metamaterial modes. Based on all the above benefits and some other advantages over the traditional CPW type resonator, the metamaterial resonator is a very promising cavity candidate for multi-mode coupling to a qubit.

In conventional cQED, the transmon qubit is normally capacitively coupled to the voltage anti-node of the transmission line resonator. The open-ended boundary condition would make sure the voltage anti-node is at the end of the transmission line for all the possible

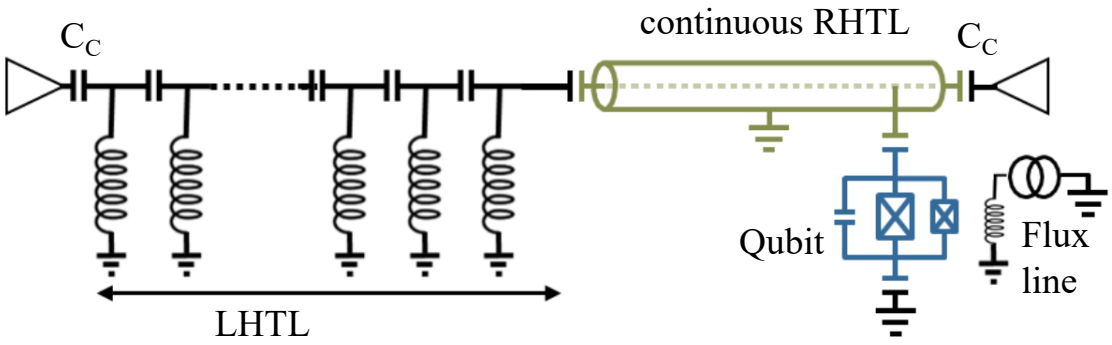

Figure 9.1: The schematic of a transmon qubit coupled near the voltage antinode of the RH part of a hybrid transmission line resonator. The qubit is drawn to be asymmetric for a general case.

resonance modes. Thus, if the coupling strength of the qubit to the cavity is stronger than the mode spacing, the qubit would automatically couple to multiple modes of the cavity at the same time, like in Ref. [112] where an extremely long CPW resonator with a quite low fundamental resonance was used for that purpose. As discussed in Chapter 5 and 8, unlike the CPW resonator, there's no universal voltage or current anti-node for all the modes in the metamaterial resonator for the qubit to couple. To solve this problem, Daniel Egger and Frank Wilhelm from Saarland University proposed a novel approach: instead of using only a LHTL resonator, one can couple a continuous RHTL like a CPW to one end of the LHTL to form a hybrid transmission line and apply open-circuit boundary condition to this TL to form a hybrid cavity [3]. The two directly coupled transmission lines should have the same impedance to avoid impedance mismatch. Shown in Fig. 9.2, the hybrid cavity would still have a high density of peaks and IR-cutoff at the low-frequency band edge, behaving similarly to a LHTL, while the voltage spatial distribution of the RH part would remain almost the same for the modes that are close in frequency. Thus, coupling a qubit to the end of the RH part would ensure the qubit being coupled to the voltage anti-nodes of the entire hybrid cavity.

The conventional cQED physics also applies to the hybrid cavity-qubit system. A qubit described by the Pauli matrices $\hat{\sigma}_{x/z}$ coupled to the hybrid cavity with coupling strength g_n

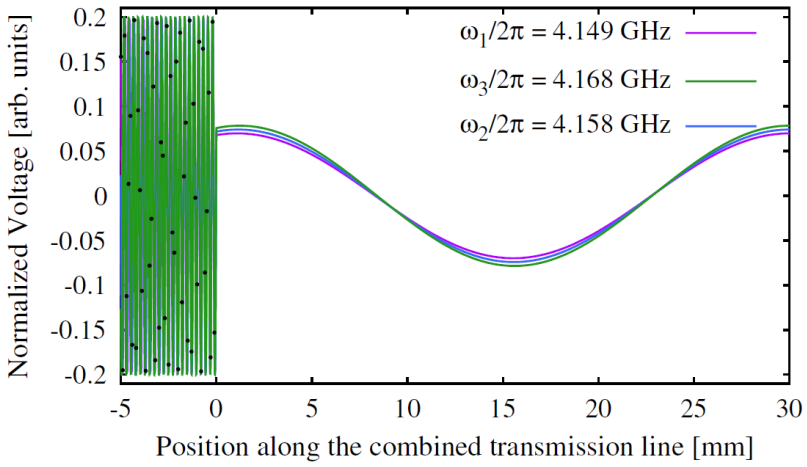

Figure 9.2: From Egger and Wilhelm 2013–The standing wave patterns of the first three modes of a hybrid transmission line cavity counting from low frequency end. Image taken from Ref. [3]. The LHTL part has 200 unit cell measuring 100 μm each. $\omega_{IR}/2\pi = 4$ GHz. The RHTL part is 3 cm long with $C_r = 1667$ fF/μm and $L_r = 4167$ pH/μm. It's clear that the voltage standing wave patterns in the RH part are almost the same for the first three modes of the hybrid cavity.

for mode n would have the Hamiltonian of

$$\hat{H}/\hbar = \omega_q \hat{\sigma}_z/2 + \sum_n \omega_n \hat{a}_n^\dagger \hat{a}_n + \sum_n g_n \hat{\sigma}_x \left(\hat{a}_n^\dagger + \hat{a}_n\right), \tag{9.1}$$

where ω_n is the frequency of mode n and $\hat{a}_n^\dagger$ ($\hat{a}_n$) is the creation (annihilation) operator for that mode [3]. If the qubit is coupled to the cavity, at the degeneracy point where the qubit frequency is very close to the cavity mode frequency, a vacuum Rabi avoided crossing of $2g$ is expected [74]. We designed and fabricated a hybrid cavity coupled to a flux-tunable transmon qubit and measured the transmission $|S_{21}(f)|$ as a function of the qubit flux bias.

9.1 Transmon qubit

Here we briefly discuss the transmon qubit. Ideally, a qubit is a quantum two-level system. In cQED, typically the ground state and the first excited state of a superconducting nonlinear quantum LC circuit form the qubit basis states. The transmon qubit is a capacitively

shunted nonlinear inductance, which is typically coupled to a transmission line cavity for readout and coupling to other qubits [12, 113]. The nonlinearity comes from the low-loss nonlinear inductor formed from a Josephson junction [71]. The junction consists of two superconducting electrodes that are separated by a thin insulating barrier that allows a supercurrent of Cooper pairs to tunnel across the barrier where the current depends on the phase difference ϕ between the superconducting wavefunctions on either side of the barrier: $I = I_0 \sin\phi$, where I_0 is the critical current of the junction [97]. This is called the Josephson effect and it results in the junction behaving like a nonlinear inductance:

$$L_J = \frac{\Phi_0}{2\pi I_0 \cos\phi}, \tag{9.2}$$

where $\Phi_0 \equiv h/2e$ is the magnetic flux quantum [74]. The characteristic energy scale for a junction is the Josephson energy E_J [74]:

$$E_J = I_0 \Phi_0 / 2\pi. \tag{9.3}$$

In our case, a configuration of using two junctions in a superconducting loop to make a SQUID allows for E_J to be tuned periodically with magnetic flux [114]. A large capacitor with capacitance C_B is connected with the two Josephson junctions in parallel which gives the qubit total charging energy of

$$E_C = e^2/2C_\Sigma, \tag{9.4}$$

where $C_\Sigma = C_B + C_J + C_g$ is the total of the qubit capacitor capacitance, the junction capacitance, and the capacitance to the environment, respectively [113]. The transmon qubit is working in the regime where E_J/E_C is in the range of $\sim 20 - 200$. The two junctions that are used in the transmon may have different Josephson energies, E_{J1} and E_{J2}. If we define the energy ratio as $\alpha = E_{J1}/E_{J2}$ and the total energy as $E_{J\Sigma} = E_{J1} + E_{J2}$, we then would

have the flux-dependent total Josephson energy as:

$$E_J(\Phi) = E_{J\Sigma} \cos\left(\frac{\pi\Phi}{\Phi_0}\right) \sqrt{1 + d^2 \tan^2\left(\frac{\pi\Phi}{\Phi_0}\right)}, \tag{9.5}$$

where $d = (\alpha - 1)/(\alpha + 1)$ [114]. Thus the qubit frequency can be tuned by an external flux and have the periodicity of Φ_0 [113]. Nowadays, scientists know a lot about the transmon qubit and its implementation in cQED. So, we could just proceed with substituting the transmission line cavity with a hybrid cavity and couple it to a transmon qubit to test the idea of dense spectrum coupling.

9.2 Sample design

The hybrid cavity and qubit require much more space than the metamaterial resonator alone. So a bigger sample holder which can fit a chip with an active area of 6.25×6.25 mm^2 is used. Fig. 9.3(a) shows the circuit diagram illustrating how the qubit is coupled to the hybrid cavity. Fig. 9.3(b)-(d) shows optical micrograph images of one of these devices. The hybrid cavity is placed on the top part of the chip. The LH part has the same size and parameters as our previous metamaterial resonators discussed in the earlier chapters: 42 unit cells of interdigitated capcitors in series and staggered meander-line inductors, and the input gap capacitor is chosen to be 5 μm wide to provide $\sim$ 25 fF of coupling capacitance, which is slightly smaller than the measured metamaterial discussed in the previous chapters in order to reduce the linewidths of the modes. The right side is coupled to a 5-mm long CPW with a small interdigitated capacitor of $\sim$ 25 fF capacitance on the outpet end. A symmetric ($\alpha = 1$) flux-tunable transmon qubit is capacitively connected to the CPW near the output coupling capacitor. The upper sweetspot, where E_J in insensitive to magnetic flux noise to first order, was designed to be around 9 GHz. The symmetric design allows for the qubit to tune from its upper sweetspot through all of the metamaterial modes below it. An additional read-out cavity, which is a conventional CPW resonator designed to have

the fundamental frequency of 7 GHz, is placed on the bottom of the chip, so we are able to control and read-out the qubit using normal cQED read-out and control techniques [67]. The sample is made of 90-nm thick Nb on Si, except for the junctions which are made of Al-AlO_x-Al. The fabrication process is described in Chapter 10.

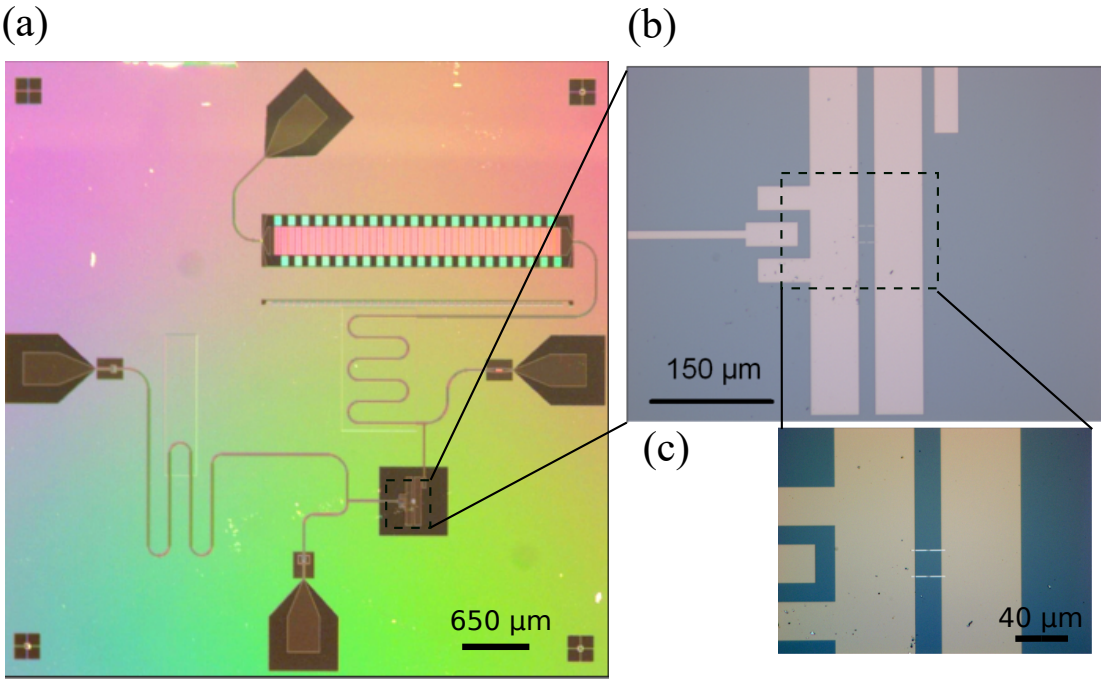

Figure 9.3: The microscopic images of the designed sample: (a) microscopic image of a copy of the measured sample. The upper right is a 42-cell metamaterial transmission line joined by a CPW on the right end. A flux-tunable transmon qubit is capacitively coupled to the CPW near the output end. (b) Zoomed-in image of the transmon. (c) Zoomed-in image of the Josephson junctions.

9.3 Measurement

The sample is mounted on the cold finger of our dilution refrigerator (DR) and then measured at $\sim$ 25 mK. Unlike in the ADR where the base temperature can only be maintained for a few hours, the DR allows for continuous cooling power at the base temperature for long measurements. Also, the DR allows for us to use an appropriate level of shielding and filtering to preserve qubit coherence, while the ADR does not have space for these components. The

sample box has a flux bobbin, which is a superconducting wire coil, on top to provide an external magnetic flux to the transmon so we can manipulate the qubit frequency by applying dc current to the bobbin.

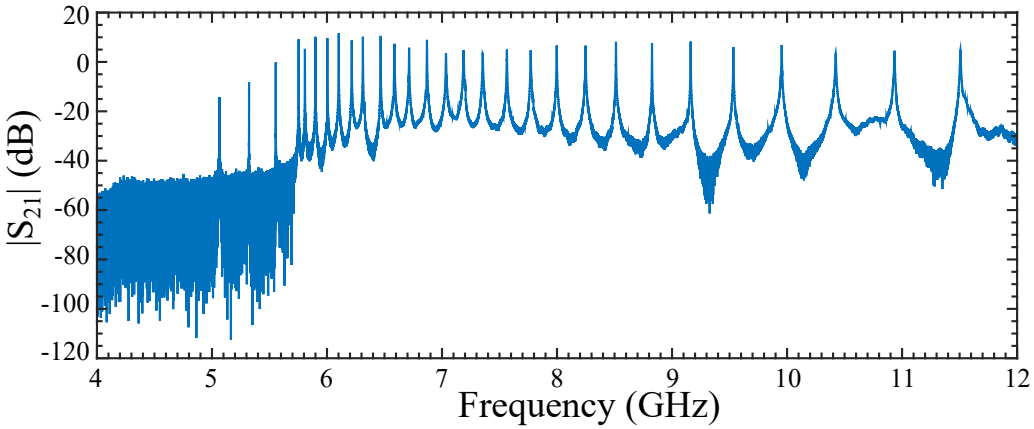

Figure 9.4: The measured $|S_{21}|(f)$ of the hybrid cavity in the DR. We don't have a baseline measured for this sample so the level is not calibrated. Similarly to the metamaterial sample (Fig. 7.3), the hybrid resonator shows a very high density of modes around 6 GHz, a cut-off frequency at around 5 GHz and spread-out mode spacings above 7 GHz.

We first measured the transmission $|S_{21}(f)|$ through the hybrid metamaterial resonator and the result is shown in Fig. 9.4. Although the baseline is uncalibrated, the spectrum shows a clear distribution of modes that is characteristic of a LHTL. The spectrum has an IR cut-off at around 5 GHz, a high density of peaks at around 6 GHz and the modes above 7 GHz have increasing mode-spacing with increasing frequency. The highest quality factor is about $130,000$ at mode 38 and most of the modes have the Q around $20,000$. Thus, our hybrid cavity is functioning well for us to explore qubit-cavity coupling. Although the coupling strength is still too small and the mode spacing is still too large for the qubit to be coupled to multiple modes simultaneously, it still shows a great potential to achieve multi-mode strong coupling.

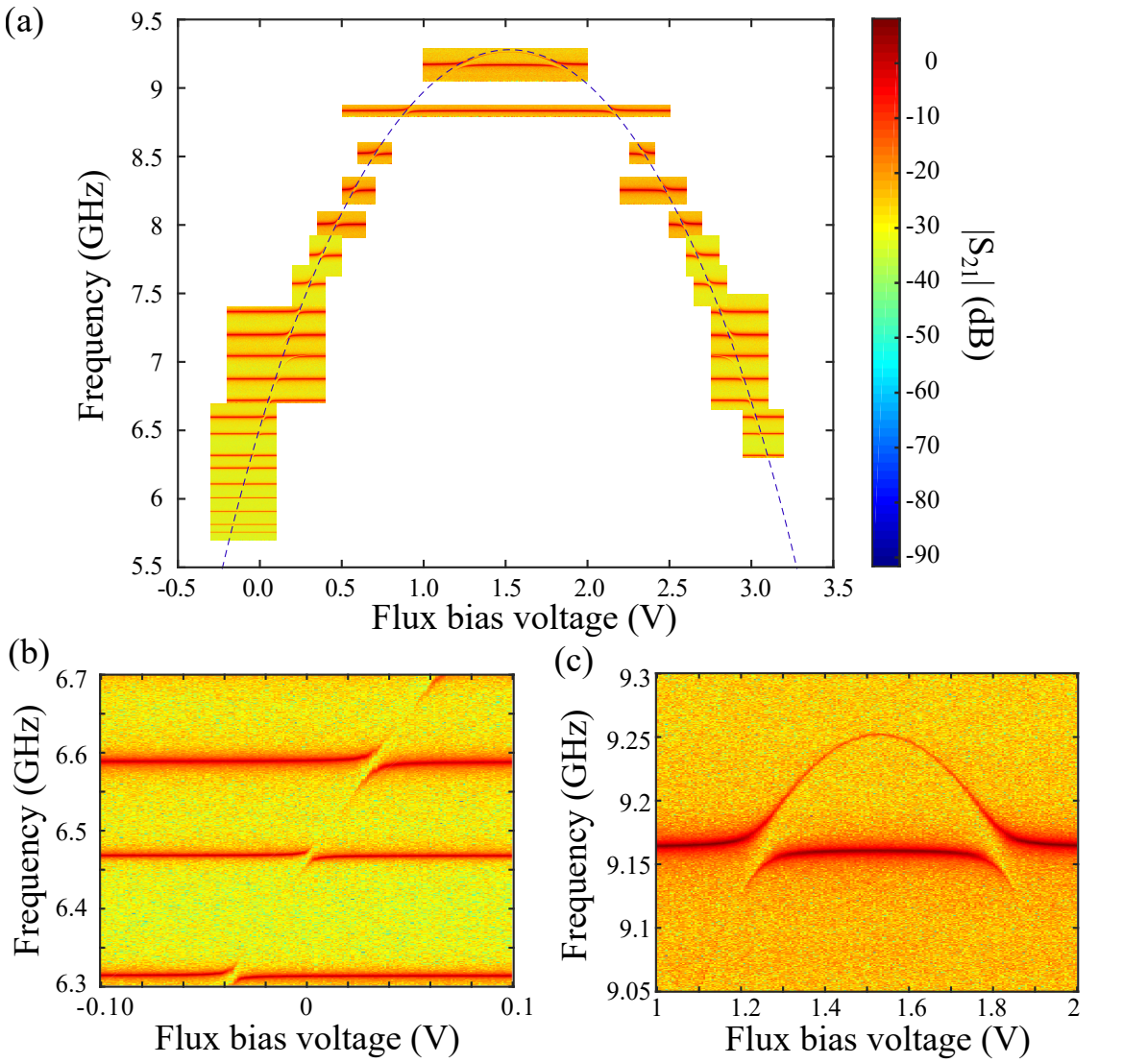

Figure 9.5: Density plot of $|S_{21}(f)|$ with the qubit tuned through different flux bias point. The color bar on the upper left applies to all the sub-images. (a) Density plot of $|S_{21}|$ over 20 modes that shows avoided crossing up to 9.2 GHz. The centers of each crossing are joined by a fit to the flux-modulation expected for the tunable transmon in dashed lines. (b) Zoomed-in plot of qubit frequency crossing with three consecutive metamaterial modes. (c) Zoomed-in plot of qubit frequency crossing with 9.16 GHz modes, which clearly shows the qubit upper sweet spot is confined to be around 9.2 GHz

9.4 Future work

Now we have successfully fabricated a hybrid cavity with a high density of resonance modes and coupled these modes to a transmon qubit. It's been the first time reported that a qubit is coupled to a metamaterial, which has the potential for exploring novel regimes of cQED and quantum simulation with multi-mode simultaneous coupling. With this sample, there are still many cQED measurement we can perform, like measuring the qubit relaxation time T_1 through the hybrid cavity at different bias point. There are also multiple improvements that could be adopted in future devices: decreasing the mode spacing by increasing the total number of cells; placing all the inductors on the same side to achieve ultra-high density of modes just above the infrared cutoff; increasing the coupling capacitance from the qubit to the hybrid cavity to increase the coupling strength.

Chapter 10

Fabrication process

This chapter is to introduce the fabrication process. The fabrication is partly done at the Cornell NanoScale Science and Technology Facility (CNF) and the rest is done at our own fab room in Syracuse. CNF is a national user facility that supports a broad range of nanoscale science and technology projects by providing state-of-the-art resources coupled with expert staff support. The metamaterial structures and the ground planes are made of 80 nm thick of Nb deposited on a silicon substrate patterned photo-lithographically. The Josephson junctions of the transmon qubit are made of a double layer of shadow evaporated Al-AlO_x-Al structure and written using e-beam lithography.

10.1 Photolithography

Photolithography is a process used in microfabrication to pattern parts of a thin film on the bulk of a substrate. In the metamaterial fabrication case, a lift-off process is used to remove the unwanted metal. I took a fresh silicon wafer to the CNF cleanroom and used compressed nitrogen air-blow to clean the wafer making sure the surface is free from dust and as dry as possible. Then I loaded the wafer into a coating tool called Gamma Automatic Coat-Develop Tool (GAMMA) to spin the photo resist on top the wafer. I normally spun a first layer of 120 nm thick of DSK-101-312. This kind of resist is called anti-reflective coating (ARC). It

will prevent the UV light that is used in the next step to reflect from the surface of the wafer to over-expose the photo-resist. DSK can't be exposed by the UV light, but it will dissolve in the developer to create an under-cut for the lift-off process. The GAMMA machine is designed to spin the resist and do a quick back side clean to ensure the back side of the wafer is not contaminated. Following that was a 60 second bake at 175 Celsius to reduce the excess solvent. Then it was cooled back down to room temperature on a chill plate. The second layer was the working photo resist of 600 nm thick. I normally use a positive resist (which means the exposed area will be removed after developing) called UV210-0.6. It then was be baked at 135 Celsius for 60 seconds right after the spinning.

Once the wafer was prepared, I would transfer it to the stepper machine called ASML 300C DUV Stepper (ASML). The machine uses a mask which was prepared using Heidelberg Mask Writer DWL2000 (Heidelberg) which uses laser to write the GDS pattern onto the mask. ASML exposed the metamaterial pattern onto the wafer using UV light at 20 mJ/cm^2 with -0.2 μm offset of the focus. After the exposure, the wafer was taken back to the GAMMA for post exposure bake and develop. For the UV210 resist, I would bake it at 135 Celsius for 90 seconds and develop it using AZ 726 MIF. The benefit of using GAMMA over the manual spin of resist is that the machine will do the spin, bake, back-side clean and develop automatically and it normally has a very good uniformity of resist and a very clean backside of the wafer. It is very important for the ASML. The ASML robot arm and platforms use vacuum to hold the wafer. If the backside of a wafer is not flat or clean enough, which could easily happen for manual spinning, it can cause the auto leveling and the focusing to fail and the wafer could get lost inside the ASML. Besides, the GAMMA can handle multiple wafers if the sequence of recipe is the same which will save the user a lot of time. Also the staff at CNF will create the recipe based on the user's individual needs on the tool which can also help save time. Once the development was done, I would take the wafer to the Glen 1000 Resist Strip (Glen) for a descum process. It's done by using reactive-ion etching (RIE) mode at 100 watts for 120 seconds to reduce any possible resist residual on the exposed area

of the wafer. The wafer is ready for metal deposition after the descum .

A sputter system in our fabrication room was used for depositing a 80 nm thick film of Nb. The patterned wafer will be loaded into the system and then covered with sputtered on the entire exposed surface with desired thickness which was 80 nm in the metamaterial case. Then I soaked the wafer in acetone to remove the UV210-0.6 photo resist. With the resist being dissolved in acetone (could be other solvent), the Nb deposited on top would be removed as well, leaving a desired pattern of metal. The bottom layer of resist which was DSK-101-312 would not dissolve in acetone so the developer (AZ726) was used after to clean it off. Another way to remove the DSK after lifting-off was to use heated microposit remover 1165 to clean the wafer. This is a very powerful method, for the 1165 could remove almost all the possible organic contamination that could build on the wafer during the process. The use of oxygen plasma to strip off the DSK is also an effective method. The wafer is ready to go to the next step, electron-beam lithography for tunnel junction patterns writing, after the cleaning process.

10.2 Electron beam lithography

For writing a pattern such as tunnel area of Josephson junction that is smaller than the wavelength of the ASML UV light which is 248 nm, e-beam lithography technique is required. This is an essential tool for nanoscale fabrication. Similarly to photolithography, e-beam lithography uses e-beam resist and exposes the resist using electrons with certain energy and then followed by a development step. In the transmon qubit case, I used a first layer of methyl metharcylate (MMA-MAA copolymer) that was spun onto the wafer at 2500 RPM and baked at 170 degrees Celsius for 10 minutes to achieve 600 nm thick and a second layer of polymethyl methacrylate (PMMA) which was spun at 3000 rmp and baked at 170 degrees Celsius for another 10 minutes to achieve 100 nm thick. The pattern was written using a tool called JEOL JBX9500FS Electron Beam Lithography System (JEOL 9500). Although

normally I pattern the entire wafer or a large chunk of the wafer, the sample that is going be to measured would be processed individually for the metal depostion and lift-off. After the e-beam writing, in order to fit the chip perfectly in the sample holder, a DISCO Dicing Saw in CNF which could provide precise cut was used to separate chips from each other.

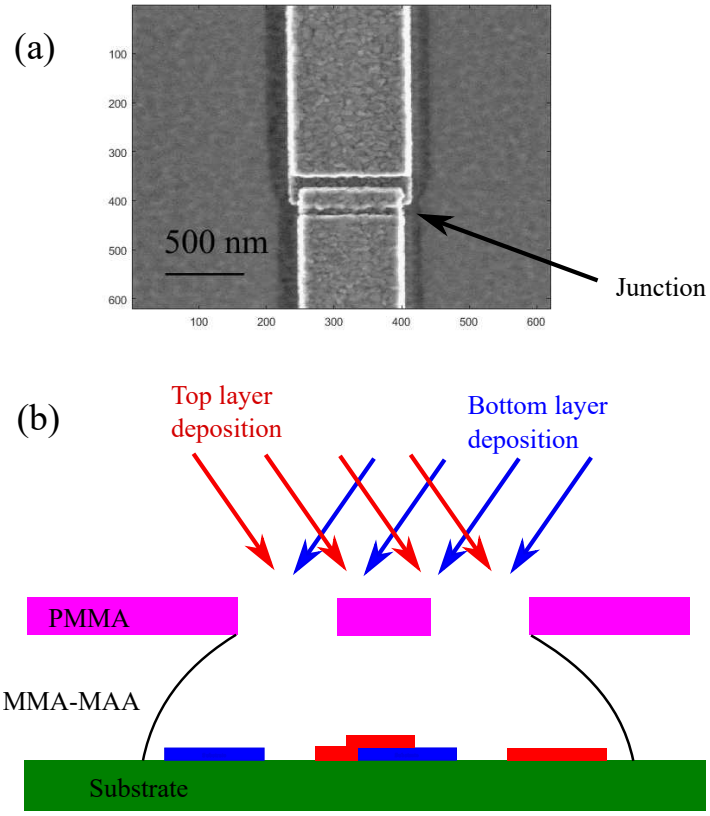

Figure 10.1: Josephson junction under SEM and double angle evaporation illustration: (a) A shadow evaporated tunnel junction made of Al-AlO_x-Al under SEM; (b) Cross-section view of the double angle shadow evapartion illustration with top layer of PMMA airbridge in pink color, the MMA-MAA with under-cut underneath the airbridge, the bottom layer metal in blue color and the top layer of metal in red color. There's a oxidation process in between the two depostions. The overlap area is the juction barrier. The plot is only for illustration purpose that it's not in scale and the angle is not meant to be the same with the actual fabrication. The deposited metal on top of resist is not shown.

To make our junction barrier tunnel, I used a so-called shadow evaporation technique combined with oxidation in between [115]. In the designed pattern, there are two long electrode traces facing each other but not touching. Since the PMMA and MMA-MAA layer reacts to the e-beam differently, I chose a certain energy so that the MMA-MAA was a little

bit over exposed while the PMMA was not. During the development, the bottom layer of MMA-MAA between the two electrodes would be removed but the PMMA would stay. This created an air bridge formed by PMMA. To develop the resist, I used a mixture of methyl isobutyl ketone (MIBK) with isopropanol (ISO) of 1:3 ratio for 60 seconds then rinsed with ISO and dried using nitrogen blow. The chip being developed was loaded into a electron-beam evaporation system in our lab to deposit the aluminum. Before depositing metal, a 13-s argon ion mill step was performed to remove the surface native oxide on the Nb contact area as well as any small surface contamination, especially the area where the junction electrodes were making contact with the bottom niobium layer to ensure the conduction between the junction electrodes and the qubit capacitor pads. The chip was tilted for 11.5 degrees respect to the horizontal before starting of the deposition. After the first layer of 65 nm thick of aluminum was deposited, low pressure 90/10 Ar/O_2 mixture was introduced to the deposition chamber at 40 mTorr for 10 minutes. This would create a layer of AlO_x which served as the insulator on top of the surface of freshly deposited aluminum. After the oxidation, the oxygen would be pumped out and the chip was tilted to -11.5 degrees to start the second layer of 35 nm thick of aluminum. This technique of double angle evaporation shown in 10.1 creates an overlap area of metal defined by the thickness and height of the airbridge and the angle of the evaporation. Also, since the bottom layer is covered with insulator, the overlap area forms an Al-AlO_x-Al Josephson tunnel junction. After the evaporation, the un-exposed e-beam resist area was stripped off by soaking in dichloromethane (DCM). This process is similar to the lift-off process described in the photolithography section to remove all the aluminum while the e-beam resist was resolved in the DCM but leave the junctions on the chip. The solvent was then cleaned using isopropanol and the chip was ready to be measured.

Bibliography

[1] Jeffrey D Wilson, Zachary D Schwartz, Christine T Chevalier, Alan N Downey, and Karl R Vaden. Flat lens focusing demonstrated with left-handed metamaterial. 2004.

[2] BLT Plourde, Haozhi Wang, Francisco Rouxinol, and MD LaHaye. Superconducting metamaterials and qubits. *arXiv:1505.01015*, 2015.

[3] D. J. Egger and F. K. Wilhelm. Multimode circuit quantum electrodynamics with hybrid metamaterial transmission lines. *Phys. Rev. Lett.*, 111:163601, 2013.

[4] Serge Haroche and Jean-Michel Raimond. *Exploring the quantum: atoms, cavities, and photons*. Oxford University press, 2006.

[5] Alexandre Blais, Ren-Shou Huang, Andreas Wallraff, S. M. Girvin, and R. J. Schoelkopf. Cavity quantum electrodynamics for superconducting electrical circuits: An architecture for quantum computation. *Phys. Rev. A*, 69:062320, Jun 2004.

[6] RJ Schoelkopf and SM Girvin. Wiring up quantum systems. *Nature*, 451(7179):664, 2008.

[7] Andreas Wallraff, David I Schuster, Alexandre Blais, L Frunzio, R-S Huang, J Majer, S Kumar, Steven M Girvin, and Robert J Schoelkopf. Strong coupling of a single photon to a superconducting qubit using circuit quantum electrodynamics. *Nature*, 431(7005):162, 2004.

[8] M Göppl, A Fragner, M Baur, R Bianchetti, S Filipp, JM Fink, PJ Leek, G Puebla, L Steffen, and Andreas Wallraff. Coplanar waveguide resonators for circuit quantum electrodynamics. *Journal of Applied Physics*, 104(11):113904, 2008.

[9] Hanhee Paik, DI Schuster, Lev S Bishop, G Kirchmair, G Catelani, AP Sears, BR Johnson, MJ Reagor, L Frunzio, LI Glazman, et al. Observation of high coherence in josephson junction qubits measured in a three-dimensional circuit qed architecture. *Physical Review Letters*, 107(24):240501, 2011.

[10] Chad Rigetti, Jay M Gambetta, Stefano Poletto, BLT Plourde, Jerry M Chow, AD Córcoles, John A Smolin, Seth T Merkel, JR Rozen, George A Keefe, et al. Superconducting qubit in a waveguide cavity with a coherence time approaching 0.1 ms. *Physical Review B*, 86(10):100506, 2012.

[11] Alexandre Blais, Jay Gambetta, A Wallraff, DI Schuster, SM Girvin, MH Devoret, and RJ Schoelkopf. Quantum-information processing with circuit quantum electrodynamics. *Physical Review A*, 75(3):032329, 2007.

[12] J Majer, JM Chow, JM Gambetta, Jens Koch, BR Johnson, JA Schreier, L Frunzio, DI Schuster, AA Houck, Andreas Wallraff, et al. Coupling superconducting qubits via a cavity bus. *Nature*, 449(7161):443, 2007.

[13] Xiu Gu, Anton Frisk Kockum, Adam Miranowicz, Yu-xi Liu, and Franco Nori. Microwave photonics with superconducting quantum circuits. *Physics Reports*, 718-719:1–102, 2017.

[14] Pol Forn-Díaz, Jürgen Lisenfeld, David Marcos, Juan José García-Ripoll, Enrique Solano, CJPM Harmans, and JE Mooij. Observation of the bloch-siegert shift in a qubit-oscillator system in the ultrastrong coupling regime. *Physical Review Letters*, 105(23):237001, 2010.

[15] Thomas Niemczyk, F Deppe, H Huebl, EP Menzel, F Hocke, MJ Schwarz, JJ Garcia-Ripoll, D Zueco, T Hümmer, E Solano, et al. Circuit quantum electrodynamics in the ultrastrong-coupling regime. *Nature Physics*, 6(10):772, 2010.

[16] Jérôme Bourassa, Jay M Gambetta, Abdufarrukh A Abdumalikov Jr, Oleg Astafiev, Y Nakamura, and A Blais. Ultrastrong coupling regime of cavity qed with phase-biased flux qubits. *Physical Review A*, 80(3):032109, 2009.

[17] S Filipp, M Göppl, JM Fink, M Baur, R Bianchetti, L Steffen, and A Wallraff. Multimode mediated qubit-qubit coupling and dark-state symmetries in circuit quantum electrodynamics. *Physical Review A*, 83(6):063827, 2011.

[18] Matteo Mariantoni, Frank Deppe, Achim Marx, Rudolf Gross, Frank K Wilhelm, and Enrique Solano. Two-resonator circuit quantum electrodynamics: A superconducting quantum switch. *Physical Review B*, 78(10):104508, 2008.

[19] Seth T Merkel and Frank K Wilhelm. Generation and detection of noon states in superconducting circuits. *New Journal of Physics*, 12(9):093036, 2010.

[20] H Wang, Matteo Mariantoni, Radoslaw C Bialczak, M Lenander, Erik Lucero, M Neeley, AD OConnell, D Sank, M Weides, J Wenner, et al. Deterministic entanglement of photons in two superconducting microwave resonators. *Physical Review Letters*, 106(6):060401, 2011.

[21] Matteo Mariantoni, H Wang, Radoslaw C Bialczak, M Lenander, Erik Lucero, M Neeley, AD OConnell, D Sank, M Weides, J Wenner, et al. Photon shell game in three-resonator circuit quantum electrodynamics. *Nature Physics*, 7(4):287, 2011.

[22] Neereja M Sundaresan, Yanbing Liu, Darius Sadri, László J Szőcs, Devin L Underwood, Moein Malekakhlagh, Hakan E Türeci, and Andrew A Houck. Beyond strong coupling in a multimode cavity. *Physical Review X*, 5(2):021035, 2015.

[23] Devin L Underwood, Will E Shanks, Jens Koch, and Andrew A Houck. Low-disorder microwave cavity lattices for quantum simulation with photons. *Physical Review A*, 86(2):023837, 2012.

[24] Mattias Fitzpatrick, Neereja M Sundaresan, Andy CY Li, Jens Koch, and Andrew A Houck. Observation of a dissipative phase transition in a one-dimensional circuit qed lattice. *Physical Review X*, 7(1):011016, 2017.

[25] David C McKay, Ravi Naik, Philip Reinhold, Lev S Bishop, and David I Schuster. High-contrast qubit interactions using multimode cavity qed. *Phys. Rev. Lett.*, 114(8):080501, 2015.

[26] RK Naik, N Leung, S Chakram, Peter Groszkowski, Y Lu, N Earnest, DC McKay, Jens Koch, and DI Schuster. Random access quantum information processors using multimode circuit quantum electrodynamics. *Nature communications*, 8(1):1904, 2017.

[27] RP Erickson, MR Vissers, M Sandberg, SR Jefferts, and DP Pappas. Frequency comb generation in superconducting resonators. *Phys. Rev. Lett.*, 113(18):187002, 2014.

[28] Viktor G Veselago. The electrodynamics of substances with simultaneously negative values of and μ. *Soviet physics uspekhi*, 10(4):509, 1968.

[29] Andrea Alu and Nader Engheta. Multifrequency optical invisibility cloak with layered plasmonic shells. *Physical Review Letters*, 100(11):113901, 2008.

[30] John Brian Pendry. Negative refraction makes a perfect lens. *Physical Review Letters*, 85(18):3966, 2000.

[31] K. Busch, G. von Freymann, S. Linden, S.F. Mingaleev, L. Tkeshelashvili, and M. Wegener. Periodic nanostructures for photonics. *Phys. Rep.*, 444:101–202, 2007.

[32] RA Shelby, DR Smith, SC Nemat-Nasser, and Sheldon Schultz. Microwave transmission through a two-dimensional, isotropic, left-handed metamaterial. *Applied Physics Letters*, 78(4):489–491, 2001.

[33] John B Pendry, AJ Holden, WJ Stewart, and I Youngs. Extremely low frequency plasmons in metallic mesostructures. *Physical Review Letters*, 76(25):4773, 1996.

[34] John B Pendry, Anthony J Holden, David J Robbins, and WJ Stewart. Magnetism from conductors and enhanced nonlinear phenomena. *IEEE Transactions on Microwave Theory and Techniques*, 47(11):2075–2084, 1999.

[35] Michael Ricci, Nathan Orloff, and Steven M Anlage. Superconducting metamaterials. *Applied Physics Letters*, 87(3):034102, 2005.

[36] Michael C Ricci and Steven M Anlage. Single superconducting split-ring resonator electrodynamics. *Applied Physics Letters*, 88(26):264102, 2006.

[37] Chunguang Du, Hongyi Chen, and Shiqun Li. Stable and bistable squid metamaterials. *Journal of Physics: Condensed Matter*, 20(34):345220, 2008.

[38] N Lazarides and GP Tsironis. Rf superconducting quantum interference device metamaterials. *Applied Physics Letters*, 90(16):163501, 2007.

[39] Yu Krupko, VD Nguyen, T Weißl, É Dumur, J Puertas, C Naud, FWJ Hekking, DM Basko, O Buisson, and W Hasch-Guichard. Kerr non-linearity in a superconducting josephson metamaterial. *arXiv:1807.01499*, 2018.

[40] Chunguang Du, Hongyi Chen, and Shiqun Li. Quantum left-handed metamaterial from superconducting quantum-interference devices. *Physical Review B*, 74(11):113105, 2006.

[41] George V Eleftheriades, Ashwin K Iyer, and Peter C Kremer. Planar negative refractive

index media using periodically lc loaded transmission lines. *IEEE Transactions on microwave theory and techniques*, 50(12):2702–2712, 2002.

[42] H Salehi, AH Majedi, and RR Mansour. Analysis and design of superconducting left-handed transmission lines. *IEEE Transactions on Applied Superconductivity*, 15(2):996–999, 2005.

[43] Chrirtophe Caloz and T Itoh. Transmission line approach of left-handed (lh) materials and microstrip implementation of an artificial lh transmission line. *IEEE Transactions on Antennas and propagation*, 52(5):1159–1166, 2004.

[44] Atsushi Sanada, Christophe Caloz, and Tatsuo Itoh. Novel zeroth-order resonance in composite right/left-handed transmission line resonators. In *Proc. Asia-Pacific Microwave Conf*, volume 3, pages 1588–1591, 2003.

[45] Changjun Liu and Kama Huang. Metamaterial transmission line and its applications. In *Advanced Microwave and Millimeter Wave Technologies Semiconductor Devices Circuits and Systems*. InTech, 2010.

[46] Christophe Caloz, Atsushi Sanada, and Tatsuo Itoh. A novel composite right-/left-handed coupled-line directional coupler with arbitrary coupling level and broad bandwidth. *IEEE Transactions on Microwave Theory and Techniques*, 52(3):980–992, 2004.

[47] Yi Wang and Michael J Lancaster. High-temperature superconducting coplanar left-handed transmission lines and resonators. *IEEE Transactions on Applied Superconductivity*, 16(3):1893–1897, 2006.

[48] P Jung, S Butz, M Marthaler, MV Fistul, Juha Leppäkangas, VP Koshelets, and AV Ustinov. Multistability and switching in a superconducting metamaterial. *Nature communications*, 5:3730, 2014.

[49] Alexandre M Zagoskin, Didier Felbacq, and Emmanuel Rousseau. Quantum metamaterials in the microwave and optical ranges. *EPJ Quantum Technology*, 3(1):2, 2016.

[50] C. Hutter, K. Stannigel, E. Tholen, and J. Lidmar. Josephson junction transmission lines as tunable artificial crystals. *Phys. Rev. B*, 83:014511, 2011.

[51] Steven M Anlage. The physics and applications of superconducting metamaterials. *Journal of Optics*, 13(2):024001, 2010.

[52] PD Nation, MP Blencowe, AJ Rimberg, and E Buks. Analogue hawking radiation in a dc-squid array transmission line. *Physical Review Letters*, 103(8):087004, 2009.

[53] Javier Puertas Martinez, Sebastien Leger, Nicolas Gheereart, Remy Dassonneville, Luca Planat, Farshad Foroughi, Yuriy Krupko, Olivier Buisson, Cecile Naud, Wiebke Guichard, et al. Probing a transmon qubit via the ultra-strong coupling to a josephson waveguide. *arXiv:1802.00633*, 2018.

[54] Mohammad Mirhosseini, Eunjong Kim, Vinicius S Ferreira, Mahmoud Kalaee, Alp Sipahigil, Andrew J Keller, and Oskar Painter. Superconducting metamaterials for waveguide quantum electrodynamics. *arXiv:1802.01708*, 2018.

[55] MA Castellanos-Beltran, KD Irwin, GC Hilton, LR Vale, and KW Lehnert. Amplification and squeezing of quantum noise with a tunable josephson metamaterial. *Nature Physics*, 4(12):929, 2008.

[56] Kejie Fang, Matthew H Matheny, Xingsheng Luan, and Oskar Painter. Optical transduction and routing of microwave phonons in cavity-optomechanical circuits. *Nature Photonics*, 10(7):489, 2016.

[57] John David Jackson. *Classical Electrodynamics*. Wiley, New York, NY, 1999.

[58] Alistair Kwan, John Dudley, and Eric Lantz. Who really discovered Snell's law? *Physics World*, 15(4):64, 2002.

[59] Betty Isabelle Bleaney, Betty Isabelle Bleaney, and Brebis Bleaney. *Electricity and Magnetism*, volume 2. Oxford University Press, 2013.

[60] Richard A Shelby, David R Smith, and Seldon Schultz. Experimental verification of a negative index of refraction. *Science*, 292(5514):77–79, 2001.

[61] David R Smith, Willie J Padilla, DC Vier, Syrus C Nemat-Nasser, and Seldon Schultz. Composite medium with simultaneously negative permeability and permittivity. *Physical Review Letters*, 84(18):4184, 2000.

[62] David R Smith, John B Pendry, and Mike CK Wiltshire. Metamaterials and negative refractive index. *Science*, 305(5685):788–792, 2004.

[63] A Wallraff, DI Schuster, A Blais, L Frunzio, J Majer, MH Devoret, SM Girvin, and RJ Schoelkopf. Approaching unit visibility for control of a superconducting qubit with dispersive readout. *Physical Review Letters*, 95(6):060501, 2005.

[64] Michael Metcalfe, E Boaknin, V Manucharyan, R Vijay, I Siddiqi, C Rigetti, L Frunzio, RJ Schoelkopf, and MH Devoret. Measuring the decoherence of a quantronium qubit with the cavity bifurcation amplifier. *Physical Review B*, 76(17):174516, 2007.

[65] JE Johnson, Christopher Macklin, DH Slichter, R Vijay, EB Weingarten, John Clarke, and Irfan Siddiqi. Heralded state preparation in a superconducting qubit. *Physical Review Letters*, 109(5):050506, 2012.

[66] A Lupaşcu, EFC Driessen, L Roschier, CJPM Harmans, and JE Mooij. High-contrast dispersive readout of a superconducting flux qubit using a nonlinear resonator. *Physical Review Letters*, 96(12):127003, 2006.

[67] JD Strand, Matthew Ware, Félix Beaudoin, TA Ohki, BR Johnson, Alexandre Blais, and BLT Plourde. First-order sideband transitions with flux-driven asymmetric transmon qubits. *Physical Review B*, 87(22):220505, 2013.

[68] Max Hofheinz, H Wang, Markus Ansmann, Radoslaw C Bialczak, Erik Lucero, Matthew Neeley, AD O'connell, Daniel Sank, J Wenner, John M Martinis, et al. Synthesizing arbitrary quantum states in a superconducting resonator. *Nature*, 459(7246):546, 2009.

[69] RH Koch, GA Keefe, FP Milliken, JR Rozen, CC Tsuei, JR Kirtley, and DP DiVincenzo. Experimental demonstration of an oscillator stabilized josephson flux qubit. *Physical Review Letters*, 96(12):127001, 2006.

[70] H Wang, M Hofheinz, M Ansmann, RC Bialczak, E Lucero, M Neeley, AD Oconnell, D Sank, J Wenner, AN Cleland, et al. Measurement of the decay of fock states in a superconducting quantum circuit. *Physical Review Letters*, 101(24):240401, 2008.

[71] Jerry Moy Chow. *Quantum information processing with superconducting qubits*. PhD thesis, Yale University, 2010.

[72] David M Pozar. *Microwave engineering*. John Wiley & Sons, 2009.

[73] Yu Hao. *Qubit Coupled Mechanical Resonator in an Electromechanical System*. PhD thesis, Syracuse University, 2017.

[74] David Isaac Schuster. *Circuit quantum electrodynamics*. PhD thesis, Yale University, 2007.

[75] Jiansong Gao. *The physics of superconducting microwave resonators*. California Institute of Technology, 2008.

[76] PJ De Visser. *Quasiparticle dynamics in aluminium superconducting microwave resonators*. PhD thesis, TU Delft, Delft University of Technology, 2014.

[77] Rainee N Simons. *Coplanar waveguide circuits, components, and systems*, volume 165. John Wiley & Sons, 2004.

[78] KC Gupta, R Garg, I Bahl, and P Bhartia. Microstrip lines and slotlines. 1996. *Arthech House*.

[79] I Nsanzineza and BLT Plourde. Trapping a single vortex and reducing quasiparticles in a superconducting resonator. *Physical Review Letters*, 113(11):117002, 2014.

[80] L Brillouin. Wave propagation in periodic structures. electric filters and crystal lattices, ser. international series in pure and applied physics, 1946.

[81] Christophe Caloz and Tatsuo Itoh. *Electromagnetic metamaterials: transmission line theory and microwave applications*. John Wiley & Sons, 2005.

[82] George V Eleftheriades, Omar Siddiqui, and Ashwin K Iyer. Transmission line models for negative refractive index media and associated implementations without excess resonators. *IEEE Microwave and Wireless Components Letters*, 13(2):51–53, 2003.

[83] Anthony Lai, Tatsuo Itoh, and Christope Caloz. Composite right/left-handed transmission line metamaterials. *IEEE microwave magazine*, 5(3):34–50, 2004.

[84] S Wang, AP Feresidis, George Goussetis, and JC Vardaxoglou. High-gain subwavelength resonant cavity antennas based on metamaterial ground planes. *IEE Proceedings-Microwaves, Antennas and Propagation*, 153(1):1–6, 2006.

[85] Christos Christopoulos. *The transmission-line modeling method: TLM*. Oxford University Press, 1995.

[86] Christophe Caloz, Atsushi Sanada, and Tatsuo Itoh. A novel composite right-/left-handed coupled-line directional coupler with arbitrary coupling level and broad bandwidth. *IEEE Transactions on Microwave Theory and Techniques*, 52(3):980–992, 2004.

[87] AA Houck, JA Schreier, BR Johnson, JM Chow, Jens Koch, JM Gambetta, DI Schuster, L Frunzio, MH Devoret, SM Girvin, et al. Controlling the spontaneous emission of a superconducting transmon qubit. *Physical Review Letters*, 101(8):080502, 2008.

[88] Janet Golio and Mike Golio. *RF and microwave circuits, measurements, and modeling*. CRC press, 2007.

[89] Richard J Collier and A Douglas Skinner. *Microwave measurements*, volume 12. IET, 2007.

[90] Anthony Megrant, Charles Neill, Rami Barends, Ben Chiaro, Yu Chen, Ludwig Feigl, Julian Kelly, Erik Lucero, Matteo Mariantoni, Peter JJ OMalley, et al. Planar superconducting resonators with internal quality factors above one million. *Applied Physics Letters*, 100(11):113510, 2012.

[91] David P Pappas, Michael R Vissers, David S Wisbey, Jeffrey S Kline, and Jiansong Gao. Two level system loss in superconducting microwave resonators. *IEEE Transactions on Applied Superconductivity*, 21(3):871–874, 2011.

[92] R Barends, HL Hortensius, T Zijlstra, JJA Baselmans, SJC Yates, JR Gao, and TM Klapwijk. Contribution of dielectrics to frequency and noise of nbtin superconducting resonators. *Applied Physics Letters*, 92(22):223502, 2008.

[93] H Wang, M Hofheinz, J Wenner, M Ansmann, RC Bialczak, M Lenander, Erik Lucero, M Neeley, AD OConnell, D Sank, et al. Improving the coherence time of superconducting coplanar resonators. *Applied Physics Letters*, 95(23):233508, 2009.

[94] JE Acuna, JL Rodriguez, and F Obelleiro. Design of meander line inductors on printed circuit boards. *International Journal of RF and Microwave Computer-Aided Engineering: Co-sponsored by the Center for Advanced Manufacturing and Packaging of Microwave, Optical, and Digital Electronics (CAMPmode) at the University of Colorado at Boulder*, 11(4):219–230, 2001.

[95] H Salehi, RR Mansour, and AH Majedi. Nonlinear josephson left-handed transmission lines. *IET microwaves, antennas & propagation*, 1(1):69–72, 2007.

[96] S Chaki, S Aono, N Andoh, Y Sasaki, N Tanino, and O Ishihara. Experimental study on spiral inductors. In *Microwave Symposium Digest, 1995., IEEE MTT-S International*, pages 753–756. IEEE, 1995.

[97] Michael Tinkham. *Introduction to superconductivity*. McGraw-Hill, Inc., 2nd edition, 1996.

[98] Matthijs W den Otter. Approximate expressions for the capacitance and electrostatic potential of interdigitated electrodes. *Sensors and Actuators A: Physical*, 96(2-3):140–144, 2002.

[99] Inc. ANSYS. Introduction to ansys q3d extractor release 10.0.

[100] Aaron D OConnell, M Ansmann, Radoslaw C Bialczak, Max Hofheinz, Nadav Katz, Erik Lucero, C McKenney, Matthew Neeley, Haohua Wang, Eva M Weig, et al. Microwave dielectric loss at single photon energies and millikelvin temperatures. *Applied Physics Letters*, 92(11):112903, 2008.

[101] John M Martinis, Ken B Cooper, Robert McDermott, Matthias Steffen, Markus Ansmann, KD Osborn, Katarina Cicak, Seongshik Oh, David P Pappas, Raymond W Simmonds, et al. Decoherence in josephson qubits from dielectric loss. *Physical Review Letters*, 95(21):210503, 2005.

[102] Frank Pobell. *Matter and methods at low temperatures*, volume 2. Springer, 1996.

[103] Bernd T Matthias, Theodore H Geballe, and V B Compton. Superconductivity. *Reviews of Modern Physics*, 35(1):1, 1963.

[104] R Meservey and PM Tedrow. Measurements of the kinetic inductance of superconducting linear structures. *Journal of Applied Physics*, 40(5):2028–2034, 1969.

[105] Ibrahim Nsanzineza. *Vortices and Quasiparticles in Superconducting Microwave Resonators*. PhD thesis, Syracuse University, 2016.

[106] Cihan Kurter, Alexander P Zhuravel, Alexey V Ustinov, and Steven M Anlage. Microscopic examination of hot spots giving rise to nonlinearity in superconducting resonators. *Physical Review B*, 84(10):104515, 2011.

[107] Alexander P Zhuravel, Steven M Anlage, and Alexey V Ustinov. Measurement of local reactive and resistive photoresponse of a superconducting microwave device. *Applied Physics Letters*, 88(21):212503, 2006.

[108] AP Zhuravel, AG Sivakov, OG Turutanov, AN Omelyanchouk, Steven M Anlage, A Lukashenko, AV Ustinov, and D Abraimov. Laser scanning microscopy of hts films and devices. *Fizika Nizkikh Temperatur*, 32(6):775–794, 2006.

[109] James C Culbertson, Harvey S Newman, and Charles Wilker. Optical probe of microwave current distributions in high temperature superconducting transmission lines. *Journal of Applied Physics*, 84(5):2768–2787, 1998.

[110] AP Zhuravel, Steven M Anlage, Stephen K Remillard, AV Lukashenko, and AV Ustinov. Effect of laalo 3 twin-domain topology on local dc and microwave properties of cuprate films. *Journal of Applied Physics*, 108(3):033920, 2010.

[111] Sonnet. Sonnet suites version 16.52.

[112] Neereja M Sundaresan, Yanbing Liu, Darius Sadri, László J Szőcs, Devin L Underwood, Moein Malekakhlagh, Hakan E Türeci, and Andrew A Houck. Beyond strong coupling in a multimode cavity. *Phys. Rev. X*, 5(2):021035, 2015.

[113] Jens Koch, M Yu Terri, Jay Gambetta, Andrew A Houck, DI Schuster, J Majer, Alexandre Blais, Michel H Devoret, Steven M Girvin, and Robert J Schoelkopf. Charge-insensitive qubit design derived from the cooper pair box. *Physical Review A*, 76(4):042319, 2007.

[114] MD Hutchings, Jared B Hertzberg, Yebin Liu, Nicholas T Bronn, George A Keefe, Markus Brink, Jerry M Chow, and BLT Plourde. Tunable superconducting qubits with flux-independent coherence. *Physical Review Applied*, 8(4):044003, 2017.

[115] Michael Paul DeFeo. *Microstrip Superconducting Quantum Interference Devices for Quantum Information Science*. PhD thesis, Syracuse University, 2012.

Contact

Name: **Haozhi Wang**

Email: hzw2011@gmail.com

Address: Department of Physics, Syracuse University, Syracuse, NY, 13244

Education

B.S., Physics, Renmin University of China, 2011

Professional Experience

Aug. 2011 - Jan. 2012, Teaching Assistant, Syracuse University

Jan. 2012 - Aug. 2018, Research Assistant, Syracuse University

Publications

1. B. L. T. Plourde, **Haozhi Wang**, Francisco Rouxinol, M.D. LaHaye. *Superconducting metamaterials and qubits*. Proceedings of the SPIE 9500, Quantum Information and Computation XIII, 95000M (2015).

2. In preparation: **Haozhi Wang**, et al. *Mode Structure in Superconducting Metamaterial Transmission Line Resonators*.

Presentations and Posters

1. Presentations at American Physical Society (APS) March Meetings in 2013, 2015, 2016, 2017.

2. Poster presented at 2014 Applied Superconductivity Conference, *Development of superconducting metamaterial structures for coupling to qubits*.